AD-A062 605 TORONTO UNIV DOWNSVIEW (ONTARIO) INST FOR AEROSPACE --ETC F/G 20/1
DIRECT CORRELATION OF NOISE AND FLOW OF A JET USING LASER DOPPL--ETC(U)
JUN 78 W G RICHARZ AFOSR-75-2808

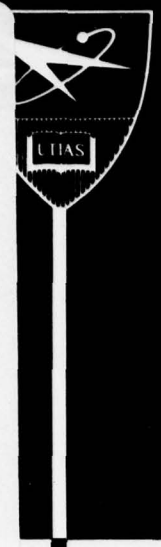
UNCLASSIFIED UTIAS-230 AFOSR-TR-78-1641 NL

1 OF 2
ADA
062605





AD A062605



INSTITUTE FOR AEROSPACE STUDIES

UNIVERSITY OF TORONTO

DDC FILE COPY

AFOSR-TR- 78-1641

DIRECT CORRELATION OF NOISE AND FLOW OF A JET USING LASER DOPPLER

LEVEL II
12

by

W. G. Richarz

DDC
DEC 28 1978
F

This document has been approved for public release and sale; its distribution is unlimited.

June, 1978

UTIAS Report No. 230
CN ISSN 0082-5255

78 12 26 081

Qualified requestors may obtain additional copies from the Defense Documentation Center, all others should apply to the National Technical Information Service.

Conditions of Reproduction:

Reproduction, translation, publication, use and disposal in whole or in part by or for the United States Government is permitted.

Approved for public release; distribution unlimited.

(6) DIRECT CORRELATION OF NOISE AND FLOW OF A JET USING LASER DOPPLER

by

(9) Interim rept. 1 Jan – 31 Dec 78,

(10) W. G. Richarz

(11) Submitted June 1978

(16) 2307 (17) A2

(12) 111 p. (14) UTIAS-230

(15) AFOSR-75-2808

(19) TR-78-1641

(18) AFOSR

AIR FORCE OFFICE OF SCIENTIFIC RESEARCH (AFSC)
NOTICE OF TRANSMITTAL TO DDC
This technical report has been reviewed and is approved for public release IAW AFR 190-12 (7b).
Distribution is unlimited.
A. D. BLOSE
Technical Information Officer

June, 1978

UTIAS Report No. 230
CN ISSN 0082-5255

78

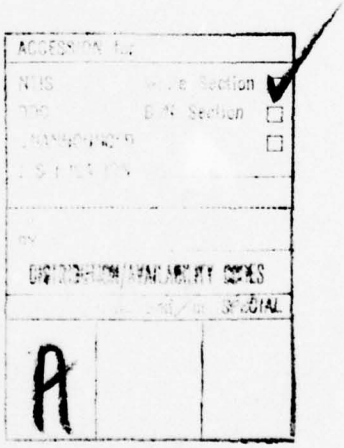
178920

Acknowledgement

The author is indebted to Dr. H. S. Ribner who initiated and supervised this research. Dr. Ribner's continued interest, stimulating discussions, and numerous suggestions are gratefully acknowledged.

Thanks are also due to the staff at UTIAS for their cooperation, in particular to Dr. G. W. Johnston and Mr. W. Davies for their helpful discussions.

The research was supported by funds from the National Research Council of Canada and the United States Air Force Office of Scientific Research under Grant AF-AFOSR 75-2808B.



12 26 081

Summary

Lighthill's theory of jet noise, as extended and developed by Ribner (self and shear noise), has successfully described many features of the jet noise outside the 'refraction valley'. However, attempts to measure the self and shear noise source terms directly by means of a cross-correlation technique have been only partially successful. The major difficulty has been suspected as spurious 'probe noise' generated by turbulence - hot wire interaction. Thus, to avoid this problem, the traditional hot wire anemometer has been replaced in the present investigation by a non-intrusive device: a Laser Doppler Velocimeter. Substantial modifications were made to meet the constraints imposed by the correlation experiment; a major feature was provision to measure $u_{(x)}$, the component of turbulent velocity in the observer direction $\underset{\sim}{x}$.

Cross-correlations and cross-spectral densities of the jet noise at 40° to the jet axis and the instantaneous turbulent jet flow u_x ($\partial^2 u_x/\partial t^2 \sim$ shear noise source term) or u_x^2 ($\partial^2 u_x^2/\partial t^2 \sim$ self noise source term) were measured at various source positions in the jet. Source distributions were inferred therefrom over slices of jet normal to the jet axis. They were found to be strongly pear-shaped, rather than axisymmetric, the small end of the 'pear' pointing toward the observer. (This is not, however, incompatible with the axisymmetry of far field sound intensity.)

Self and shear noise spectra have been constructed from the measured cross-spectral densities by a method consistent with the postulated self/shear noise formalism. The two spectra exhibit comparable amplitudes and virtually identical shapes, but are displaced substantially in frequency: all this is predicted by the theory. Self and shear noise spectra extracted from far field jet noise intensities via an algorithm of Nossier and Ribner exhibit the same behaviour. On the whole both sets of spectra, although derived from vastly different experimental procedures, are compatible.

CONTENTS

		Page
	Acknowledgement	ii
	Summary	iii
	Notation	vi
1.	INTRODUCTION	1
	1.1 Historical Background	1
	1.2 Ribner's Self and Shear Noise Model	3
	1.3 Present Investigation	5
2.	THEORY	6
	2.1 Fundamental Equations	6
	2.2 Auto-Correlation and Power Spectral Density of the Far Field Pressure	8
3.	EXPERIMENTAL FACILITIES: DEVELOPMENT AND ARRANGEMENT	12
	3.1 Laser Doppler Velocimeter	12
	3.1.1 Operating Principle	12
	3.1.2 Optical Package	14
	3.1.3 Laser Doppler Processor	15
	3.1.4 Seeding Generator	16
	3.2 Analog Squaring Module	17
	3.2.1 Non-Ideal Behaviour of Analog Multipliers	17
	3.2.2 Squaring Circuit	18
	3.3 Acoustical System	18
	3.3.1 Anechoic Room	18
	3.3.2 Model Air Jet	18
	3.3.3 Microphone System	19
	3.4 Hot Wire Anemometer	19
	3.5 Signal Processing Instrumentation	20
	3.5.1 PAR 101 Correlation Function Computer	20
	3.5.2 Spectral Dynamics Digital Signal Processor 360 (DSP 360)	20
	3.5.3 Ancillary Instrumentation	20
4.	EXPERIMENTAL CONSIDERATIONS AND CROSS-CHECKS	21
	4.1 The Effect of Transducers and Amplifiers	21
	4.2 The Effect of Sound-Flow Interaction	23
	4.3 Jet Flow Field	24
	4.4 Jet Noise	25
	4.5 Laser Doppler Velocimeter Performance Checks	27

		Page
4.5.1	Beam Intersection	27
4.5.2	Measurement of Jet Velocity	27
4.5.3	Effect of the LDV Processor on the Turbulent Velocity Spectrum	28
4.5.4	Mass Addition Due to Seeding of the Flow	28
5.	EXPERIMENTAL PROCEDURE	29
5.1	Field Points	29
5.2	Signal Handling	29
5.3	Correlation Measurements	30
5.4	Cross-Spectral Density Measurements	30
6.	RESULTS AND DISCUSSION	33
6.1	Cross-Correlations	33
6.2	Contribution to the Jet Noise from a Unit Volume of Jet	33
6.3	Contribution to the Jet Noise from a Slice of Jet	34
6.4	Jet Noise Contribution from Field Points in the Region $3 < y_1/D < 7$	35
6.5	Concluding Remarks	38
	REFERENCES	39
	FIGURES	
	APPENDIX A - A SIMPLE JET NOISE MODEL	
	APPENDIX B - NOISE GENERATED BY TRANSDUCER-FLOW INTERACTION	
	APPENDIX C - CROSS-SPECTRAL DENSITY ESTIMATES COMPUTED BY A FAST FOURIER TRANSFORM ANALYZER	
	APPENDIX D - SOME PROPERTIES OF THE LASER DOPPLER SIGNALS	
	APPENDIX E - ESTIMATE OF THE POWER SPECTRAL DENSITY OF THE LDV OUTPUT	

Notation

ρ	density of air (kg/m^3)
ρ_o	density of air at ambient temperature (1.2 kg/m^3)
P	overall pressure (N/m^2)
p	acoustic pressure (N/m^2)
p_{SH}	acoustic pressure generated by sources $\alpha \frac{\partial^2}{\partial t^2} u_x$
p_{SF}	acoustic pressure generated by sources $\alpha \frac{\partial^2}{\partial t^2} u_x^2$
$\overline{p^2_{ref}}$	arbitrary mean square reference pressure
v_i	total instantaneous velocity in the i direction
u_i	turbulent velocity in the i direction
U_i	mean velocity in the i direction
c_o	speed of sound at ambient temperature (343 m/sec)
$\underline{y}$	coordinate, usually designating source position in the jet
$\underline{x}$	coordinate, usually designating observer position
D	jet nozzle diameter
R	jet nozzle radius
y_1/D	normalized axial jet coordinate
r/R	normalized radial jet coordinate
ϕ	azimuthal angle
A_n	cross-sectional area of a slice of jet at $y_1/D = n$
$R_{v_1 v_2}(\underrightarrow{x},\underrightarrow{y},\tau)$	cross-correlation of $v_1(\underrightarrow{x},t)$ and $v_2(\underrightarrow{y},t-\tau)$
t	time (sec)
τ	time delay (sec)
$\Phi_{v_1 v_2}(\underrightarrow{x},\underrightarrow{y},\omega)$	cross-spectral density of $v_1(\underrightarrow{x},t)$ and $v_2(\underrightarrow{y},t)$
ω	radian frequency (sec^{-1})
f	frequency (Hz)

T_o	arbitrary time interval (sec)
$d_{1,2}$	relative contribution of a source in a slice of jet to the far field shear (1) or self (2) noise, reference position is at $r/R = 1$, $\phi = 0°$
$D_{1,2}$	area integral of $d_{1,2}$ over a slice of jet
$\delta(t)$	delta function: $\int_{-\infty}^{\infty} \delta(t - t_o) f(t) dt = f(t_o)$
$H(t)$	Heaviside function (unit step): $\int_{-\infty}^{\infty} \delta(t) dt = H(t)$
$h(t)$	impulse response of a linear system
$\mathcal{H}(\omega)$	transfer function of a linear system [Fourier transform of $h(t)$]
k_μ	velocity conversion factor (V/m/sec)
k_p	pressure conversion factor ($V/N/m^2$)
V_s	voltage analog of the physical quantity S
γ	AC feed-through coefficient of an analog multiplier
RMS	root mean square value (e.g. $\overline{p^2}$)
ν_o	frequency of laser light
λ_o	wavelength of laser light
$\sqrt{D}$	Doppler frequency
i	$\sqrt{-1}$
i,j	indices of the coordinates (1, 2, 3)
$\overline{\quad}$	denotes time average

1. INTRODUCTION

1.1 Historical Background

Over a quarter century ago, Sir James Lighthill (Refs. 1, 2) proposed a theory of sound generation by turbulent flows. The governing wave equation is a direct consequence of the equations of conservation of mass and momentum. The sound sources are described as an equivalent distribution of quadrupoles in a quiescent medium whose strength is proportional to time varying virtual stresses in the fluid. For a subsonic jet at ambient temperature the inertial Reynolds stresses $\rho v_i v_j$ are the dominant sources. Scaling considerations led Lighthill to deduce the $U^8 D^2$ acoustic power law which is strongly supported by measurements from subsonic jet flows (Ref. 3).

In order to be able to predict the relevant properties of jet noise (the mean square pressure for example) two point correlations of $\rho v_i v_j$, or equivalent source terms, must be known or modelled. Proudman (Ref. 4) pointed out that the distribution of sources with strength $\partial^2/\partial t^2\ \rho v_x^2$ (a single term) is equivalent to the quadrupole distribution of strength $\rho v_i v_j$ (six terms), if the radiation to an observer at $\underrightarrow{x}$ far away from the source region is considered (v_x is the velocity in the direction of the observer). He applied this formalism to evaluate the noise from decaying isotropic turbulence described by a statistical model.

Lilley (Ref. 5) applied Lighthill's theory in a quantitative fashion to the noise generation of air jets. A particular feature of his approach was a split into 'shear noise' and 'self noise'. The shear noise sources were modelled (Ref. 2) as proportional to the first time derivative of the total pressure multiplied by a mean rate of strain. Such sources were believed to be dominant in regions of high shear, as is found in the mixing region of a jet. (Ribner, Ref. 6, later argued that the relative spatial scales of turbulence and mean shear are comparable in such a region and thus the shear noise sources are not necessarily dominant.) Additional noise - self noise - is generated by the turbulent flow regardless of the presence of mean shear. Lilley computed hypothetical spectra and directivity patterns based on assumed two point correlations of the self and shear noise sources. He independently derived the x^o and x^{-7} laws, first obtained by Ribner (Ref. 7), which describe the axial source strength distribution in the mixing region and the fully developed jet respectively. Powell (Ref. 8) also developed these scaling laws from turbulence similarity considerations, as well as a corresponding jet noise spectral shape (f^2 at low frequencies, f^{-2} at high frequencies).

A different self and shear noise model was proposed by Ribner (Refs. 9, 10) in which the momentum flux ρv_x^2 of the Proudman formalism is decomposed into two contributing terms $2\rho U_x u_x$ [$U_x(\partial^2 u_x/\partial t^2)$ ~ shear noise] and $\rho u_x^2[(\partial^2 u_x^2/\partial t^2)$ ~ self noise]. He was able to predict the qualitative behaviour of the self and shear noise both as to directivity and relative pitch. Source convection was included in the analysis, and good agreement with measurement was found for field points outside the valley of relative quiet that exists near the jet axis.

The earlier work (e.g., Lighthill, Lilley, loc cit) included source convection (at a fraction M_c of the speed of sound) but neglected small variations in the travel time (the time delay between emission and

reception) across a coherent source region; it predicted a $(1 - M_c\cos\theta)^{-5}$ amplifying 'convection factor' which can be singular for $M_c \geq 1$. Ffowcs Williams (Ref. 11) and Ribner (Ref. 6) showed by different methods that the singularity is removed if the correct time delay is used. According to this factor, source convection at subsonic speeds ($M_c < 1$) strongly biases the noise towards the downstream direction ($\theta \rightarrow 0$). However, refraction bends the sound rays towards the sides to create the peculiar 'valley of quiet' along the jet axis; this gives the overall directivity a heart-shaped appearance.

The role of refraction by the jet velocity and temperature gradients was recognized independently in the United Kingdom (Ref. 12) and in Canada. Ribner's group, in a major series of experiments (Refs. 13, 14), showed that the sound of a pure tone point source placed in a jet flow has a valley of quiet that at each frequency closely matches that of narrow band filtered jet noise centred at the same frequency. Since the pure tone source is omnidirectional when the jet is turned off, this confirms that the valley of quiet in the jet noise must be due to refraction of sound by the mean flow velocity-temperature gradients. Later Schubert (Refs. 15, 16) theoretically predicted similar directivities. The noise in the 'valley of quiet' is low pitched; the pitch increases steadily as the observer moves away from the jet axis; this is just the reverse of what would be expected from simple Doppler shift considerations. However, high frequencies suffer more refraction than low frequencies and are 'bent' further away from the jet axis; this in conjunction with the directional and pitch properties of Ribner's self and shear noise model explains the 'reverse Doppler shift'.

MacGregor et al (Ref 17) demonstrated a viable semi-empirical theory based on Ribner's self and shear noise model (which neglects refraction) incorporating measured or calculated (Refs. 15, 16) refraction corrections. The empiricism of the model correlations is a substitute for a detailed spatial and temporal knowledge of the relevant turbulence parameters, and the a posteriori refraction correction allows for reasonable estimates in the refraction zone.

Refraction is automatically accounted for if a convected wave equation with variable mean flow is considered. An equation of this kind was derived by Phillips and applied to predict the sound from a turbulent supersonic shear flow (Ref. 18). A similar equation has been used in the study of combustion noise (e.g., Ref. 19), although with different dominant source terms. Lilley (Ref. 20) went further and formulated a third order generalized convected wave equation which contrasts with the more traditional second order equations of the previous models. The Lilley equation separates generation effects (sources) from propagation effects more precisely than the Lighthill formalism; thus, despite its complexity, it has come into widespread use (Refs. 21, 22).

The convected wave equation can only be solved analytically for idealized mean flow distributions. Mani's (Ref. 23) model of jet noise generation is one of them. It uses a form equivalent to Lilley's equation, and describes moving quadrupoles in a cylindrical jet embedded in a fluid at rest. In Mani's model the shear term, which in Ribner's model is on the right hand side of the wave equation as a source term, is in effect on the left hand side as a propagation term. Ribner points this out in Ref. 24 and demonstrates that the respective theories, although they differ in the role of the shear term, show comparably good agreement with experiment outside the refraction valley.

Recently recognition of the existence of large-scale coherent structures in jet turbulence has led to analyses (Refs. 24, 26) which suggest that such structures, particularly axisymmetric ones, can be efficient sound radiators. The experimental evidence, however, fails to support this in the case of jet noise. Extensive far-field measurements of Maestrello (Ref. 27) show that two microphones on opposite sides of a jet have very poor signal correlations except at small angles to the axis; thus any axisymmetric components contribute only a small fraction to the total jet noise. Furthermore, Ribner (Ref. 28) has recently shown that his self and shear noise model is capable of predicting two point correlations of the jet noise, in good agreement with measurements by Maestrello, without invoking large scale structures.

An altogether different approach, introduced circa 1958, models the sources as fluid dilatations proportional to fluctuating pressures (pseudosound) in and near the jet flow. Such a source model is implicit in the work of Meecham and Ford (Ref. 29); Corcos and Broadwell (Ref. 30) and Ribner (Ref. 31) formulated the model explicitly. Ribner (Ref. 6) developed the dilatation approach in detail and illustrated phenomena associated with source convection and wave cancellation effects, among others, all of which can also be applied to Lighthill's formalism. The equivalence of the dilatation and Lighthill models has been demonstrated by Ribner (Ref. 6) and acknowledged by Lighthill (Ref. 32).

At first the dilatation theory did not enjoy widespread attention, possibly for lack of detailed experimental information about the pseudosound field of a turbulent jet. On the experimental side there were suspicions that pressure probes locally distort the pseudosound pressure they were intended to measure. Over the years the experimental difficulties have been overcome, and the dilatation theory continues to be the subject of experimental and theoretical investigations (Refs. 33, 34, 35, 36).

1.2 Ribner's Self and Shear Noise Model

Ribner (Refs. 9, 10) developed the Proudman formalism by noting that the instantaneous velocity in the direction of an observer at x in the far field is the sum of a mean velocity U_x and a turbulent velocity $u_x(y,t)$. This leads to two families of sources: one, proportional to $\partial^2 u_x^2/\partial t^2$ contains only the unsteady turbulent velocity. Noise generated by such sources, which are found in all turbulent flows, is called self noise. For the case of isotropic turbulence (assumed in his analysis) sources of the type $2U_x(\partial^2 u_x/\partial t^2)$ can be shown to contribute only if the mean flow possesses shear; hence the name shear noise is associated with this second source term.

Using certain mean flow and turbulence models, Ribner was able to predict the qualitative behaviour of the self and shear noise. The results suggest that the basic self noise is omnidirectional, whereas the shear noise has a dipole-like directivity with lobes pointing along the jet axis. The shear noise spectrum is predicted to peak about one octave below the self noise spectrum; the maximum intensities are comparable. These basic patterns are powerfully altered by convection and refraction effects.

The first extensive comparison of the self and shear noise model with experimental data was performed by MacGregor et al (Ref. 17). More recently Nossier and Ribner (Ref. 37) found good agreement between predicted

and measured narrow-band filtered jet noise directivity patterns and demonstrated that the self and shear noise spectra extracted from far field data of several investigators conformed to the predictions of the theory. The comparisons were restricted to points outside the refraction valley, as the basic theory does not predict refraction.

The surprising lack of spatial coherence of the far field jet noise inferred from measured two point correlations of jet noise (Maestrello, Ref. 27) led Ribner (Ref. 28) to extend his self-shear noise predictive model to deal with two field points (microphones) rather than one. The result was a quite reasonable quantitative fit of the normalized theoretical and measured cross-correlations. The agreement is especially good for the plane at 90° to the jet axis which should be insensitive to convection effects (the model excluded convection effects as a concession to mathematical expediency).

At the present time this is the only theory that has been demonstrated to account for the major features of jet noise for both one and two microphones outside the zone of refraction. The model contains one empirical constant: rather idealized correlations are used and the average temporal scale (or equivalently the Strouhal number) is chosen for best average fit; the Strouhal number is roughly compatible with measurements in jet turbulence.

It can be argued that Lighthill's theory, which underlies all this, describes only an equivalent source distribution and not the 'real' one, since the source integral has been modified by the application of two integral transformations. While the value of the integrals may well be equal, the integrands, which are proportional to the effective source strength distributions, may not be one to one. The dilemma is analogous to the one found in electrostatics, where dissimilar distributions of monopoles and dipoles can result in equivalent electric fields. (A monopole distribution of local strength equal to the minus divergence of a certain dipole distribution will generate the same field.)

Even though Ribner's self and shear noise formalism appears to be a valid description of noise generation by turbulent flows, there has been a lack of conclusive evidence such as furnished by direct measurement of the supposed sources leading to correct prediction of the far field noise. The first serious attempt to measure the self and shear noise was made by Chu (Ref. 38): he measured pertinent two point velocity correlations in a jet flow. The fourth time derivative of these correlations can, in principle, be used to determine the properties of the radiated noise, and perhaps lead to the validation of the self and shear noise model. It was found that multiple differentiation of time domain data is invariably accompanied by a large error. Later Lee and Ribner (Ref. 39) used an idea of Siddon to estimate the combined self and shear noise source strength distribution as well as the far field spectrum from two point cross-correlations between measurements of $v_x^2 = (U_x + u_x)^2$ and radiated sound. Only two differentiations are needed; however, there is a trade-off between the relative ease of data analysis and poor signal to noise ratio, as the cross-correlations by nature possess very small amplitudes. Experimental difficulties finally led Lee to abandon the correlation in favour of the mathematically equivalent cross-spectral density. With the latter approach estimates of the overall source strength distribution and the radiated spectrum were obtained.

Seiner and Reethof (Ref. 40) applied this technique, but with the hot wire signal split into U_x and u_x to extract the apparent self and shear noise source strength distributions. Their measurements, supported by earlier unpublished work of Morris in this laboratory (Ref. 41), appeared to show that the shear noise term dominated the self noise by at least 10 dB, whereas the theory, supported by much indirect evidence from far field jet noise measurements, suggests that the self and shear noise should be comparable in intensity. It was this discrepancy that provided much of the motivation for the present in-depth investigation.

In the direct correlations of the jet flow and jet noise discussed above, the instantaneous jet velocity components U_x and u_x were measured with hot wire probes. The presence of such solid objects - the probe support needles - in a turbulent flow gives rise to noise generated by the unsteady forces that act thereon (Refs. 42, 43). Even though the very weak sound radiated by the hot wire probe is buried in the overall jet noise, the small signal may be well correlated with the flow that impinges on the probe and is measured by it. This implies that the measured correlations of the probe signal and the far field microphone signal could be significantly 'contaminated' by a spurious probe noise contribution. This second possibility further helped motivate the present experimental investigation. (The theoretical expectations for probe-flow interaction are discussed in detail in Appendix B.)

1.3 Present Investigation

The noise generated by the probe-flow interaction will be eliminated when the hot wire anemometer is replaced by a remote sensing scheme such as the Laser Doppler Velocimeter (LDV). Since the demonstration of the Laser Doppler method by Yeh and Cummins in 1964 (Ref. 44), the technique has been refined, and reliable Laser Doppler systems have been available 'off the shelf' for several years.

Knott et al (Ref. 45) have performed parametric LDV studies of a high speed, high temperature, turbulent jet, and also demonstrated that the LDV can be used in cross-correlation measurements of the jet flow and jet noise. The cross-correlation measurement was, however, restricted to a single pair of field points in the jet flow and the far field.

The present investigation is an extension of the work of Lee and Ribner (Ref. 39) and others (Refs. 40, 41) in the field of jet noise diagnostics via cross-correlations. A major difference is the replacement of the hot wire, with its spurious noise, by an LDV. The research program was divided into three tasks:

(i) adaptation of an 'off the shelf' LDV system to the special requirements of a cause and effect experiment,

(ii) identification of possible sources of error that may affect the estimates of the correlation between jet flow and jet noise, as well as validation of the Laser Doppler Velocimeter system,

(iii) direct correlation of the postulated self and shear noise source terms at selected field points in the jet with the radiated sound, and computation of overall self and shear noise spectra based on the correlation measurements.

Assessment of the compatibility of the predicted far-field spectra with measured curves would test whether the self and shear noise model is a self-consistent description of sound generated by turbulent flows.

2. THEORY

2.1 Fundamental Equations

The central equation of noise generation by turbulent flow can be derived from the equations of mass and momentum:

$$\frac{\partial \rho}{\partial t} + \frac{\partial \rho v_j}{\partial y_i} = I_1 = 0 \tag{2.1}$$

$$\rho \frac{\partial v_i}{\partial t} + \rho v_j \frac{\partial v_i}{\partial y_j} + \frac{\partial \tau_{ij}}{\partial y_j} + \frac{\partial P}{\partial y_i} = I_2 = 0 \tag{2.2}$$

ρ is the fluid density, P the pressure, v_i the fluid velocity in the i direction, and τ_{ij} the viscous stress tensor. (i,j) range from 1 to 3, and repeated indices are summed over. The operation:

$$\frac{\partial}{\partial y_i} (I_2 + v_i I_1) - \frac{\partial}{\partial t} I_1 \tag{2.3}$$

combines Eqs. 2.1 and 2.2 into the form:

$$\frac{1}{c_o^2} \frac{\partial^2 P}{\partial t^2} - \nabla^2 P = \frac{\partial^2 \rho v_i v_j}{\partial y_i \partial y_j} + \frac{\partial^2 \tau_{ij}}{\partial y_i \partial y_j} + \frac{1}{c_o^2} \frac{\partial^2}{\partial t^2} (P - c_o^2 \rho) \tag{2.4}$$

after adding $c_o^{-2}\, \partial^2/\partial t^2 (P)$ to both sides (see for example Ref. 6). The left hand side of Eq. 2.4 is the linear wave operator applied to the pressure P(y,t). In a compressible stationary medium, small disturbances propagate at a speed c_o that is characteristic of the medium (Ref. 46). Equation 2.4 therefore can be thought of as describing the sound field of a turbulent flow by an equivalent distribution of sound sources in a quiescent medium (Ref. 1) with no flow and uniform sound speed c_o.

The simplicity of the equation is deceiving, as it allows for all the subtleties of source motion, refraction of sound by mean flow and temperature gradients, and other phenomena. Perturbations in the density ρ for example, in conjunction with mean velocity gradients are responsible for refraction of sound. If the flow is anisentropic (e.g., a heated jet), the term $c_o^{-1}\, \partial^2/\partial t^2 (P - c_o^2 \rho)$ will be nonzero. This causes further refraction and can be a significant source of sound (combustion noise for example). There is no unique description of sound generation by a turbulent flow, as the conservation equations and their solutions may be manipulated in a variety of ways (Refs. 18, 20).

In Lighthill's treatment of a turbulent subsonic jet at ambient temperature the source-like terms are taken to be dominated by $\partial^2 \rho_o v_i v_j / \partial y_i \partial y_j$,

and the features mentioned above are suppressed. The principal contributor to this suppression is the replacement of the variable local density ρ by the constant ambient density ρ_o. Thus, as a first approximation, the sound generated by such a flow is described by the differential equation:

$$\frac{1}{c_o^2}\frac{\partial P}{\partial t^2} - \nabla^2 P \approx \frac{\partial^2 \rho_o v_i v_j}{\partial y_i \partial y_j} \tag{2.5}$$

The pressure at any field point $\underset{\rightarrow}{x}$ and time t is computed by the volume integral (Ref. 47):

$$P(\underset{\rightarrow}{x},t) = P_o + \frac{1}{4\pi}\iiint_V \frac{\delta(t' - t + c_o^{-1}|\underset{\rightarrow}{x} - \underset{\rightarrow}{y}|)}{|\underset{\rightarrow}{x} - \underset{\rightarrow}{y}|}\frac{\partial^2}{\partial y_i \partial y_j}\rho_o v_i v_j(\underset{\rightarrow}{y},t')\, dt' d\underset{\rightarrow}{y} \tag{2.6}$$

The source region is assumed to extend over a volume V that encloses the region of sensible (i.e. measurable) jet flow. The integral sums the contribution of each elementary source at $\underset{\rightarrow}{y}$ in V. The delta function determines the difference between the time of signal emission at $\underset{\rightarrow}{y}$ and signal reception by an observer at $\underset{\rightarrow}{x}$. $|\underset{\rightarrow}{x} - \underset{\rightarrow}{y}|$ is the source-receiver separation.

A mathematically equivalent description is given by:

$$P(\underset{\rightarrow}{x},t) = P_o + \frac{1}{4\pi}\iiint_V \frac{\partial}{\partial y_i}\left[\frac{\delta(t' - t + c_o^{-1}|\underset{\rightarrow}{x} - \underset{\rightarrow}{y}|)}{|\underset{\rightarrow}{x} - \underset{\rightarrow}{y}|}\frac{\partial}{\partial y_j}\rho_o v_i v_j(\underset{\rightarrow}{y},t')\right] dt' d\underset{\rightarrow}{y}$$

$$- \frac{1}{4\pi}\iiint \frac{\partial}{\partial y_i}\left[\frac{\delta(t' - t + c_o^{-1}|\underset{\rightarrow}{x} - \underset{\rightarrow}{y}|)}{|\underset{\rightarrow}{x} - \underset{\rightarrow}{y}|}\right]\frac{\partial}{\partial y_j}\rho_o v_i v_j(\underset{\rightarrow}{y},t')\, dt' d\underset{\rightarrow}{y} \tag{2.7}$$

Application of the divergence theorem (Gauss theorem) shows that the first integral does not contribute to $P(\underset{\rightarrow}{x},t)$, if there are no solid boundaries: the transform into an integral over the bounding surface of V is zero, as the integrand decays faster than r^{-2} for large r. The procedure may be repeated for the remaining integral:

$$P(\underset{\rightarrow}{x},t) = P_o + \frac{1}{4\pi}\iiint_V \rho_o v_i v_j(\underset{\rightarrow}{y},t')\frac{\partial^2}{\partial y_i \partial y_j}\frac{\delta(t' - t + c_o^{-1}|\underset{\rightarrow}{x} - \underset{\rightarrow}{y}|)}{|\underset{\rightarrow}{x} - \underset{\rightarrow}{y}|}\, dt' d\underset{\rightarrow}{y} \tag{2.8}$$

where

$$\frac{\partial^2}{\partial y_i \partial y_j}\frac{\delta(t' - t + c_o^{-1}|\underset{\rightarrow}{x} - \underset{\rightarrow}{y}|)}{|\underset{\rightarrow}{x} - \underset{\rightarrow}{y}|}$$

$$= \frac{1}{|\underset{\rightarrow}{x} - \underset{\rightarrow}{y}|}\left[\frac{(x_i - y_i)(x_j - y_j)}{c_o^2|\underset{\rightarrow}{x} - \underset{\rightarrow}{y}|^2}\frac{\partial^2}{\partial t^2}\delta(t' - t + c_o^{-1}|\underset{\rightarrow}{x} - \underset{\rightarrow}{y}|)\right.$$

$$+\left(\frac{\delta_{ij}}{|\underset{\rightarrow}{x} - \underset{\rightarrow}{y}|} - 3\frac{(x_i - y_i)(x_j - y_j)}{|\underset{\rightarrow}{x} - \underset{\rightarrow}{y}|^2}\right)\left(\frac{1}{c_o}\frac{\partial}{\partial t'}\delta(t' - t + c_o^{-1}|\underset{\rightarrow}{x} - \underset{\rightarrow}{y}|)\right.$$

$$\left.\left. - \frac{1}{|\underset{\rightarrow}{x} - \underset{\rightarrow}{y}|}\delta(t' - t + c_o^{-1}|\underset{\rightarrow}{x} - \underset{\rightarrow}{y}|)\right)\right] \tag{2.9}$$

and

$$\frac{\partial^2}{\partial y_i \partial y_j} \frac{\delta(t' - t + c_o^{-1}|\underset{\rightarrow}{x} - \underset{\rightarrow}{y}|)}{|\underset{\rightarrow}{x} - \underset{\rightarrow}{y}|}$$

$$\approx \frac{1}{|\underset{\rightarrow}{x}|} \cdot \frac{x_i x_j}{|x|^2} \cdot \frac{1}{c_o^2} \cdot \frac{\partial^2}{\partial t'^2} \delta(t' - t + c_o^{-1}|\underset{\rightarrow}{x} - \underset{\rightarrow}{y}|); \quad |\underset{\rightarrow}{x}| \gg |\underset{\rightarrow}{y}| \qquad (2.9A)$$

For an observer outside the flow and sufficiently far away so that $|\underset{\rightarrow}{x} - \underset{\rightarrow}{y}| \approx |\underset{\rightarrow}{x}| \gg$ typical wavelength, the only significant contribution to the acoustic pressure is made by

$$P(\underset{\rightarrow}{x},t) - P_o = \frac{1}{4\pi c_o^2} \frac{1}{|\underset{\rightarrow}{x}|} \iiint_V \frac{x_i x_j}{|\underset{\rightarrow}{x}|^2} \rho_o v_i v_j(\underset{\rightarrow}{y},t) \frac{\partial^2}{\partial t'^2} \delta(t' - t + c_o^{-1}|\underset{\rightarrow}{x} - \underset{\rightarrow}{y}|)dt'd\underset{\rightarrow}{y} \qquad (2.10)$$

since the other terms decay faster than $|\underset{\rightarrow}{x}|^{-1}$.

Noting that $x_i v_i |\underset{\rightarrow}{x}|^{-1} = \underset{\rightarrow}{x} \cdot \underset{\rightarrow}{y} |\underset{\rightarrow}{x}|^{-1} = v_x$ the component of the velocity in the direction of the observer at $\underset{\rightarrow}{x}$, and integrating by parts results in the so-called Proudman formalism:

$$p(\underset{\rightarrow}{x},t) = P(\underset{\rightarrow}{x},t) - P_o = \frac{1}{4\pi c_o^2 |\underset{\rightarrow}{x}|} \iiint_V \frac{\partial^2}{\partial t'^2} \rho_o v_x^2(\underset{\rightarrow}{y},t) \delta(t' - t + c_o^{-1}|\underset{\rightarrow}{x} - \underset{\rightarrow}{y}|) dt'd\underset{\rightarrow}{y} \qquad (2.11)$$

In this particular description only the velocity component in the direction of the observer contributes to the sound heard by the observer. v_x can be measured with considerably less effort than $v_i v_j$ (simultaneous measurement of $v_i v_j$ is a Herculian task), and thus opens the way for experimental verification of the theory via a correlation technique.

Equations 2.10 and 2.11 are the central equations governing the generation of sound by unsteady flows; they are referred to as the Lighthill and Proudman forms, respectively.

2.2 Auto-Correlation and Power Spectral Density of the Far Field Pressure

The instantaneous far field acoustic pressure (the pressure difference from ambient) due to a turbulent jet flow fluctuates above and below zero in a random manner. It is therefore appropriate to characterize the noise by measuring relevant statistical properties such as the auto-correlation function, and the power spectral density of the pressure. The auto-correlation of the far field acoustic pressure is defined to be (Ref. 48):

$$R_{pp}(\underset{\rightarrow}{x},\tau) = p(\underset{\rightarrow}{x},t)\, p(\underset{\rightarrow}{x},t - \tau) = \lim_{T \to \infty} \frac{1}{2T} \int_{-T}^{T} p(\underset{\rightarrow}{x},t)\, p(\underset{\rightarrow}{x},t - \tau)\, dt \qquad (2.12)$$

substituting for $p(x,t)$:

$$R_{pp}(\underset{\rightarrow}{x},\tau) = \lim_{T \to \infty} \frac{1}{2T} \frac{1}{4\pi c_o^2 |\underset{\rightarrow}{x}|} \iiint \frac{\partial^2}{\partial t'^2} \rho_o v_x^2(\underset{\rightarrow}{y},t') \delta(t' - t + c_o^{-1}|\underset{\rightarrow}{x} - \underset{\rightarrow}{y}|)$$

$$p(\underset{\rightarrow}{x},t - \tau)dt'dtd\underset{\rightarrow}{y} \qquad (2.13)$$

In general the velocity v_x is the sum of a mean velocity $U_x = \bar{v}_x$ and a turbulent velocity $u_x = v_x - \bar{v}_x$. The source term expands into

$$\frac{\partial^2 v_x^2}{\partial t^2} = \frac{\partial^2}{\partial t^2}\left(U_x^2 + 2U_x u_x + u_x^2\right) \tag{2.14}$$

The first term is identically zero, hence:

$$R_{pp}(\underset{\rightarrow}{x},\tau) = \frac{1}{4\pi c_o^2 |\underset{\rightarrow}{x}|}\int_V 2U_x(\underset{\rightarrow}{y}) \overline{\frac{\partial^2}{\partial t^2}\rho_o u_x(\underset{\rightarrow}{y},t)\; p(\underset{\rightarrow}{x},t - \tau + c_o^{-1}|\underset{\rightarrow}{x} - \underset{\rightarrow}{y}|)}\; d\underset{\rightarrow}{y}$$

$$+ \frac{1}{4\pi c_o^2 |\underset{\rightarrow}{x}|}\int_V \overline{\frac{\partial^2}{\partial t^2}\rho_o u_x^2(\underset{\rightarrow}{y},t)\; p(\underset{\rightarrow}{x},t - \tau\, c_o^{-1}|\underset{\rightarrow}{x} - \underset{\rightarrow}{y}|)}\; d\underset{\rightarrow}{y} \tag{2.15}$$

For steady jet flow u_x, u_x^2, and p are statistically stationary random variables (Ref. 49), so that

$$R_{pp}(\underset{\rightarrow}{x},\tau) = \frac{\rho_o}{2\pi c_o^2 |\underset{\rightarrow}{x}|}\int_V U_x(y) \overline{\frac{\partial^2}{\partial \tau^2} u_x(\underset{\rightarrow}{y},t)\; p(\underset{\rightarrow}{x},t - \tau + c_o^{-1}|\underset{\rightarrow}{x} - \underset{\rightarrow}{y}|)}\; d\underset{\rightarrow}{y}$$

$$+ \frac{\rho_o}{4\pi c_o^2 |\underset{\rightarrow}{x}|}\int_V \overline{\frac{\partial^2}{\partial \tau^2} u_x^2(\underset{\rightarrow}{y},t)\; p(\underset{\rightarrow}{x},t - \tau + c_o^{-1}|\underset{\rightarrow}{x} - \underset{\rightarrow}{y}|)}\; d\underset{\rightarrow}{y} \tag{2.16}$$

The far field acoustic pressure auto-correlation is the sum of two volume integrals. At $\tau = 0$, the integrals describe the mean square pressure. Ribner (Ref. 10) has called the two contributions shear and self noise respectively. This kind of division was first suggested by Lilley (Ref. 5), but with different definitions.

Following the notion of Siddon (Ref. 50), one may think of these cross-correlations as causality correlations, as they compare the supposed source terms $[2U_x\, \partial^2/\partial t^2(u_x),\ \partial^2/\partial t^2(u_x^2)]$ with the effect they produce. The correlations have dimensions of a mean square pressure per unit volume and describe the sound radiated by a correlation volume about the source point. A single correlation volume, therefore, contributes a small amount to the mean square pressure. If one assumes that there are N such correlation volumes of equal strength ($\Delta V \cdot N = V$), then it follows that the normalized peak correlation coefficient is of order $1/\sqrt{N}$ (see Appendix A for a more detailed mathematical analysis).

The Wiener-Khinchin theorem states that the auto-correlation function and the power spectral density are Fourier transform pairs (Ref. 51):

$$R_{pp}(\underset{\rightarrow}{x},\tau) = \int_{-\infty}^{\infty} \varphi_{pp}(\underset{\rightarrow}{x},\omega)\; e^{-i\omega\tau}\; d\omega \tag{2.17}$$

The power spectral density $\varphi_{pp}(\underset{\rightarrow}{x},\omega)$ can be determined from Eq. 2.12 by taking the inverse Fourier transform:

$$\varphi_{pp}(\underset{\rightarrow}{x},\omega) = \frac{1}{2\pi}\int R_{pp}(\underset{\rightarrow}{x},\tau)e^{i\omega\tau}\, d\omega \tag{2.18}$$

Substituting for $R_{pp}(x,\tau)$:

$$\varphi_{pp}(\underset{\rightarrow}{x},\omega) = \frac{\rho_o}{4\pi^2 c_o^2 |\underset{\rightarrow}{x}|}\iiint_V U_x(\underset{\rightarrow}{y})\frac{\partial^2}{\partial\tau^2}\overline{u_x(\underset{\rightarrow}{y},t)p(\underset{\rightarrow}{x},t-\tau+c_o^{-1}|\underset{\rightarrow}{x}-\underset{\rightarrow}{y}|)}\, e^{i\omega\tau}\, d\tau d\underset{\rightarrow}{y}$$

$$+\frac{\rho_o}{8\pi^2 c_o^2 |\underset{\rightarrow}{x}|}\iiint_V \frac{\partial^2}{\partial\tau^2}\overline{u_x^2(\underset{\rightarrow}{y},t)p(\underset{\rightarrow}{x},t-\tau+c_o^{-1}|\underset{\rightarrow}{x}-\underset{\rightarrow}{y}|)}\, e^{i\omega\tau}\, d\tau\, d\underset{\rightarrow}{y} \tag{2.19}$$

After integration by parts:

$$\varphi_{pp}(\underset{\rightarrow}{x},\omega) = -\frac{\rho_o}{2\pi c_o^2 |\underset{\rightarrow}{x}|}\int_V \omega^2 U_x(\underset{\rightarrow}{y})\,\varphi_{u_x p}(\underset{\rightarrow}{x},\underset{\rightarrow}{y},\omega)\, e^{i\omega c_o^{-1}|\underset{\rightarrow}{x}-\underset{\rightarrow}{y}|}\, d\underset{\rightarrow}{y}$$

$$-\frac{\rho_o}{4\pi c_o^2 |\underset{\rightarrow}{x}|}\int_V \omega^2\,\varphi_{u_x^2 p}(\underset{\rightarrow}{x},\underset{\rightarrow}{y},\omega)\, e^{i\omega c_o^{-1}|\underset{\rightarrow}{x}-\underset{\rightarrow}{y}|}\, d\underset{\rightarrow}{y} \tag{2.20}$$

where

$$\varphi_{u_x p}(\underset{\rightarrow}{x},\underset{\rightarrow}{y},\omega) = \frac{1}{2\pi}\int \overline{u_x(\underset{\rightarrow}{y},t)\, p(\underset{\rightarrow}{x},t-\tau)}\, e^{i\omega\tau}\, d\tau \tag{2.21}$$

and

$$\varphi_{u_x^2 p}(\underset{\rightarrow}{x},\underset{\rightarrow}{y},\omega) = \frac{1}{2\pi}\int \overline{u_x^2(\underset{\rightarrow}{y},t)\, p(\underset{\rightarrow}{x},t-\tau)}\, e^{i\omega\tau}\, d\tau \tag{2.22}$$

The power spectral density of the far field sound pressure is expressed by Eqs. 2.20 to 2.22 as a volume integral of two weighted cross-spectral density functions $\varphi_{u_x p}(\underset{\rightarrow}{x},\underset{\rightarrow}{y},\omega)$ and $\varphi_{u_x 2p}(\underset{\rightarrow}{x},\underset{\rightarrow}{y},\omega)$. The double differentiation with respect to τ in the time domain is equivalent to multiplication by $-\omega^2$ in the frequency domain (Ref. 52), a property that will be used in the analysis of the measured data.

The cross-correlation functions $R_{u_x p}(\underset{\rightarrow}{x},\underset{\rightarrow}{y},\tau) = \overline{u_x(\underset{\rightarrow}{y},t)\, p(\underset{\rightarrow}{x},t-\tau)}$ and $R_{u_x 2p}(\underset{\rightarrow}{x},\underset{\rightarrow}{y},\tau) = \overline{u_x^2(\underset{\rightarrow}{y},t)\, p(\underset{\rightarrow}{x},t-\tau)}$ as well as the cross-spectral densities $\varphi_{u_x p}(\underset{\rightarrow}{x},\underset{\rightarrow}{y},\omega)$ and $\varphi_{u_x 2p}(\underset{\rightarrow}{x},\underset{\rightarrow}{y},\omega)$ can be estimated by direct measurement. Both representations contain the same information, and it is often a matter of convenience which one is to be used. For each position $\underset{\rightarrow}{x}$ the above functions must be defined over all values of $\underset{\rightarrow}{y}$, τ, or ω.

As turbulence levels vary slowly with position in the jet, the volume integrals 2.16 and 2.20 may be approximated by a suitably weighted summation over a finite number of source points. The weighting is a measure of the effective volume over which the single estimate is a reasonable approximation to the integrand. For example, the expression

$$R_{pp}(\underset{\rightarrow}{x},\tau) \cong \frac{\rho_o}{2\pi c_o^2 |\underset{\rightarrow}{x}|} \sum_{n=1}^{N} U_x(\underset{\rightarrow}{y}_n) \frac{\partial^2}{\partial \tau^2} R_{u_x p}(\underset{\rightarrow}{x},\underset{\rightarrow}{y}_n,\tau') \Bigg|_{\tau - c_o^{-1}|\underset{\rightarrow}{x}-\underset{\rightarrow}{y}_n|} \Delta V_n^{(1)}$$

$$+ \frac{\rho_o}{4\pi c_o^2 |\underset{\rightarrow}{x}|} \sum_{m=1}^{M} \frac{\partial^2}{\partial \tau'^2} R_{u_x^2 p}(\underset{\rightarrow}{x},\underset{\rightarrow}{y}_m,\tau') \Bigg|_{\tau - c_o^{-1}|\underset{\rightarrow}{x}-\underset{\rightarrow}{y}_m|} \Delta V_m^{(2)} \qquad (2.23)$$

estimates the auto-correlation of the acoustic pressure from measured 'causality correlations' of the postulated sources (as described by Ribner's self and shear noise formalism) and the far field pressure.

The time domain estimates are very susceptible to signal to noise problems because of the small amplitudes of the cross-correlations. On going over to the frequency domain, the transform

$$\varphi_{pp}(\underset{\rightarrow}{x},\omega) \triangleq - \frac{\rho_o}{2\pi c_o^2 |\underset{\rightarrow}{x}|} \sum_{n=1}^{N} U_x(\underset{\rightarrow}{y}_n) \omega^2 \varphi_{u_x p}(\underset{\rightarrow}{x},\underset{\rightarrow}{y}_n,\omega) e^{i\omega c_o^{-1}|\underset{\rightarrow}{x}-\underset{\rightarrow}{y}_n|} \Delta V_n^{(1)}$$

$$- \frac{\rho_o}{4\pi c_o^2 |\underset{\rightarrow}{x}|} \sum_{m=1}^{M} \omega^2 \varphi_{u_x^2 p}(\underset{\rightarrow}{x},\underset{\rightarrow}{y}_m,\omega) e^{i\omega c_o^{-1}|\underset{\rightarrow}{x}-\underset{\rightarrow}{y}_m|} \Delta V_m^{(2)} \qquad (2.24)$$

describes the power spectrum of the far field pressure as a summation of measured cross-spectral densities. The differentiations with respect to τ of the time domain data will invariably result in more errors, whereas multiplication by $-\omega^2$ should only alter the shape of the cross-spectral densities, which are likely to be smooth functions of frequency.

The measurement of the 'causality' correlations and the cross-spectral densities is one of the major objectives of this investigation. Should the experimental results be demonstrated to be compatible with the above equations, then the self and shear noise model becomes a more credible description of the noise generation of turbulent jets.

It must be emphasized that the measured cross-correlation and cross-spectral densities are not estimates of a unique source distribution: they are but estimates of one of a number of mathematically equivalent source patterns. The overall contribution to the far field sound pressure from such equivalent source distributions are identical.

The relative intensity and directivity of the self and shear noise have been predicted theoretically (Ref. 10) using certain models to describe the statistics of the turbulence. The self noise (assuming isotropic turbulence) is omnidirectional and the directional pattern of the shear noise is dipole-like, with the lobes pointing along the jet axis. The basic overall directivity is significantly modified by source convection and refraction (Refs. 13, 14, 15, 16). Refraction of sound by a jet flow is generally significant only for angles less than 40° from the jet axis. Any experiment designed to detect a cause-effect relationship between the principal source term and the radiated far field sound pressure should avoid measurements in that region, unless it or the theory incorporates a correction for refraction.

3. EXPERIMENTAL FACILITIES: DEVELOPMENT AND ARRANGEMENT

A considerable portion of the project has been devoted to the development of a Laser Doppler Velocimeter (LDV) system that could meet the constraints imposed by the nature of the experiment:

(i) the system should not interfere with the flow field nor the sound field,

(ii) the frequency response should extend to the upper audio range,

(iii) the seeding generator needed to supply a sufficient number of scattering agents for the Laser Doppler Velocimeter must be very quiet.

The development of the latter proved to be a rather time-consuming endeavour.

3.1 Laser Doppler Velocimeter

3.1.1 Operating Principle

A small particle travelling with a non-relativistic velocity $\underset{\rightarrow}{v}_p = \partial y/\partial t$ crosses a light beam of frequency ν_o and wave number vector $\underset{\rightarrow}{k}_1$, $|\underset{\rightarrow}{k}_1| = 2\pi\,\nu_o/c$, and scatters the spherical wave described by

$$E_{SCAT}(\underset{\rightarrow}{x},\underset{\rightarrow}{y},t) = \frac{SE_o}{ik|\underset{\rightarrow}{x} - \underset{\rightarrow}{y}|}\, e^{-i(2\pi\nu_o t - \underset{\rightarrow}{k}_1\cdot\underset{\rightarrow}{y})}\, e^{ik|\underset{\rightarrow}{x}-\underset{\rightarrow}{y}|} \tag{3.1}$$

to the observer at $\underset{\rightarrow}{x}$ in the far field. S is a directivity factor that depends on the particle size, refractive index, and the incident radiation (Ref. 53); k is the scattered wave number. The far-field approximation is:

$$E_{SCAT}(\underset{\rightarrow}{x},\underset{\rightarrow}{y},t) \approx A_p\, e^{-i\left[2\pi\nu_o t + \left(k\frac{\underset{\rightarrow}{x}}{|\underset{\rightarrow}{x}|} - \underset{\rightarrow}{k}_1\right)\cdot\underset{\rightarrow}{y}\right]} \tag{3.2}$$

where

$$A_p = \frac{SE_o}{k|\underset{\rightarrow}{x}|}\, e^{i\left(k|\underset{\rightarrow}{x}| - \frac{\pi}{2}\right)}$$

If a second beam of light of the same frequency ν_o but with a different wave vector is scattered simultaneously, then the signal at $\underset{\rightarrow}{x}$ becomes:

$$E_{\substack{SCAT \\ TOTAL}}(\underset{\rightarrow}{x},\underset{\rightarrow}{y},t) = A_p \left\{ e^{-i\left[2\pi\nu_o t + \left(k \frac{\underset{\rightarrow}{x}}{|\underset{\rightarrow}{x}|} - \underset{\rightarrow}{k}_1 \right) \cdot \underset{\rightarrow}{y} \right]} + e^{-i\left[2\pi\nu_o t + \left(k \frac{\underset{\rightarrow}{x}}{|\underset{\rightarrow}{x}|} - \underset{\rightarrow}{k}_2 \right) \cdot \underset{\rightarrow}{y} \right]} \right\} \tag{3.3}$$

It has been assumed that S varies sufficiently slowly over the range $\theta = \tan^{-1}(|k_1 - k_2|/2|k_1 + k_2|)$ to be represented by a constant. The expression $E_{\substack{SCAT \\ TOTAL}}$ can be rewritten in the form of an amplitude modulated signal:

$$E_{\substack{SCAT \\ TOTAL}} = A_p e^{-i\left[2\pi\nu_o t - \left(k \frac{\underset{\rightarrow}{x}}{|\underset{\rightarrow}{x}|} - \underset{\rightarrow}{k}_1 \right) \cdot \underset{\rightarrow}{v}_p t \right]} \left(1 + e^{-i(\underset{\rightarrow}{k}_2 - \underset{\rightarrow}{k}_1)\underset{\rightarrow}{v}_p t} \right) \tag{3.4}$$

The first term is a wave with frequency

$$\nu = \nu_o + \frac{1}{2\pi}\left(k \frac{\underset{\rightarrow}{x}}{|\underset{\rightarrow}{x}|} - \underset{\rightarrow}{k}_1 \right) \underset{\rightarrow}{v}_p \approx \nu_o, \qquad |\underset{\rightarrow}{v}_p| \ll c \tag{3.5}$$

and can be thought of as the high frequency carrier signal. The amplitude modulation consists of a DC component and a time varying signal with frequency

$$\nu_D = \frac{1}{2\pi} (\underset{\rightarrow}{k}_2 - \underset{\rightarrow}{k}_1) \cdot \underset{\rightarrow}{v}_p \tag{3.6}$$

The latter is the so-called Doppler signal; it is actually the difference of the two Doppler frequencies that are generated by the scattering process. The frequency ν_D, which is much lower than ν, can be detected by a photomultiplier and measured by conventional frequency analyzers or high speed counters. The Doppler frequency:

$$\nu_D = \frac{1}{2} (\underset{\rightarrow}{k}_2 - \underset{\rightarrow}{k}_1) \cdot \underset{\rightarrow}{v}_p$$

is unique to the system and varies linearly with the speed of the particle in the direction of the $\underset{\rightarrow}{k}_2 - \underset{\rightarrow}{k}_1$ vector.

$$\begin{aligned} \nu_D &= \frac{1}{2\pi} |\underset{\rightarrow}{k}_2 - \underset{\rightarrow}{k}_1| \cdot |\underset{\rightarrow}{v}_p| \cdot \cos\phi \\ \nu_D &= \frac{2}{\lambda_o} \sin\theta |\underset{\rightarrow}{v}_p| \cos\phi \end{aligned} \tag{3.7}$$

The sense of direction is lost, but can be recovered by a system that uses frequency shift techniques.

For a more heuristic description consider the intersection of two coherent light beams. At the beam intersection an interference pattern is created (Fig. 3.1). The angle of intersection and the wavelength of the light determine the fringe spacing:

$$d_f = \frac{\lambda}{2} \left(\sin \theta\right)^{-1} \tag{3.8}$$

A small particle crossing the fringe pattern will scatter a modulated signal, the frequency of which is determined by the fringe spacing and the particle velocity normal to the fringes. The scattered light is then collected on the first dynode of a photomultiplier tube (Fig. 3.2). This type of signal detection is known as the differential mode. A phase-locked loop or a high speed counter can be used to estimate the Doppler frequency which is directly proportional to the particle speed normal to the fringe pattern. There is no linearization required, as is the case with the hot wire anemometer. Aside from small scattering agents, the flow remains unaffected by the measurement. The remote sensing eliminates any probe-flow interaction which may generate an unwanted, but well correlated, sound signal. A comprehensive survey of the operating principles, advantages, and limitations of the LDV can be found in Refs. 54 and 55.

3.1.2 Optical Package

The optical arrangement has been built up from standard DISA components consisting of a 55L84 Beam Splitter, 55L87 Beam Separator and Focusing Lens, and a 55L12 Photomultiplier, as shown by the schematic representation in Fig. 3.3. For minimum acoustic interference a long range back-scatter system would have been preferable. Small particles that follow the turbulent flow most faithfully, scatter the incident beam in the forward direction; therefore, the differential mode of light collection (Fig. 3.2) offers a better signal strength (Ref. 56).

The space available in the anechoic room restricted the focal lengths of the optics to be 30 cm. In order to minimize acoustical interference, all optical components have been moved as far away from the flow as possible, subject to spatial and vibrational constraints.

After several design iterations a self-contained optical package was built. The system can be easily aligned and allows the beam intersection to be placed virtually anywhere in the jet flow. There are two main components: the traversing gear and the basic optical system (Fig. 3.4).

The X-Y traversing gear provides a stable platform for the Laser Doppler optical system. The traversing gear has a range of travel of 30 cm along the jet axis and 20 cm laterally to it. An aluminum U channel beam supports the beam splitter optics and the photomultiplier assembly. The horizontal support is attached to the traversing gear via a "Lazy Susan' bearing, providing the capability to rotate the entire assembly about the probe volume. This feature makes the measurement of v_x possible. The

support beam also serves as a platform for a Spectra Physics 124A 15 mW He-Ne laser (632.8 nm). Two front surface mirrors on adjustable mountings steer the laser beam into the beam splitter optics 75 cm above the laser. The beam splitter and upper steering mirror are attached to a bracket whose vertical position can be adjusted. A carrier with lateral and vertical travel holds the receiving optics and the photomultiplier in place. The support rests on a 50 cm optical bench. This arrangement assures precise alignment of the photomultiplier with the probe volume. Four locating rings, epoxied on the support beam, lock the optical bench in the correct position. The optical bench also serves as a counterweight for the beam splitter optics, so that there is no external torque on the traversing gear. The entire system is quite stable, and only severe shocks will result in misalignment. Prior to installation in the anechoic room the laser and the optical path to the beam splitter were covered with a cardboard mantle to reduce dust accumulation on the mirrors. Figure 3.5 shows the optical system after installation in the anechoic room. When aligned to measure the velocity component at 40° to the jet axis, the beam splitter optics are just upstream of the nozzle, thereby eliminating any interference with sound radiated in the direction of the microphone.

3.1.3 Laser Doppler Processor

The detected Doppler signals are analyzed by a DISA 55L90 counter processor. The 55L90 is a sophisticated high speed electronic counter capable of resolving 5 nsec intervals (100 MHz). The photomultiplier signal is conditioned by adjustable high and low pass filters. The high pass removes the so-called Doppler pedestal which does not contain any velocity information. The low pass filter improves the signal to noise ratio of the Doppler signal by minimizing the noise bandwidth of the photomultiplier shot noise.

A high speed Schmitt trigger converts the filtered Doppler signal to a square wave that is compatible with the digital counter circuitry used to measure the time ΔT taken by a single particle to cross 8 fringes in the probe volume, defined by the beam intersection.

The reciprocal of ΔT is 8 times the Doppler frequency which is directly proportional to the particle speed. The latter is available at the output of a digital to analog converter. The DAC holds the old output level until a new valid velocity measurement has been performed. A 10 MHz Doppler signal can generate new output data at the rate of 625,000 samples per second.

In practice the number of particles that cross the probe volume per unit time and the orientation of the probe volume with respect to the mean flow direction govern the data rate (Appendix D). The main sources of error in the velocity estimates are large particles that do not follow the flow, but scatter a large amount of light, particles that cross less than eight fringes and multiple particles in the probe volume. An internal validation system minimizes the errors caused by these invalid signals. For optimum data acquisition both the data rate and the percentage of valid data contained in the input signal must be large. In this instance the best use is made of particles that pass through the probe volume. A digital subsystem of the processor displays the output data rate as well as the validation percentage. Both these parameters were carefully monitored during each experiment.

3.1.4 Seeding Generator

In order to assure a high data rate, a proportionately large number of scattering particles must cross the probe volume. A wide variety of particles and particle generators can be used (Ref. 57). In this particular application, the particle generator had to be efficient as well as quiet. A great deal of effort was devoted to the development of such a device, culminating in two particle generators.

The first seeding generator uses commercially available .5 μm alumina polishing powder as the scattering agents. The particles are kept in a holding tank (Fig. 3.6). A small air jet stirs the air above the particles and some of them are carried away with the exhaust flow. The point of particle injection is just ahead of the entrance to the model jet plenum. A fine stainless steel screen serves as a filter to reduce the chance of particle coagulation. The particle concentration at the nozzle was uniform, and data rates in excess of 60 KHz were measured as far downstream as 7 jet diameters. It was found, however, that the alumina particles would migrate into the control room and adjacent laboratory space. The serious health hazard posed by the fine alumina dust prevented use of this particle generator.

By far the safest seeding material is water, since the water droplets eventually evaporate. Yanta et al (Ref. 58), for example, used water droplets to seed a supersonic flow. The most efficient method of generating water droplets is the process of atomization. Liquid is drawn into the low pressure region of a high speed jet flow, and the shear action of the flow breaks off small droplets. The size and concentration of the particles is a function of the jet velocity and the position and diameter of the liquid supply line.

To assure a large particle concentration, the jet must possess a large injector effect. This can be achieved with a high speed jet, making it necessary to find the best compromise between efficiency and minimal noise generation. It was found that the nozzle of the atomizing jet could be very small without affecting the particle concentration. The small jet diameter assured that the atomizer would radiate a negligible amount of noise; as is suggested by the U^8D^2 acoustic power law. The final design is illustrated in Fig. 3.7. The atomizer consists of a miniature jet connected to a variable high pressure air supply. The liquid supply line is terminated in a No. 19 stainless steel hypodermic tube and positioned along the jet axis until optimum seeding conditions have been reached.

The procedure is one of trial and error. The air jet has a sufficiently large injector effect to allow the particle generator to be self starting. The seeding generator is placed in the upstream end of the model jet plenum. In static tests the plume of the minijet spread to the walls of the plenum in a distance of 30 cm. This is not expected to be much different when the model jet is turned on.

The heavier droplets settle more quickly, strike the walls of the plenum, and are collected in two drains. The atomizer fluid is stored in an airtight glass jar outside the plenum. A pressure equalization line maximizes the pressure drop between the reservoir and the miniature jet. Based on the amount of water collected in the drains, it is estimated that the atomizer has an efficiency of 70%. There is also some loss due to evaporation, reducing

the efficiency. Nevertheless, data rates were found to be consistently above 20 KHz at all locations where velocity measurements used in the cross-correlations were performed. The overall water consumption was 3.3l/hour.

3.2 Analog Squaring Module

3.2.1 Non-Ideal Behaviour of Analog Multipliers

An analog multiplier was used to compute the signal proportional to $u_x^2(\underline{y},t)$. A typical analog multiplier in the squaring mode is described by the equation:

$$V_{u^2} = \frac{1}{10V} (V_u)^2 + \gamma \frac{\partial V_u}{\partial t} \tag{3.9}$$

where V_u is the input voltage and V_{u2} the output voltage. The second term is often referred to as AC feed-through. The factor γ is a function of frequency and signal amplitude.

Even high performance multipliers suffer from AC feed-through. In many instances the non-ideal behaviour can be tolerated as a negligible error. This does not apply to cross-correlation experiments. The input voltage V_u is proportional to the velocity $u_x(\underline{y},t)$, the constant of proportionality being the sensitivity of the transducer system:

$$V_u = k_u \, u_x(\underline{y},t) \tag{3.10}$$

The cross-correlation function of V_{u2} and the pressure signal V_p is:

$$\overline{V_{u^2} V_p} = \frac{1}{10V} k_u^2 k_p \, \overline{u_x^2 p} + \gamma \, k_u k_p \frac{\partial}{\partial \tau} \overline{u_x p} \tag{3.11}$$

and the cross-spectral density function is:

$$\varphi_{V_{u^2} V_p} = \frac{1}{10V} k_u^2 k_p \, \varphi_{u_x^2 p}(\omega) - i\gamma \, k_u k_p \omega \, \varphi_{u_x p}(\omega) \tag{3.12}$$

In order to assure a good estimate of $\varphi_{u_x^2 p}(\omega)$, the leading term must dominate at all frequencies:

$$\frac{k_u}{10V} \frac{\varphi_{u_x^2 p}(\omega)}{\varphi_{u_x p}(\omega)} \gg \gamma\omega \tag{3.13}$$

From theoretical considerations it can be shown that

$$\frac{\varphi_{u_x^2 p}(\omega)}{\varphi_{u_x p}(\omega)} = 2U_x \mathcal{F}(\omega) \tag{3.14}$$

where $\mathcal{F}(\omega)$ is the ratio of the self and shear noise spectra. If the inequality

$$2\frac{k_{u_x}}{10V}\mathcal{F}(\omega) = \frac{2V_{u_x}}{10V}\mathcal{F}(\omega) \gg \gamma\omega \qquad (3.15)$$

is not satisfied, then the estimate of the cross-spectral density $\Phi_{u_x 2p}$ as well as the cross-correlation $R_{u_x 2p}$ will be in error.

3.2.2 Squaring Circuit

As discussed above, analog multipliers are not ideal elements, but suffer from AC feed-through. After testing several other models, a Burr-Brown 4206 multiplier was selected on the basis of good AC feed-through rejection. In order to assure that the criterion stated in Eq. 3.15 is always satisfied, the performance of the multiplier has been improved. The AC feed-through can be eliminated if a signal equal to $-\gamma\ \partial/\partial t\ (V_u)$ is added to the output of the multiplier. As γ is a function of signal amplitude, one can only hope for limited success. The circuit diagram of the squaring module with AC feed-through correction is shown in Fig. 3.8. The multiplier has least error, when it is operated in a negative quadrant ($V_x \cdot V_y$ is always negative). The basic squarer is built up from a buffer amplifier Q_1 and a unity gain inverter Q_2 connected to the X and Y inputs of the 4206 respectively. A differentiator followed by a variable gain amplifier (Q_3 to Q_5) computes the error signal to be added to the output of the squarer. Summing amplifier Q_6 performs the addition. Switch S_1 allows the basic squarer to be adjusted independently of the error compensating network. A relative improvement of 10 dB is achieved over a wide range of frequencies, when the system is properly trimmed (Fig. 3.9).

3.3 Acoustical System

3.3.1 Anechoic Room

All measurements were performed in the anechoic room at the University of Toronto Institute for Aerospace Studies. The anechoic room has dimensions 4.2 x 2.9 x 2.1 m^3 between the tips of the fibreglass wedges which have a wedge depth of 20 cm. A .32 mm thick lead sheet provides extra transmission loss for external sound that may be transmitted through the concrete walls. The cut-off frequency of the room (defined by deviation from the 1/r law) is approximately 300 Hz. The background noise level is less than 28 dBA.

A fibreglass lined duct (.75 x .75 m^2 cross-sectional area) serves as an exhaust for the model jet installed in the anechoic room. All equipment is wrapped in fibreglass, to eliminate excessive reflections. A detailed description of the anechoic room can be found in Ref. 59.

3.3.2 Model Air Jet

The model air jet used in the experiments is capable of producing nozzle velocities from 10 m/sec to 300 m/sec. The nozzle has an exit diameter of 1.91 cm (3/4 in) and the area ratio (the square of the ratio of the plenum diameter most upstream of the nozzle and the orifice diameter) is 110. The nozzle contour has been designed to provide slug flow at the orifice (Ref. 59). A 1 m long steel pipe acts as a plenum.

The model air jet is connected to a fibreglass-lined muffler in the control room via a flexible air hose. The muffler isolates the jet from an adjustable two stage pressure regulator. A compressor supplies 70 to 100 psi air to the system. The compressed air is passed through a water trap and regulated down to 60 psi by the first regulator stage. The second stage is a Fisher Type 99 Regulator with feedback stabilization. Cross-correlations of the valve noise of the regulators and the jet noise indicate that the muffler and the flexible air line provide complete acoustic isolation from valve noise.

The static pressure upstream of the nozzle is monitored by a mercury manometer. All cross-correlation experiments were performed at a static head of 50 mm Hg, corresponding to a jet velocity of 105 m/sec.

3.3.3 Microphone System

A Bruel & Kjaer 1/2" condenser microphone served as the pressure transducer. The 1/2" microphone type 4334 is the best compromise between sensitivity (12.5 mV/Pa) and frequency response (4 Hz to 40 KHz). The microphone is coupled to a Bruel & Kjaer 2619 FET preamplifier driven by a Bruel & Kjaer 2801 microphone power supply via a special low capacitance 10 m extension cable. A 2.5 m long balanced aluminum T beam supports the microphone and preamplifier assembly. The microphone boom can be rotated about its vertical axis which is aligned with the jet centre line and the nozzle exit plane. The microphone is located in the horizontal plane of the jet at a distance of 1.60 m from the jet nozzle and at an angle of 40° to the jet axis, when cross-correlation experiments are performed. The average time delay between the time of emission of the signal in the jet flow and reception at the microphone is 4.5 msec.

Careful attention has been paid to eliminate ground loops caused by possible electrical contact of the microphone system with its metal supports. A Keithley Model 102 B decade isolation amplifier boosts the low level microphone signal by a factor of 80. The 1/2" microphone limits the overall frequency response to be 4 Hz to 40 KHz.

3.4 Hot Wire Anemometer

A Thermosystems TSI 1034 A linearized anemometer was used to measure the turbulence and the mean flow characteristics of the model air jet. These measurements served as reference data. The anemometer has a frequency response from DC to 16 KHz, measured by the sine wave method (Ref. 60). All measurements were performed with hot film probes type 1210 AG - 10 featuring a .0254 mm sensor diameter and a 1.27 mm sensor length. These particular probes have been developed by Lee (Ref. 61) and reduce the probe flow interference found in conventional short stem hot film probes.

The water trap of the air supply to the model jet does not remove very small oil droplets that are picked up by the air in the compressor stage. The particle concentration is not significant; however, when a hot film probe is exposed to the jet flow for an extended period of time, it is covered by a baked-on oil film. After use, the sensors were cleaned with a fine brush dipped in Varsol; the solvent combined with a gentle brushing action removed the oil film. The hot film probes are surprisingly rugged and can stand up to repeated vigorous cleansing.

3.5 Signal Processing Instrumentation

Two principal computation instruments were used during the investigation: a Princeton Applied Research 101 Correlation Function Computer and a Spectral Dynamics DSP 360 signal processor.

3.5.1 PAR 101 Correlation Function Computer

The PAR 101 is a hybrid (part analog, part digital) instrument that computes a running time average of 100 lag products. The result is an estimate of the correlation function at 100 equally spaced points in the time span $\tau = T_o$ to $\tau = T_o + T$. The precomputation delay T_o can be varied in integral steps of T, the delay range. The integration time of the RC averagers is adjustable. In order to be able to measure correlations as low as .005, it is necessary to use a 400 sec integration time and wait for at least 4 time constants before sampling the output. The inherent noise floor of the instrument makes it impossible to detect correlations with correlation coefficients less than .002.

3.5.2 Spectral Dynamics Digital Signal Processor 360 (DSP 360)

The DSP 360 is a two channel fast Fourier transform computer capable of performing cross-spectral density and cross-correlation function estimates. This particular instrument became available in the later stages of the investigation. All Laser Doppler Velocimeter based measurements were analyzed with the DSP 360.

The fast Fourier transform computer estimates the cross-spectral density directly (Appendix C), resulting in a significant decrease of computation time, when compared to the method employed by Lee (Ref. 61). Memory limitations restrict the number of averages that can be performed on the output data to 4096, equivalent to a 100 sec averaging time, when a 0 to 12 KHz analysis range is selected.

Despite the averaging, the cross-spectral density functions were not free from noise. It was found that the cross-spectral density estimates could be analyzed with least error, when they were displayed in an amplitude-phase angle format. Such a display allows direct multiplication by f^2, if the function is plotted against logarithmic frequency.

For computational reasons, the analyzer uses only half the amount of data, when estimates of correlations are being computed. The decrease is effective averaging time brings about a poorer signal to noise ratio for the cross-correlation functions.

3.5.3 Ancillary Instrumentation

In order to be able to normalize the correlation functions, the RMS voltages of the input signals must be known. The input voltages to the correlation computers were measured with two Bruel & Kjaer 2417 Random Noise Voltmeters, each with a 100 sec integration time. The RMS voltages also served as a check on possible drift in the measuring instrumentation. The computed correlations and spectra were drawn by a Mosely 2D4 X-Y recorder. The hard-copy output data formed the basis for further data analysis.

4. EXPERIMENTAL CONSIDERATIONS AND CROSS-CHECKS

Before attempting to measure the cross-correlations and cross-spectral densities, it is necessary to account for mechanisms, other than described by the theory, that are capable of affecting the cross-correlations/spectra. Some of these can be minimized, others, hopefully, are not significant. The main sources of error that are likely to occur during the estimation of the functions $R_{u_x p}(\underset{\rightarrow}{x},\underset{\rightarrow}{y},\tau)$, $R_{u_x 2p}(\underset{\rightarrow}{x},\underset{\rightarrow}{y},\tau)$, $\Phi_{u_x p}(\underset{\rightarrow}{x},\underset{\rightarrow}{y},\omega)$, and $\Phi_{u_x 2p}(\underset{\rightarrow}{x},\underset{\rightarrow}{y},\omega)$ are:

(i) distortion of signals by the transducers and amplifiers,

(ii) distortion of sound waves by propagation through a turbulent shear flow,

(iii) spurious sound generated by the seeded flow.

4.1 The Effect of Transducers and Amplifiers

The computation of the cross-correlation functions and the cross-spectral densities is performed with electrical signals (voltages) that are near replicates of the physical quantities they represent. Ideally a transducer should convert a physical property of a medium into an electrical signal for all possible states of the particular property being measured. This requirement dictates that the transducer have a flat response over all frequencies, an infinite dynamic range, and be free of noise.

A practical compromise is to use transducers that have a smooth frequency response at least one decade beyond the lowest and highest frequencies of interest to the experimenter. The transducers must be operated well within their dynamic range, in order to minimize electrical noise and signal clipping. Similar considerations apply to amplifiers.

The action of a transducer is analogous to passing the signal to be measured through an electrical network. For a linear transducer, the electrical network is made up of passive components such as resistors, capacitors, and inductors; all amplifiers are assumed to be ideal. The output of such a transducer is given by:

$$g(t) = \int h(\alpha)\, f(t - \alpha)\, d\alpha \qquad (4.1)$$

where $f(t)$ is the physical quantity being measured, and $h(t)$ is the impulse response of the equivalent electrical network of the transducer (Ref. 62). For an ideal transducer $h(t) = A\,\delta(t)$.

The cross-correlation of the output signals of two dissimilar transducers measuring $f_1(t)$ and $f_2(t)$ respectively is:

$$\overline{g_1(t)\, g_2(t - \tau)} = \int \overline{h_1(\alpha)\, f_1(t - \alpha)\, h_2^*(\beta)\, f_2^*(t - \tau - \beta)}\, d\alpha\, d\beta$$

$$= \int h_1(\alpha)\, h_2^*(\beta)\, \overline{f_1(t)\, f_2^*(t - \tau - \beta + d)}\, d\alpha\, d\beta \qquad (4.2)$$

The correlation function of the process $\overline{f_1(t)\ f_2(t-\tau)}$ is distorted by the action of a double convolution. The degree of distortion depends on the nature of $h_1(t)$ and $h_2(t)$.

The cross-spectral density on the other hand takes the form:

$$\varphi_{g_1g_2}(\omega) = \int \overline{g_1(t)\ g_2(t-\tau)}\ e^{i\omega\tau}\ d\tau$$

$$= \int h_1(\alpha)h_2^*(\beta)\ \overline{f_1(t)\ f_2(t-\tau-\beta+\alpha)}\ e^{i\omega(\tau+\beta-\alpha)}\ e^{i\omega(\alpha-\beta)}\ d\tau d\alpha d\beta$$

$$= \mathcal{H}_1(\omega)\mathcal{H}_2^*(\omega)\ \varphi_{f_1f_2}(\omega) \qquad (4.3)$$

The cross-spectral density $\varphi_{f_1f_2}(\omega)$ of the process is modified by the product of two transfer functions which are the Fourier transforms of the respective transducer responses. A good transducer will be 'flat' over some bandwidth of B Hz, and the amplitude of the measured cross-spectrum, i.e. $|\varphi_{g_1g_2}(\omega)|$, will be a good estimate of $|\varphi_{f_1f_2}(\omega)|$ over the frequency range where $|\mathcal{H}_1(\omega)\mathcal{H}_2^*(\omega)|$ is nearly constant.

The effect of severely mismatched and slightly mismatched transducers is illustrated in Figs. 4.1 and 4.2. The case of severe transducer mismatch is modelled by a 'C' weighting network and a 1/3 octave filter centred at 1.6 KHz. The signals to be measured are generated by a common random noise source. The cross-correlation of the process has two interesting properties: the correlation function 'rings' at the filter centre frequency, and the envelope of the measured correlation peaks near .3 msec time delay; the cross-correlation that would be measured if the transducers were ideal is symmetric and has a maximum at zero time delay. Even a slightly mismatched transducer pair, as represented by 'C' and 'B' filters will cause some distortion of the correlation function (Fig. 4.2).

The cross-spectral density estimates can be interpreted much more readily, since the frequency response of the transducers simply multiply the cross-spectral density to be measured. It is more difficult to account for the effect of the double convolution. For this reason it is preferable to analyze data in the frequency domain. An added benefit is that n fold differentiation with respect to time is equivalent to multiplication by $(-i\omega)^n$ in the frequency domain.

When the signals to be analyzed are broadband in nature, the range of time delay for which the correlation is significantly greater than zero is of the order of 1/B, where B is the signal bandwidth. For small correlation coefficients the important details of the correlation functions will be buried in instrument noise, resulting in a poor estimate. The cross-spectral density function of the same process is not immune from noise, but the estimate of the cross-spectral density is much less sensitive to noise, since it extends over a wide range of B Hz.

4.2 The Effect of Sound-Flow Interaction

The sound generated by the turbulent flow must travel through turbulence as well as a mean velocity gradient before reaching still air. The mean velocity gradient refracts the sound away from the jet axis (Ref. 13). If the field position of the observer is more than 40° from the jet axis, then the effect of refraction is minimal. Scattering of sound by turbulent flow is always present. As a result of the interaction with turbulence, the sound wave emitted by a source in the jet flow will suffer a Doppler shift. The shift is random because of the randomness of the turbulence in space and time. The overall effect will be a spectral broadening. The analysis of the scattering problem is rather complex (Refs. 63, 64, 65), and it is more expedient to perform a controlled experiment that allows one to assess whether or not refraction and turbulent scattering are significant sources of error in the estimation of the cross-correlation and cross-spectral density functions.

The experimental arrangement of the test is similar to the one employed by Atvars et al (Ref. 13) in the study of refraction of sound by a jet flow (Fig. 4.3). An omnidirectional point source was placed in the jet flow field and driven by a pure tone signal. The sound received by a microphone in the far-field was then compared to the input signal. The relative amplitude and phase of the input and received signals were measured for several jet velocities (67, 94, 132 m/sec), source positions (y_1/D = 2, 6; r/R = 1) and microphone positions (-20° to 90°). The microphone signal was filtered by two narrow band frequency analyzers that were trimmed to zero phase error at the signal frequency. A PAR 129 lock-in amplifier served as a phase detector and RMS meter. The bandwidth of the detection system was measured to be .1 Hz.

The RMS output voltage of the lock-in amplifier is a measure of the peak amplitude of the correlation between the signal emitted by the point source and the sound received by the observer. The narrow bandwidth of the detection system effectively eliminates any uncorrelated noise signals. Changes in the RMS output can be caused by a combination of an altered directivity pattern (refraction) and spectral line broadening (turbulent scattering). It can be argued that the amount of turbulent scattering is governed by the ratio of the mean turbulence scale and the wavelength of the incident sound. The ratio is proportional to D/λ; D is the jet diameter. Values of D/λ at the three test frequencies (.069 at 1250 Hz; .139 at 2500 Hz; .278 at 5000 Hz) suggest that the high frequency sound will be subject to more intense turbulent scattering. Refraction will result in a redistribution of acoustic energy in space, but the frequencies will be preserved.

The propagation of sound through the turbulent shear flow may also be accompanied by a change in the travel time of the signal which is equivalent to a change in the relative phase of the signals. The phase measurements are very sensitive to small temperature fluctuations $T = T_{amb} + \Delta T$ and frequency drift $f = f_o + \Delta f$:

$$\frac{\Delta\phi}{\phi_o} \approx \left(\frac{\Delta f}{f_o} - \frac{1}{2} \frac{\Delta T}{T_{amb}} \right) \tag{4.4}$$

The reference test case (no flow) was repeated after each parameter change to minimize the error in the phase measurements. Frequency drift was held to .1 Hz/min by the use of a stable oscillator.

The measurements are relatively insensitive to changes in the position of the source (this was also found by Atvars et al). The change in arrival time is governed by the microphone position, jet speed, and source frequency (Fig. 4.4). At 40° to the jet axis, the change in arrival time is less than .02 msec. Such a shift in time delay cannot be detected if the basic delay increment of the correlator is .08 msec, as is the case when the cross-correlation functions $R_{u_x p}(\underset{\sim}{x},\underset{\sim}{y},\tau)$ and $R_{u_x 2p}(\underset{\sim}{x},\underset{\sim}{y},\tau)$ are being measured.

Amplitude changes are also functions of microphone position, jet velocity, and source frequency (Fig. 4.5). As expected from the early refraction experiments and the scaling outlined above, the low frequency components (1250 Hz) exhibit little, if any, measurable change in amplitude. Mid-frequencies (2500 Hz) appear to be refracted at small angles to the jet axis, with signal recovery at larger angles. The increase in the RMS level is small, as the refracted energy is spread over a much greater area. High frequencies (5000 Hz) suffer the largest amplitude changes. There is no complete recovery, even at 90° to the jet axis. Apparently the turbulent scattering has broadened the spectrum of the pure tone to such an extent that it contains significant energy outside the effective narrow band filter made up of the two ganged filters and the lock-in amplifier.

Even though the line broadening is significant for the high frequencies, it cannot be detected by the fast Fourier transform analyzer which is operated at a frequency spacing of 24 Hz, when cross-spectral densities or cross-correlations are computed. The effective frequency spacing of the PAR correlator is of similar magnitude. The results suggest that the sound propagation through the turbulent jet flow will not affect the estimates of the cross-correlations and cross-spectra for the frequency range of interest.

4.3 Jet Flow Field

A series of measurements was performed with the hot wire anemometer to determine the character of the jet flow, and to identify any possible discrepancies from typical jet flow behaviour. The parameters of interest are the mean flow distribution, the turbulent flow distribution, and the turbulence spectrum. Figure 4.6 illustrates the mean velocity profiles $U_1(y_1,r)/U_j$ and the turbulence intensity profiles $\sqrt{u_1^2}(y_1,r)/U_j$ as a function of distance y_1 from the jet nozzle. The potential core of the jet extends to four diameters downstream of the nozzle, and the mean velocity profiles in the transition region exhibit the typical Gaussian shape (Ref. 66).

In the mixing and transition regions the radial profiles of turbulence intensity peak near the $r/R = 1$ position. The high turbulence levels gradually diffuse from a narrow ridge centred about $r/R = 1$ and 'fill in' the region of low turbulence near the jet axis, as is shown by contours of equal turbulence intensity (Fig. 4.7).

A typical turbulence spectrum (Fig. 4.8) is flat to some critical frequency $\hat{f}(y_1,r)$ and then decays at a rate of about 6 dB/octave. No measurements were performed for axial positions greater than $y_1/D=7$. The jet flow was found to exhibit the characteristic features of a 'typical' jet (Ref. 67).

4.4 Jet Noise

Nossier and Ribner (Ref. 37) have devised a method which allows one to extract the self and shear noise spectra, as defined in the Ribner theory, directly from far field jet noise spectra. The procedure relies on the different directivity patterns and spectral contributions of the self and shear noise.

Consider the simplified self and shear noise model with mean square shear noise sound pressure proportional to:

$$\overline{p^2_{SH}}(\underset{\rightarrow}{x}) \alpha \frac{1}{|\underset{\rightarrow}{x}|} \int U_x(\underset{\rightarrow}{y}_1) U_x(\underset{\rightarrow}{y}_2) \frac{\partial^4}{\partial \tau^4} \overline{u_x(\underset{\rightarrow}{y}_1,t) u_x(\underset{\rightarrow}{y}_2,t-\tau)} \Bigg|_{\tau = c_o^{-1}(\underset{\rightarrow}{y}_2-\underset{\rightarrow}{y}_1)\cdot\underset{\rightarrow}{x}} \frac{d\underset{\rightarrow}{y}_1 d\underset{\rightarrow}{y}_2}{|\underset{\rightarrow}{x}|^{-1}} \quad (4.5)$$

The two point velocity correlation differs from zero only in a correlation volume L^3. The shear noise will scale as:

$$p^2_{SH}(\underset{\rightarrow}{x}) \alpha \frac{1}{|\underset{\rightarrow}{x}|} U_x^{\,2}\, u_x^{\,2}\, f_{SH}^4\, L^3\, V_{JET} \quad (4.6)$$

where f_{SH} is a characteristic shear noise frequency. U_x^2 may be approximated as $U_1^2 \cos^2\theta$.

Similarly the mean square self noise

$$\overline{p^2_{SF}}(\underset{\rightarrow}{x}) \alpha \frac{1}{|\underset{\rightarrow}{x}|} \int \frac{\partial^4}{\partial \tau^4} u_x^{\,2}(\underset{\rightarrow}{y}_1,t) u_x^{\,2}(\underset{\rightarrow}{y}_2,t-\tau) \Bigg|_{(\underset{\rightarrow}{y}_2-\underset{\rightarrow}{y}_1)\cdot\underset{\rightarrow}{x}\, c_o^{-1} |\underset{\rightarrow}{x}|^{-1}} \quad (4.7)$$

scales as

$$p^2_{SF}(\underset{\rightarrow}{x}) \alpha \frac{1}{|\underset{\rightarrow}{x}|} (u_x^{\,2})^2\, f_{SF}^4\, L^3\, V_{JET} \quad (4.8)$$

A spectral component $e^{i\omega t}$ of the shear noise will upon squaring become $e^{2i\omega t}$. Hence as a first approximation: $f_{SF} = 2f_{SH}$; for a random process the frequency shift depends on the statistics of the process and may not be equal to 2.

The shear noise, therefore, is expected to exhibit a dipole-like ($\cos^2\theta$) directivity and dominant frequency f_{SH}, and the self noise should be omnidirectional with dominant frequency $2f_{SH}$. At 90° to the jet axis, there is no shear noise contribution, allowing one to estimate the self noise.

A more rigorous analysis due to Ribner (Ref. 10) is based on a two point correlation model with postulated statistics and accounts for source motion. The central results of his analysis are:

$$\varphi_{p_\theta}(CS) = \left\{ \varphi_{SELF}(CS) + \varphi_{SHEAR}(CS) \frac{\cos^2\theta(1 + \cos^2\theta)}{2} \right\} C^{-4} \qquad (4.9)$$

C = convection factor $[(1 - M_c\cos\ )^2 + \alpha^2 M_c{}^2]^{1/2}$

S = Strouhal number fD/U_{JET}

φ = power spectral density

The overall jet noise spectrum measured at an angle θ to the jet axis (outside the zone of refraction) is the sum of a self and shear noise spectrum. The effect of convection is a downstream bias (C^{-4}) and a Doppler shift (CS). Furthermore, the model predicts that the self and shear noise spectra are similar but with the self noise shifted by one octave

$$\varphi_{SHEAR}(CS) = \beta\, \varphi_{SELF}(2CS) \qquad (4.10)$$

The amplitude factor β is predicted to be 2.

If the self and shear noise theory is not a valid description of the jet noise, then any attempt to cast the jet noise spectra into the form of Eq. 4.9 would result in a non-unique shear noise spectrum. Nossier and Ribner (Ref. 37) have tested the self and shear noise model against experimental jet noise data and have found that the shear noise spectrum is unique and conforms to the notion of Eq. 4.10, namely that the self and shear noise spectra match and exhibit nearly an octave shift. These results support the major predictions of the theory and lend credibility to the existence of shear noise.

The basic self noise spectrum can be estimated from jet noise measurements at 90° to the jet axis. At angles other than 90°, the self noise is changed by convection $[C^{-4}\varphi(CS)]$ in a predictable manner. Thus the shear noise spectrum can be extracted by an algorithm formulated by Nossier and Ribner (Ref. 37):

$$\varphi_{SELF}(CS) = C_{90°}^4\, \varphi_{p_{90°}}(CS)$$

$$\varphi_{SHEAR}(CS) = \frac{2}{\cos^2\theta(1 + \cos^2\theta)} \left\{ C_\theta^4\, \varphi_{p_\theta}(CS) - C_{90°}^4\, \varphi_{p_{90°}}(CS) \right\} \qquad (4.11)$$

Figure 4.9 shows plots of $\varphi_{p\theta°}$ for three different far-field microphone positions at a constant jet velocity of 105 m/sec. The spectral peak moves toward the lower frequencies for decreasing angles with the jet axis (reverse Doppler shift). The measurement at $\theta = 90°$ contains some error, as the microphone was just 15 cm away from the nearest fibreglass wedge, bringing about some low frequency enhancement. The over-estimation of the low frequency components of the self noise leads to a reduced shear noise estimate.

The self and shear noise spectra, calculated on the basis of Eq. 4.11, are plotted in Fig. 4.10. The ratio of the peak spectral amplitudes of the self and shear noise is 1.71, and the ratio of the peak frequencies is 1.36. Nossier and Ribner (Ref. 37) have found that a large body of jet noise data exhibits a one octave shift between the self and shear noise spectral peaks. A 7% increase in the peak amplitude of the shear noise, for example, would shift the spectral peaks sufficiently far apart, and the peak frequency ratio would be closer to 2. Even without these hypothetical corrections, the estimates compare with spectra computed by Nossier (Ref. 68), from published jet noise spectra of a 1.52" diameter jet at jet velocity of 122 m/sec (Fig. 4.11). The self and shear noise spectra extracted from far-field measurements serve as reference data for the self and shear noise estimates to be computed from the cross-spectral densities $\Phi_{u_x p}(\underline{x},\underline{y},\omega)$ and $\Phi_{u_x 2p}(\underline{x},\underline{y},\omega)$.

4.5 Laser Doppler Velocimeter Performance Checks

The operating characteristics of the Laser Doppler Velocimeter (LDV) are described below. The overall performance of the LDV is good, and an accurate description of the fluid motion can be obtained, subject to the limitations inherent in the measuring technique.

4.5.1 Beam Intersection

After the initial alignment of the optics was completed, the beam intersection was double-checked. It is difficult to detect small alignment errors, as the beam diameter is about 1 mm. When a test objective is placed at the beam intersection, it is possible to view a magnified image of the probe volume on an opaque screen (Fig. 4.12). The position of the intersecting beams is adjusted until the cross-section of the fringe pattern becomes circular. Under these conditions the test section is an ellipse of revolution with major axis 10 mm and minor axis 1 mm. Compared to the sensing elements of the hot film probes used to survey the jet flow (Sec. 4.3), the measuring volume has increased by a factor of 300. The upper velocity limit of the LDV system in the present configuration is 150 m/sec, well above the jet exit velocity of 105 m/sec.

4.5.2 Measurement of Jet Velocity

The LDV probe volume was located at $y_1/D = 2$ inside the potential core of the jet, and the output voltage of the processor was measured as a function of the orientation of the probe volume with respect to the jet axis. The normalized velocity $U(\theta)/U(0)$ is described by the function $\cos\theta$. There is good agreement between the measurements and the hypothesis (Fig. 4.13). For angles greater than 60° data validation is affected by the small number of particles that cross at least eight fringes in the probe volume. Eventually an orientation is reached (dead angle) for which no particle crosses eight fringes, preventing the processor from computing a velocity estimate.

The spatial resolution of the LDV is determined by the extent of the probe volume. If there is a significant change in the mean flow velocity in the span of the probe volume, then the DC output voltage will be the average mean velocity in the probe volume. [The determination of the mean velocity in the presence of a shear flow across the probe volume is controversial (Refs. 69, 70); however, if the shear is small, then there cannot be a large error no matter which method of mean flow estimation is used.]

A more serious problem is the creation of a spurious turbulent velocity component. This phenomenon, caused by the sampling of single particle velocities, is not found in hot wire anemometers, where the heat transfer rate is automatically averaged by the sensor. In a turbulent shear flow the experimenter cannot identify whether the fluctuating signal is caused by an apparent turbulent velocity or a real one. The ambiguity is of no significance in cross-correlation experiments, as the two velocities are real physical quantities. Any small shift of the measuring point within the probe volume cannot be detected.

The presence of an apparent turbulent velocity due to mean shear will increase the turbulence intensities and broaden the region of peak turbulence intensity that is found near r/R = 1 (Fig. 4.14). The LDV based mean velocity profiles agree with the profiles measured with the hot wire anemometer (Fig. 4.15). The difference in the turbulence intensity profile can be explained by the presence of mean shear.

4.5.3 Effect of the LDV Processor on the Turbulent Velocity Spectrum

The DISA 55L90 processor computes the speed of a single particle and stores the value in the output memory, until a new valid speed has been measured. The output of the processor resembles a staircase with random step height and step length (Fig. 4.16). The sampling theorem (Ref. 71) states that no information is lost if the digitization rate (here the data rate) is at least two times the highest frequency of interest. The upper frequency limit was chosen to be 10 KHz, in order to allow for data rate fluctuations near the boundary of the jet flow. The peak frequency radiated by the jet is about 2 KHz, at least 2 octaves below the upper frequency limit. The average data rate observed during the cross-correlation/cross-spectral density measurements was greater than 20 KHz, the Nyquist frequency for a 10 KHz spectral analysis range. When the data rate is artificially decreased (by attenuation of the output of the photomultiplier), the high frequency estimate of the turbulence spectrum is reduced (Fig. 4.17). For the case of high data rates (in excess of 20 KHz), the power spectral estimates compare with the ones computed from hot wire anemometer measurements (Fig. 4.18). The effect of the data rate on a single frequency component is analyzed in Appendix E.

The previous tests support the assertion of Cliff et al (Ref. 72), namely that LDV and hot wire anemometer measurements are compatible.

4.5.4 Mass Addition Due to Seeding of the Flow

In order to assure data rates that are consistently greater than 20 KHz, water droplets must be added to the jet flow at a rate of .64 gm/sec. The mass of the seeding particles increases the fluid density. As the droplets have virtually no kinetic energy when they are injected into the plenum, the jet velocity must decrease. The droplets may also affect the turbulence structure and can attenuate high frequency sound (Ref. 73). Based on the increase in mass, one predicts a 6% change in flow velocity and a 2 dB change in the radiated sound pressure level; the latter is confirmed by measurement. The power spectral density of the jet noise should exhibit a 6% shift toward the low frequencies (as a result of Strouhal scaling fD/U_j), and a decrease in spectrum level, which should be uniform, if the absorption due to water vapour and droplets is negligible.

There is a very slight excess loss for frequencies greater than 6.3 KHz (Fig. 4.19). There may still be local changes in the turbulence structure of the jet flow. Any significant change in the turbulence should alter the near field pressure signature and the near-field far-field pressure cross-correlations. There is no measurable change in the normalized cross-correlation coefficients for the seeded and unseeded jet flow (Fig. 4.20). The only effect of any consequence is the velocity defect that is caused by the mass addition.

5. EXPERIMENTAL PROCEDURE

5.1 Field Points

Even though the contributions to the jet noise from a unit volume of jet may change with position in the jet, the source pattern retains a top-bottom symmetry. This property allows one to survey only field points that are located in the upper two quadrants of a slice of jet, without losing any information about the remainder of the slice. The field points were located on semicircles of radius R centred at $y_1/D = n$, $n = (3, 7)$. The jet nozzle interfered with the Laser Doppler Velocimeter optics for $n < 3$. The coordinates of the field points were chosen to be $(y_1/D, r/R, \phi) = (n, 1, m\pi/4)$; $m = (0, 4)$. A more comprehensive survey was performed at $y_1/D = 3$ and 6, permitting a better estimate of the contribution to the far field pressure from a typical slice of jet in the mixing and transition regions of the jet (Fig. 5.1).

The sound pressure was measured at a single position 160 cm from the jet nozzle and at an angle of 40° to the jet axis. The location offers the best compromise between the detectability of the shear noise contribution $(\cos^2\theta + \cos^4\theta)$ and errors due to refraction of sound by the jet flow.

5.2 Signal Handling

The signal processing schematic shown in Fig. 5.2 traces the paths of the output voltages of the LDV and microphone systems. The output of the Laser Doppler processor is split into three components. The DC voltage $V_{U_x} \sim (U_x)$ is measured by a calibrated digital multimeter. The turbulence signal, available at the output of an AC coupled amplifier with a voltage gain of 8, or a voltage proportional to the square of the instantaneous turbulent velocity, reaches the input of the fast Fourier transform (FFT) analyzer via a unity gain wide band filter (20 Hz to 40 KHz). The microphone signal is passed through a similar wide band filter, but with a voltage gain of 100. The cross-correlations and the cross-spectral densities are computed by the DSP 360 FFT analyzer. The input voltages to the analyzer are measured by two RMS voltmeters. The velocity and sound signals are passed through nearly identical networks, thereby minimizing any spectral distortion due to mismatched frequency response. The voltages that represent the various physical quantities to be analyzed are defined by:

$$
\begin{aligned}
V_{U_x} &= k_u\, U_x(\underrightarrow{y}) & V_p &= 8000 k_p\, p(\underrightarrow{x},t) \\
V_{u_x} &= 8k_u\, u_x(\underrightarrow{y},t) & k_u &= .040\ \text{V/m/sec} \qquad (5.1) \\
V_{u_x^2} &= \frac{64}{10V}\, k_u^{\,2}\, u_x^{\,2}(\underrightarrow{y},t) & k_p &= .0125\ \text{V/N/m}^2
\end{aligned}
$$

5.3 Correlation Measurements

The majority of the cross-correlation functions were computed over the delay range -12.5 to 12.5 msec. It was possible to identify the major maxima of the cross-correlations, when several realizations (typically 5) were plotted on a common hard copy output. The temporal resolution of the cross-correlation functions could be improved by the use of a shorter delay range and suitable precomputation delay. It was found, however, that the decrease in averaging time brought about unacceptably large noise signals that add to the low amplitude cross-correlations. The PAR 101 correlator which possesses an integration time independent of the delay range could not improve the poor resolution.

5.4 Cross-Spectral Density Measurements

The cross-spectral density estimates were affected by similar signal to noise problems. The errors were minimized by displaying the computed spectra in an amplitude phase $[\log|\varphi_{(\omega)}|;\ \phi^\circ,\ \phi = \tan^{-1}(I_m\varphi/Re\varphi)]$ format. The logarithm 'compressed' the noise that added to the signal and allowed a reasonable estimate of the amplitude of the cross-spectral density. In addition, the logarithmic format enhanced the dynamic range of the output memory of the FFT analyzer which is limited to 12 bit words.

The analysis below shows that the phase information is not needed in the estimate of the far field power spectrum, if the two point cross-correlations that are proportional to the source strengths are symmetric. Consider the auto-correlation of the far-field shear noise:

$$R_{\substack{pp\\SHEAR}}(\underset{\rightarrow}{x},\tau) \sim \int_V \frac{\partial^2}{\partial\tau^2}\,\overline{u_x(\underset{\rightarrow}{y},t)\ p(\underset{\rightarrow}{x},t - \tau + c_o^{-1}|\underset{\rightarrow}{x} - \underset{\rightarrow}{y}|)}\ dy \qquad (5.2)$$

The power spectrum is the Fourier transform of the auto-correlation:

$$\varphi_{\substack{pp\\SHEAR}}(\underset{\rightarrow}{x},\omega) \sim \iint \frac{\partial^2}{\partial\tau^2} R_{u_x p}(\underset{\rightarrow}{y},\underset{\rightarrow}{x},\tau - c_o^{-1}|\underset{\rightarrow}{x} - \underset{\rightarrow}{y}|)\ e^{i\omega\tau}\ d\underset{\rightarrow}{y}\ d\tau$$

$$= -\int \omega^2\ \varphi_{u_x p}(\underset{\rightarrow}{x},\underset{\rightarrow}{y},\omega)\ e^{i\omega c_o^{-1}|\underset{\rightarrow}{x}-\underset{\rightarrow}{y}|}\ d\underset{\rightarrow}{y} \qquad (5.3)$$

where $\varphi_{u_x p}(\underset{\rightarrow}{x},\underset{\rightarrow}{y},\omega)$ is defined by

$$\varphi_{u_x p}(\underset{\rightarrow}{x},\underset{\rightarrow}{y},\omega) = \int \overline{u_x(\underset{\rightarrow}{y},t)\ p(\underset{\rightarrow}{x},t - \tau)}\ e^{i\omega\tau}\ d\tau \qquad (5.4)$$

but $\overline{u_x(\underset{\rightarrow}{y},t)\ \ p(\underset{\rightarrow}{x},t - \tau)}$ has a maximum at $\tau = -c_o^{-1}|\underset{\rightarrow}{x} - \underset{\rightarrow}{y}|$. The function

$$f(\underset{\rightarrow}{x},\underset{\rightarrow}{y},\tau + c_o^{-1}|\underset{\rightarrow}{x} - \underset{\rightarrow}{y}|) = \overline{u_x(\underset{\rightarrow}{y},t)\ p(\underset{\rightarrow}{x},t-\tau)} \tag{5.5}$$

is assumed to be symmetric about $\tau = -c_o^{-1}|\underset{\rightarrow}{x} - \underset{\rightarrow}{y}|$, and

$$\varphi_{u_x p}(\underset{\rightarrow}{y},\underset{\rightarrow}{x},\omega) = \frac{1}{2\pi}\int f(\underset{\rightarrow}{x},\underset{\rightarrow}{y},\tau + c_o^{-1}|\underset{\rightarrow}{x} - \underset{\rightarrow}{y}|)\ e^{i\omega\tau}\ d\tau \tag{5.6}$$

$$\varphi_{u_x p}(\underset{\rightarrow}{x},\underset{\rightarrow}{y},\omega) = \frac{1}{2\pi}\int f(\underset{\rightarrow}{x},\underset{\rightarrow}{y},T)\ e^{i\omega T}\ dT\ e^{-i\omega c_o^{-1}|\underset{\rightarrow}{x}-\underset{\rightarrow}{y}|} \tag{5.7}$$

$$= \mathcal{F}(\underset{\rightarrow}{x},\underset{\rightarrow}{y},\omega)\ e^{-i\omega c_o^{-1}|\underset{\rightarrow}{x}-\underset{\rightarrow}{y}|} \tag{5.8}$$

$\mathcal{F}(\underset{\rightarrow}{x},\underset{\rightarrow}{y},\omega)$ is wholly real, since $f(\underset{\rightarrow}{x},\underset{\rightarrow}{y},T)$ is symmetric about $T = 0$. Thus:

$$\varphi_{\substack{pp \\ SHEAR}}(\underset{\rightarrow}{x},\omega) \sim \int -\omega^2 \left\{\mathcal{F}(\underset{\rightarrow}{x},\underset{\rightarrow}{y},\omega)\ e^{-i\omega c_o^{-1}|\underset{\rightarrow}{x}-\underset{\rightarrow}{y}|}\right\} e^{i\omega c_o^{-1}|\underset{\rightarrow}{x}-\underset{\rightarrow}{y}|}\ d\underset{\rightarrow}{y}$$

$$= -\int \omega^2\, \mathcal{F}(\underset{\rightarrow}{x},\underset{\rightarrow}{y},\omega)\ d\underset{\rightarrow}{y} \tag{5.9}$$

The FFT analyzer measures an approximation to $\mathcal{F}(\underset{\rightarrow}{x},\underset{\rightarrow}{y},\omega)e^{i\phi}$, where, theoretically, $\phi = -\omega c_o^{-1}|\underset{\rightarrow}{x} - \underset{\rightarrow}{y}|$. The output format thus allows implementation of Eq. 5.9. A similar analysis may be performed for the case of the self noise.

The measured cross-spectral densities were processed by tracing a smooth best fit curve on a translucent paper, placed over the hard copy drawn by the X-Y plotter. After applying the f^2 correction to convert $[\varphi_{u_x p}(\underset{\rightarrow}{x},\underset{\rightarrow}{y},\omega),\ \varphi_{u_x 2p}(\underset{\rightarrow}{x},\underset{\rightarrow}{y},\omega)]$ to $[\varphi_{u_x p}(\underset{\rightarrow}{x},\underset{\rightarrow}{y},\omega),\ \varphi_{u_x 2p}(\underset{\rightarrow}{x},\underset{\rightarrow}{y},\omega)]$, the cross-spectral densities were multiplied by $2V_{U_x}$ and $1.25V$ respectively and plotted in a double logarithmic format. The amplitude scale is referenced to an arbitrary level, common to all spectral measurements.

The volume integral that sums the contribution of all field points to the power spectral density of the far-field pressure (Eq. 2.19) can be rearranged to be more compatible with the measured data:

$$\varphi_{pp}(\underset{\rightarrow}{x},f) = (8000\ k_p)^{-2}\ \varphi_{V_p V_p}(\underset{\rightarrow}{x},f) \tag{5.10}$$

and

$$\varphi_{V_p V_p}(\underset{\rightarrow}{x},f) = \frac{\rho_o}{4\pi c_o^2 |\underset{\rightarrow}{x}|}\ \frac{\omega_o^2 D\hat{A}}{8k_u^2}\ (8000\ k_p)$$

$$\cdot \int \frac{dy_1}{D}\left\{\int_{A(y_1/D)} \frac{\omega^2}{\omega_o^2}\left[\ 2V_{U_x}\left|\varphi_{V_{u_x}V_p}\right| + 1.25\left|\varphi_{V_{u_x}2V_p}\right|\ \right]\frac{dA}{\hat{A}}\right\} \tag{5.11}$$

where $A(y_1/D)$ is the area of a slice of jet of thickness d y_1/D and $\hat{A}$ is the area of the jet at $y_1/D = 3$. If the cross-spectral densities are of the form

$$\varphi(\underset{\rightarrow}{x},\underset{\rightarrow}{y},f) = \varphi(\underset{\rightarrow}{x},y_1,f)\ d(y_2,y_3) \tag{5.12}$$

then

$$\varphi_{V_pV_p} = K\int \frac{f^2}{f_o^2}\ |\varphi_{V_{u_x}V_p}(x,y,f)|\int_A 2V_{U_x}(y)d_1(y)\ \frac{dA}{A}\ d\ \frac{y_1}{D}$$

$$+ K\int \frac{f^2}{f_o^2}\ |\varphi_{V_{u_x}{}^2V_p}(\underset{\rightarrow}{x},\underset{\rightarrow}{\hat{y}},f)|\int_A 1.25V\ d_2(\underset{\rightarrow}{y})\ \frac{dA}{\hat{A}}\ d\ \frac{y_1}{D} \tag{5.13}$$

where $\hat{y}$ is chosen to be $(y_1/D,\ r/R = 1,\ \phi = 0)$. The integrals over $A(y_1/D)$ compute the contribution of a thin slice of jet to the total power spectral densities. In particular:

$$D_1\left(\frac{y_1}{D}\right) = \int_{A(y_1/D)} 2V_{u_x}(\underset{\rightarrow}{y})\ d_1(\underset{\rightarrow}{y})\ \frac{dA}{\hat{A}}$$

$$D_2\left(\frac{y_1}{D}\right) = \int_{A(y_1/D)} 1.25V\ d_2(\underset{\rightarrow}{y})\ \frac{dA}{\hat{A}} \tag{5.14}$$

were estimated from detailed measurements at $y_1/D = 3$ and 6. Values of D_1 and D_2 at other stations were obtained by interpolation or extrapolation. The y_1 integration along the jet axis is replaced by a summation with step size $\Delta y_1/D = 1$; thus:

$$\varphi_{V_pV_p}(x,f) \approx \frac{\pi\rho_o f_o^{\,2}}{c_o^{\,2}|x|}\ \frac{8000\ k_p\hat{A}}{8\ k_u^{\,2}}$$

$$\cdot\sum_{n=3}^{7}\left\{\frac{f^2}{f_o^2}\ |\varphi_{V_{u_x}V_p}(\underset{\rightarrow}{x},\underset{\rightarrow}{\hat{y}}_n\ f)|\ D_1(n) + \frac{f^2}{f_o^2}\ |\varphi_{V_{u_x}{}^2V_p}(\underset{\rightarrow}{x},\underset{\rightarrow}{\hat{y}}_n\ f)|\ D_2(n)\right\} \tag{5.15}$$

The above formalism is compatible with Eq. 2.21 and was used to sum the contribution of the field points in the jet to the power spectral density of V_p, which is directly proportional to $\varphi_{p,p}(\underset{\rightarrow}{x},\omega)$.

The strongest aliases in the spectra of u_x and $u_x{}^2$ are expected to be in the range of 10 KHz and beyond (based on a 20 KHz data rate, see Appendix E); therefore, the analysis range was chosen to span 0 to 10 KHz.

6. RESULTS AND DISCUSSION

6.1 Cross-Correlations

The cross-correlations $\overline{u_x(\underset{\rightarrow}{y},t)\ p(\underset{\rightarrow}{x},t-\tau)}$ and $\overline{u_x^2(\underset{\rightarrow}{y},t)\ p(\underset{\rightarrow}{x},t-\tau)}$ are expected to peak near $c_o^{-1}|\underset{\rightarrow}{x}-\underset{\rightarrow}{y}|$ and decay rapidly with increasing τ (Appendix A). Measured correlations are largely obscured by noise, and only the peak values can be determined with any degree of accuracy. The measurements are repeatable, as is shown by Figs. 6.1 and 6.2. Each plot is a superposition of 40 realizations of the 'shear' and 'self' noise correlations respectively. The increase of the noise at the extreme values of time delay is an artifact of the built-in amplitude correction of the DSP 360 analyzer.

The self noise correlations $R_{u_x^2p}(\underset{\rightarrow}{x},\underset{\rightarrow}{y},\tau)$ are similar in their temporal behaviour over a cross-section of jet, and vary only in magnitude as the field point location is changed. The shear noise correlations $R_{u_xp}(\underset{\rightarrow}{x},\underset{\rightarrow}{y},\tau)$ possess a marked dependence on the position of the source point (Fig. 6.3); the behaviour illustrated in Fig. 6.3 is typical for all field points. Cross-correlations measured with the PAR 101 correlation function computer, which evaluates the cross-correlation directly, exhibited the same features.

The self noise correlations peak at the expected time delay of $c_o^{-1}|\underset{\rightarrow}{x}-\underset{\rightarrow}{y}|$, whereas the shear noise correlations have peak amplitudes at about .2 msec earlier (Fig. 6.4). The shear noise signal is apparently emitted by the correlation volume prior to the velocity measurement at the source point. Even though the shear noise correlation is influenced by the behaviour of the mean flow distribution (Appendix A), no model has been found that can account satisfactorily for the observed phenomena.

Shear noise correlations measured with a hot wire anemometer (Fig. 6.5) do not behave in a similar manner in that they do peak at the expected time delay of $c_o^{-1}|\underset{\rightarrow}{x}-\underset{\rightarrow}{y}|$. This result is compatible with the notion of probe-flow interaction which appears to dominate the genuine flow noise generated by the correlation volume that surrounds the probe (Appendix B).

The self and shear noise correlations are strongest along the line $r/R = 1$, $\phi = 0$. The peak cross-correlation coefficients

$$\frac{R_{u_xp}(\underset{\rightarrow}{x},\underset{\rightarrow}{y},\tau)}{\sqrt{u_x^2(\underset{\rightarrow}{y})\ p^2(\underset{\rightarrow}{x})}}\ ;\qquad \frac{R_{u_x^2p}(\underset{\rightarrow}{x},\underset{\rightarrow}{y},\tau)}{\sqrt{(u_x^2)^2(\underset{\rightarrow}{y})\ p^2(\underset{\rightarrow}{x})}} \tag{6.1}$$

are the order of .004 (Fig. 6.6). The poor resolution of the cross-correlation functions prevented any further data processing.

6.2 Contribution to the Jet Noise from a Unit Volume of Jet

A set of measured cross-spectral densities $\Phi_{V_{u_x}V_p}(\underset{\rightarrow}{x},\underset{\rightarrow}{y},f)$ and $\Phi_{V_{u_x^2}V_p}(\underset{\rightarrow}{x},\underset{\rightarrow}{y},f)$ is shown in Figs. 6.7 and 6.8. The lower trace of each plot is the amplitude of the cross-spectral density displayed in a $\log|\varphi|$ format. The upper trace represents the phase angle in degrees (-180° to 180°).

Even though both the amplitude and the phase of the measured spectra suffer from similar sources of error (mainly due to finite averaging times), one can estimate the smooth amplitude of the cross-spectral density with some confidence. Repeated measurements show that the error signals are random. The linear display of the phase angle is very sensitive to error signals when the phase angle of the cross-spectral density is near ± 180°, and small perturbations cause a large amount of jitter.

Data processing, as described in Section 5.4, converts the cross-spectral densities to contributions to the self and shear noise spectra from a unit volume of jet as shown in Figs. 6.9 and 6.10 respectively. The spectral contributions and their peak frequencies are decreasing functions of the distance from the jet nozzle. Contrary to speculation, a unit volume radiates a broad-band signal; the peak frequency can be considered as the preferred frequency. In the range $y_1/D = 3$ to 7, the peak frequencies are approximated by the empirical relations:

$$f_{SELF} = \left(5.3 - .44 \frac{y_1}{D} \right) \text{KHz}$$

$$f_{SHEAR} = \left(3.0 - .20 \frac{y_1}{D} \right) \text{KHz} \qquad (6.2)$$

The average peak frequency ratio f_{SELF}/f_{SHEAR} is 1.54. The cross-spectral density measurements indicate that the self and shear noise contribution from a unit volume of jet to the far field jet noise at 40° to the jet axis are approximately equal.

6.3 Contribution to the Jet Noise from a Slice of Jet

In what follows, the terms source distributions and source patterns are to be interpreted as source power densities and not as source strength densities as used earlier, e g. on RHS of Eqs 2.4, 2 5, etc. The respective self and shear noise source strength densities are proportional to $(\partial^2 u_x/\partial t^2)$ and $U_x(\partial^2 u_x/\partial t^2)$. On the other hand contributions from a unit volume to the far-field acoustic power take the forms $(\partial^4 u_x^2 u_x'^2/\partial\tau^4)$ and $(\partial^4 u_x U_x u_x' U_x'/\partial\tau^4)$ which scale as $\omega^4 \overline{(u_x^2)^2}$ and $\omega^4 \overline{u_x^2} U_x^2$, respectively.

The contribution from slices of jet at $y_1/D = 3$ and 6 have been computed from detailed measurements at a grid of field points. At a given axial station, the spectra are similar in their frequency content and differ only in amplitude (Fig. 6.11). After cross-plotting the data, contours of constant source contributions can be obtained. The reference position in each slice of jet is located at $r/R = 1$, $\phi = 0°$.

At $y_1/D = 3$ the potential core (which should contain no sources) is clearly defined. The source distributions of the shear and self noise (Figs. 6.12, 6.13) are largely confined to the quadrants of jet closest to the observer and are strongest along the circle $r/R = 1$. The source patterns in the Proudman format are fixed to the vector $\underset{\sim}{x}$ and move with the observer; therefore the jet axisymmetry will insure that the mean square pressure is axisymmetric. Because of the top-bottom symmetry only the upper portion of the patterns are illustrated.

There is a close affinity of the source patterns to the functions $\overline{u_x^2}U_x^2$ and $(\overline{u_x^2})^2$. From a simplistic argument these may be considered to be approximate indicators of the contributions* per unit volume to the far field shear and self noise power. $\overline{u_x^2}U_x^2$ and $(\overline{u_x^2})^2$ are not axisymmetric, contrary to the common assumption in noise models. The turbulence is not isotropic and the mean flow not quite parallel to the jet axis; thus there will be a biasing toward the observer at x. The role of the radial flow is indicated in Fig. 6.15. The nominal source patterns do not behave exactly as the two point velocity correlations that govern the sound generation, and therefore are not one to one with the measured source patterns.

In the transition region the properties of the jet flow approach the characteristic behaviour of a fully developed turbulent jet. The source distributions are expected to become more symmetric about the jet centre line. At $y_1/D = 6$ both the self and shear noise source patterns are strongest in the quadrants closest to the observer, with a pronounced bulge along the line pointing in the direction of the observer (Figs. 6.16, 6.17). The mean velocity distribution U_x gives the shear noise pattern a more circular appearance. As was the case on the mixing region, the nominal source patterns $\overline{u_x^2}U_x^2$ and $(\overline{u_x^2})^2$ are similar to the source distributions of the shear and self noise respectively (Fig. 6.18).

6.4 Jet Noise Contribution from Field Points in the Region $3 \leqslant y_1/D \leqslant 7$

The overall self and shear noise spectra at 40° to the jet axis can be constructed from contributions of radial slices of jet (see Section 5.4). Figure 6.19 illustrates the spectral contributions from such slices in the range $y_1/D = 3$ to 7. As the cross-spectra were found to differ only in their relative amplitudes at a fixed axial position the curves are similar to the ones in Fig. 6.9 and 6.10 but with different magnitudes to account for the overall emission from a slice of jet rather than a unit volume.

The total self and shear noise contributions from an individual slice, which is directly proportional to the area under the corresponding curves in Fig. 6.19, are nearly equal. The contributions to the far field jet noise are decreasing functions of axial position in the range $3 \leqslant y_1/D \leqslant 7$ (Fig. 6.20). The hybrid model discussed in Appendix A is shown for comparison. The model source strength distributions are based on assumed frequency and correlation volume scaling and measured nominal source patterns and agree qualitatively with the normalized self and shear noise source strength distributions deduced from the cross-spectral density measurements in the region surveyed by the experiment, namely $y_1/D = 3$ to 7. This particular region appears to be responsible for about 40% of the total jet noise heard by an observer at 40° to the jet axis.

---

* For the model discussed in Appendix A the respective self and shear noise contributions to the power spectrum of the far field jet noise are of the form (Eqs. A21 and A28):

$$d\varphi_{SF} \approx (\overline{u_x^2})^2\, \omega^4\, \mathcal{J}_1(\omega, \underset{\sim}{y}) \sim \overline{(u_x^2)^2}\, \omega^4\, \mathcal{J}_1(\omega, \underset{\sim}{y})$$

$$d\varphi_{SH} \approx \overline{u_x^2}\, U_x^2\, \omega^4\, \mathcal{J}_2(\omega, \underset{\sim}{y})$$

If $\mathcal{J}_1$ and $\mathcal{J}_2$ are invariant across a slice of jet, then the contributions to the self/shear noise spectra are governed by the nominal source patterns $(\overline{u_x^2})^2$ and $\overline{u_x^2}\, U_x^2$ respectively.

The behaviour of several frequency bands (bandwidth 24 Hz) suggests that the major part of the source distribution is confined to axial positions less than $y_1/D = 10$ (Fig. 6.21). Source location techniques such as employed by Grosche et al (Ref. 74) and Fischer et al (Ref. 75) indicate that sources as far downstream as 15 jet diameters contribute to the jet noise. These tests were, however, performed at considerably higher Mach number than the present experiments (Grosche: M = 0.7 and 1.0; Fischer: M = 0.8). Grosche's results show that the source distribution migrates towards the jet nozzle as the Mach number is reduced.

The source strength distributions of Fisher et al (Ref. 75) exhibit a rather steep roll-off in the transition region of the jet. The rapid loss of source strength is moderated by a slow asymptotic decay for $y_1/D > 8$; thus the axial source strength distributions deduced from the measured cross-spectral densities may well be compatible with the ones that would be measured by an acoustic source location technique. Acoustic telescope measurements of Billingsley and Kinns (Ref. 76) appear to corroborate the present results. Their tests were performed on a real (i.e. hot) turbojet exhaust, and the correspondence is thought to be rather fortuitous.

The spectral contributions to the overall self and shear noise are estimated by direct summation over all slices of jet that have been surveyed. As was inferred above, only about 40% of the overall jet noise appears to be accounted for; hence, the spectra predicted from the measured cross-spectral densities are likely to underestimate the self and shear noise spectra which have been extracted from the far-field jet noise via the Nossier-Ribner technique (see Section 4.4). Based on the behaviour of the sources contained in the region $y_1/D = 3$ to 7, it can be argued that sources downstream of the axial position $y_1/D = 7$ will contribute much of their energy to the low frequency parts of the spectra, and the sources near the jet nozzle ($y_1/D < 3$) will add to the high frequencies.

The self and shear noise contributions to the overall jet noise (in the present investigation only the observer position at 40° to the jet axis is considered) can be estimated from far field jet noise data via the Nossier-Ribner algorithm (Ref. 37) or from cross-spectral densities as measured herein. Both methods are consistent with Ribner's self and shear noise model and, if the theory is valid, should result in identical predictions of the self and shear noise spectra subject to experimental constraints. Should such a closure be demonstrated, then the credibility of the theory, which is supported by other evidence (for example: compatibility with the work of Mani, Ref. 23, as demonstrated by Ribner, Ref. 24, theoretical two point far field pressure correlations, Ref. 28) is strengthened.

The shear noise spectrum computed from measured spectral densities and the shear noise spectrum extracted from the far field jet noise are compared in Fig. 6.22. The shear noise contribution from the limited volume surveyed by the experiment is comparable to the total radiated shear noise. There has been no arbitrary fit of the spectral amplitudes: the direct summation described by Eq. 5.15 has been performed. It was reported earlier that the 'shear noise correlations' exhibited a marked change over a radial slice of jet; such a change takes the form of a phase angle $\psi(x,y,\omega)$, as the frequency distribution appears to be unaffected by changes in the radial or azimuthal position of the source point (Fig. 6.11). The estimate of ψ is

buried in the phase angle computed by the FFT analyzer. The shear noise spectrum

$$\varphi_{pp_{SHEAR}}(\underset{\rightarrow}{x},\omega) \sim \int \omega^2 \, U_x(\underset{\rightarrow}{y}) \, |\varphi_{u_x p}(\underset{\rightarrow}{x},\underset{\rightarrow}{y},\omega)| \, e^{i\psi(\underset{\rightarrow}{x},\underset{\rightarrow}{y},\omega)} \, e^{i\omega c_o^{-1} |\underset{\rightarrow}{x}-\underset{\rightarrow}{y}|} \, d\underset{\rightarrow}{y} \quad (6.3)$$

is approximated as

$$\hat{\varphi}_{pp_{SHEAR}}(\underset{\rightarrow}{x},\omega) \sim \int \omega^2 \, U_x(\underset{\rightarrow}{y}) \, |\varphi_{u_x p}(\underset{\rightarrow}{x},\underset{\rightarrow}{y},\omega)| \, d\underset{\rightarrow}{y} \quad (6.4)$$

where $\psi(\underset{\rightarrow}{x},\underset{\rightarrow}{y},\omega)$ has been chosen to be $-\omega c_o^{-1}|x-y|$. The correct phase angle is obscured by a large experimental error; in general $\psi(\underset{\rightarrow}{x},\underset{\rightarrow}{y},\omega) \neq -\omega c_o^{-1}|\underset{\rightarrow}{x}-\underset{\rightarrow}{y}|$. The integrand in Eq. 6.4 is simply the absolute value of the integrand of the more exact shear noise spectrum estimate given by Eq. 6.3. It can be shown with the aid of the Schwartz inequality that the shear noise contribution, as computed by Eq. 6.4, overestimates the spectrum. It is encouraging, however, that the spectrum estimates are of a comparable order of magnitude. A longer averaging time is likely to improve the definition of the phase angle $\psi(\underset{\rightarrow}{x},\underset{\rightarrow}{y},\omega)$; implementation of such a scheme requires a digital computer, which was not readily available to the investigator.

The self noise spectrum computed from measured cross-spectral densities and the self noise spectrum extracted from the far field jet noise (measuring the jet noise spectrum at 90° to the jet axis and correcting for the Doppler shift and convection amplification to obtain the self noise estimate at 40° to the jet axis) are shown in Fig. 6.23. The peak amplitude of the predicted self noise spectrum is found near 3.15 KHz, whereas the self noise spectrum computed from the far field jet noise via the 'Nossier-Ribner technique' has a maximum near 2.2 KHz.

The measured cross-correlations $\overline{u_x^2(\underset{\rightarrow}{y},t)\, p(\underset{\rightarrow}{x},t-\tau)}$, in contrast to the shear noise correlations $R_{u_x p}(\underset{\rightarrow}{x},\underset{\rightarrow}{y},\tau)$, have maxima at the expected time delay of $c_o^{-1}|\underset{\rightarrow}{x}-\underset{\rightarrow}{y}|$; thus the phase angle introduced above can be set to $-\omega c_o^{-1}|\underset{\rightarrow}{x}-\underset{\rightarrow}{y}|$ with no significant error, and the estimate of the self noise at 40° to the jet axis can be treated with considerably more confidence than the corresponding shear noise estimate. The energy content of the predicted self noise spectrum is only 41% of the overall self noise spectrum. This figure is in good agreement with the 40% total energy contribution which was inferred from the behaviour of the axial source strength distribution.

One form of Ribner's theory predicts that the shear and self noise spectra have the same shape after an octave shift; the shift actually depends on the form of the time correlation of the sources (Refs. 10, 77). In Fig. 6.24 the shear noise spectrum extracted from the far field noise has been shifted in frequency and adjusted in amplitude until the spectrum nearly matched the self noise spectrum. The best fit was found for a shift of 1.6. The same frequency shift has been applied to the shear noise spectrum predicted from the cross-spectral densities. After matching the peak amplitudes, it is found that the two estimates of the frequency-shifted shear noise spectra fit the corresponding self noise spectra, as predicted by the theory. Nossier and

Ribner (Ref. 37) found that a large body of experimental jet noise data on average exhibits close to an octave shift. The frequency shift appears to be a weak monotonic function of jet velocity (Table I of Ref. 37), and thus the present result is thought to be compatible with the one of Nossier and Ribner (Ref. 37).

For the sake of completeness, the overall jet noise spectrum measured at 40° to the jet axis and the sum of the predicted self and shear noise contributions, based on the cross-spectral density measurements performed herein, are shown in Fig. 6.25. The apparent fit for frequencies greater than 2.5 KHz is for the most part due to the overestimate of the shear noise spectrum.

6.5 Concluding Remarks

Over the years Ribner's self and shear noise model, an extension of Lighthill's theory of jet noise, has been demonstrated to describe the major features of jet noise (Refs. 17, 37, 28, 24), but direct measurement of the postulated sources via a cross-correlation technique has met only limited success. The spurious 'probe noise' generated by interaction of the turbulence and the velocity sensor - the hot wire probe - is believed to be the major source of error. In the present investigation the sources, which are proportional to certain rates of momentum flux, have been measured by a 'remote' sensing technique made possible by a Laser Doppler Velocimeter that has been adapted to the special requirements of the correlation measurements.

Cross-correlations and cross-spectral densities of the postulated self and shear noise source terms and the radiated sound have been measured. For radiation to the field point at 40° to the jet axis, the effective instantaneous source patterns of the self and shear noise, as derived from the cross-spectra, show a marked deviation from axisymmetry. Nominal source patterns, proportional to $\overline{u_x^2 U_x^2}$ for the shear noise and $\overline{(u_x^2)^2}$ for the self noise, are qualitatively similar to the measured source patterns. The effective source patterns are observer oriented, and not fixed to particular jet flow coordinates; this property assures that the overall radiated mean square sound pressure is axisymmetric, even though the instantaneous sound pressure is not.

The self and shear noise spectra predicted from an aggregate of cross-spectral density measurements of the postulated source terms and the radiated sound are compatible with the self and shear noise spectra extracted from far field jet noise measurements. The source region surveyed herein ($y_1/D = 3$ to 7) appears to radiate about 40% of the total jet noise heard by the observer; therefore the predicted self and shear noise spectra are not one to one with those extracted via the 'Nossier-Ribner' algorithm.

Both sets of self and shear noise spectra do match very nearly in shape and exhibit a common frequency shift, and both sets have comparable absolute spectral amplitudes; this behaviour is predicted by the theory. The compatibility suggests that the theory is internally consistent and lends it substantial further credibility.

REFERENCES

1. Lighthill, M. J. — On Sound Generated Aerodynamically. I - General Theory. Proceedings of the Royal Society, A211, pp. 564-587, 1952.

2. Lighthill, M. J. — On Sound Generated Aerodynamically. II - Turbulence as a Source of Sound. Proceedings of the Royal Society, A222, pp. 1-32, 1954.

3. Olsen, W. A.; Gutierrez, O. A.; Dorsch, R. G. — The Effect of Nozzle Inlet Shape, Lip Thickness, and Exit Shape and Size on Subsonic Jet Noise. NASA TM X 68182, 1973.

4. Proudman, I. — The Generation of Noise by Isotropic Turbulence. Proceedings of the Royal Society, A214, pp. 119-132, 1952.

5. Lilley, G. M. — On the Noise from Air Jets. Aeronautical Research Council, U.K. ARC 20, 376-N40-FM 2724, 1958.

6. Ribner, H. S. — Aerodynamic Sound from Fluid Dilatations, A Theory of the Sound from Jets and Other Flows. Univ. of Toronto, Institute of Aerophysics, UTIA Rep. 86, 1962.

7. Ribner, H. S. — On the Strength Distribution of Noise Sources Along a Jet. Univ. of Toronto, Institute of Aerophysics, UTIA Rep. 51, 1958; abridged in Jour. of the Acoustical Society of America, Vol. 30, No. 9, p. 876, 1958.

8. Powell, A. — Similarity Considerations of Noise Production from Turbulent Jets, Both Static and Moving. Douglas Aircraft Co., Rep. SM-23246, 1958; abridged in Jour. of the Acoustical Society of America, Vol. 31, No. 6, pp. 812-813, 1959.

9. Ribner, H. S. — On Spectra and Directivity of Jet Noise. Jour. of the Acoustical Society of America, Vol. 35, No. 4, pp. 614-616, 1963; see also The Generation of Sound by Turbulent Jets. Advances in Applied Mechanics, Vol. 8, Academic Press, New York, pp. 103-182, 1964.

10. Ribner, H. S. — Quadrupole Correlations Governing the Pattern of Jet Noise. Jour. of Fluid Mechanics, Vol. 38, pp. 1-24, 1969.

11. Ffowcs-Williams, J. E. — The Noise from Turbulence Convected at High Speed. Philosophical Transactions of the Royal Society, A255, pp. 469-503, 1963.

12. Powell, A. — Survey of Experiments in Jet Noise. Aircraft Engineering, 26, pp. 2-9, 1954.

13. Atvars, J.; Schubert, L. K.; Ribner, H. S. — Refraction of Sound from a Point Source Placed in an Air Jet. AIAA Paper No. 65-82, Presented at AIAA 2nd Aerospace Sciences Meeting, New York, 1965.

14. Atvars, J.; Schubert, L. K.; Grande, E.; Ribner, H. S. — Refraction of Sound by Jet Flow or Jet Temperature. NASA CR-494, May 1966.

15. Schubert, L. K. — Numerical Study of Sound Refraction by a Jet Flow. I Ray Acoustics. Jour. of the Acoustical Society of America, Vol. 51, No. 2, pp. 439-446, 1972.

16. Schubert, L. K. — Numerical Study of Sound Refraction by a Jet Flow. II. Wave Acoustics. Jour. of the Acoustical Society of America, Vol. 51, No. 2, 447-463, 1972.

17. MacGregor, G. R.; Ribner, H. S.; Lam, H. — 'Basic' Jet Noise Patterns After Deletion of Convection and Refraction Effects: Experiments vs Theory. Jour. of Sound and Vibration, Vol. 27, No. 4, pp. 437-454, 1973.

18. Phillips, O. M. — On the Generation of Sound by Supersonic Turbulent Shear Layers. Jour. of Fluid Mechanics, 9, pp. 1-28, 1960.

19. Chiu, H. H.; Summerfield, M. — Theory of Combustion Noise. Presented at the 4th International Coloquium on Gasdynamics of Explosions and Reactive Systems, San Diego, California, 1973.

20. Lilley, G. M. — The Generation and Radiation of Supersonic Jet Noise. Air Force Aero-Propulsion Lab., AF Systems Command, Wright Patterson Air Force Base, Ohio, AFAPL TR-72-53, Vol. IV, 1972.

21. Tester, B. J.; Morfey, C. L. — Developments in Jet Noise Modelling - Theoretical Predictions and Comparisons with Measured Data. Jour. of Sound and Vibration, Vol. 46, No. 1, pp. 79-103, 1974.

22. Balsa, T. F.; Gliebe, P. R. — Aerodynamics and Noise of Coaxial Jets. AIAA Jour. Vol. 15, No. 11, pp. 1550-1558, 1977.

23. Mani, R. — The Influence of Jet Flow on Jet Noise. Part I. The Noise of Unheated Jets. Jour. of Fluid Mechanics, 35, pp. 101-117, 1976.

24. Ribner, H. S. — The Issue of Source Terms for Jet Noise. AIAA Paper No. 76-487, Presented at the AIAA 3rd Aeroacoustics Conference, 1976; Revised as On the Role of the Shear Term in Jet Noise. Jour. of Sound and Vibration, 52(1), pp. 121-132, 1977.

25. Michalke, A. — On the Effect of Spatial Source Coherence on the Radiation of Jet Noise. Jour. of Sound and Vibration, 55(3), pp. 377-394, 1977.

26. Ffowcs-Williams, J. E. Kempton, A. D. — The Noise from the Large-Scale Structure of a Jet. Jour. of Fluid Mechanics, 84(4), pp. 673-694, 1978.

27. Maestrello, L. — Two-Point Correlations of Sound Pressure in the Far Field of a Jet: Experiment. NASA TM X-72835, 1976.

28. Ribner, H. S. — Theory of Two-Point Correlations of Jet Noise. NASA TN D8330, 1976; also Two Point Correlations of Jet Noise. Jour. of Sound and Vibration, 56(1), pp. 1-19, 1978.

29. Meecham, W. C. Ford, G. W. — Acoustic Radiation from Isotropic Turbulence. Jour. of the Acoustical Society of America. Vol. 30, No. 4, pp. 318-322, 1958.

30. Corcos, G. M. — Some Measurements Bearing on the Principle of Operation of Jet Silencing Devices. Douglas Aircraft Co., Santa Monica Div. Rep. SM-23114, 1958.

31. Ribner, H. S. — New Theory of Jet Noise Generation, Directionality, and Spectra. Jour. of the Acoustical Society of America, Vol. 31, No. 2, pp. 245-246, 1959.

32. Lighthill, M. J. — Jet Noise (Wright Brothers Lecture). AIAA Jour., Vol. 1, No. 7, pp. 1507-1517, 1963.

33. Hurdle, P. M. Meecham, W. C. — Investigation of the Aerodynamic Noise Generating Region of a Jet Engine by Means of the Simple Source Fluid Dilatation Model. Jour. of the Acoustical Society of America, Vol. 56, No. 6, pp. 1708-1721, 1974.

34. Siddon, T. E. Rackl, R. — Cross-Correlation Analysis of Flow Noise with Fluid Dilatation as Source Fluctuation. Jour. of the Acoustical Society of America, Vol. 51, No. 1 (Abstract), p. 96, 1972.

35. Planchon, H. P. Jones, B. G. — A Study of the Local Pressure Field in Turbulent Shear Flow and Its Relation to Aerodynamic Noise Generation - A Study of the Mixing Region of a Round Jet. Proc. of the Second Interagency Symposium on University Research in Transportation Noise, North Carolina State Univ., pp. 20-35, 1974.

36. Krich, R.
Jones, B. G.
Hammersley, R. J.
Planchon, H. P.
Weber, D. P.
Prediction of Far Field Sound Power Level for Jet Flows from Flow Field Pressure Model. AIAA Paper No.

37. Nossier, N. S. M.
Ribner, H. S.
Tests of a Theoretical Model of Jet Noise. AIAA Paper No. 75-436, 1975.

38. Chu, W. T.
Turbulence Measurements Relevant to Jet Noise. Univ. of Toronto, Institute for Aerospace Studies, UTIAS Rep. 119, 1966.

39. Lee, H. K.
Ribner, H. S.
Direct Correlation of Noise and Flow of a Jet. Jour. of the Acoustical Society of America, Vol. 52, No. 5, pp. 1280-1290, 1972.

40. Seiner, J. M.
Reethof, G.
On the Distribution of Source Coherency in Subsonic Jets. AIAA Paper No. 74-4, 1974.

41. Morris, P. J.
Hot Wire-Microphone Cross-Correlations Based on Ribner's Source Terms, to Indicate Separately the Shear-Noise and Self-Noise Contributions to Jet Noise. Univ. of Toronto, Institute for Aerospace Studies, Unpublished, 1972.

42. Curle, N.
The Influence of Solid Boundaries Upon Aerodynamic Sound. Proc. of the Royal Society, A231, pp. 505-514, 1955.

43. Clark, P. J. F.
Ribner, H. S.
Direct Correlation of Fluctuating Lift With Radiated Sound for an Airfoil in Turbulent Flow. Jour. of the Acoustical Society of America, Vol. 52, No. 3, pp. 802-805, 1969.

44. Yeh, Y.
Cummins, H. Z.
Localized Fluid Flow Measurements With an He Ne Laser Spectrometer. Applied Physics Letters, 4, pp. 176-178, 1964.

45. Scott, P.
Ahlgrin, F.
Knott, P.
In-Jet/Far-Field Cross-Correlation Experiments. Supersonic Jet Exhaust Noise Investigation, Vol. II, Tech. Rep. AFARL TR-76-68, General Electric Co., Advanced Engineering and Technology Prog. Dept., Aircraft Engine Grp., Air Force Aeropropulsion Lab., pp. 417-457, 1976.

46. Goldstein, M. E.
Aeroacoustics. NASA SP 346, pp. 1-7, 1974. Also in Aeroacoustics, McGraw-Hill, New York, pp. 1-6, 1976.

47. Stratton, J. A.
Electromagnetic Theory. McGraw-Hill, New York, pp. 424-427, 1941.

48. Tatarski, V. I. — Wave Propagation in a Turbulent Medium. McGraw-Hill, New York, pp. 3-8, 1961.

49. Crandall, S. H. (Ed.) — Random Vibration. MIT Press, Cambridge, Mass., pp. 1-10, 1963.

50. Siddon, T. E. — Noise Source Diagnostics Using Causality Correlations. AGARD Conference Proceedings No. 131 on Noise Mechanisms. AGARD CP 131, pp. 7.1 - 7.12, 1973.

51. Wiener, N. — Time Series. MIT Press, Cambridge, Mass. (First printing 1949), pp. 37-43, 1977.

52. Lighthill, M. J. — Introduction to Fourier Analysis and Generalized Functions. Cambridge at the University Press, pp. 16-21, 1958.

53. Van De Hulst, H. C. — Light Scattering by Small Particles. John Wiley, New York, pp. 114-130, 1957.

54. Anon. — The Accuracy of Flow Measurements by Laser Doppler Methods. Proc. of the LDA Symposium, Copenhagen, 1975 (P.O. Box 70, DK-2740, Skovlunde, Denmark), 1976.

55. Durst, F.; Melling, A.; Whitelaw, J. H. — Principles and Practice of Laser-Doppler Anemometry. Academic Press, London, 1976.

56. Anon. — Laser Anemometer Systems. Thermo-Systems, Inc., TSI 900-275, pp. 46-53, 1975.

57. Melling, A.; Whitelaw, J. H. — Seeding of Gas Flows for Laser Doppler Anemometry. DISA Information No. 15, pp. 5-14, 1973.

58. Yanta, W. J.; Gates, D. F.; Brown, F. W. — The Use of a Laser Doppler Velocimeter in Supersonic Flow. AIAA Paper No. 71-287, 1971.

59. Atvars, J — Refraction of Sound by a Jet Velocity Field. M.A.Sc. Thesis (unpublished), Univ. of Toronto, Institute for Aerospace Studies, 1964.

60. Berger, E.; Freymuth, P.; Froebel, E. — Use of Feedback Control in the Development of a Constant-Temperature Hot-Wire Anemometer. (DVLR Bericht Nr. 282, 1963), Boeing Scientific Research Laboratories Translations, 1963.

61. Lee, H.K. — Correlation of Noise and Flow of a Jet. Univ. of Toronto, Institute for Aerospace Studies, UTIAS Rep. 168, 1971.

62. Bendat, J. S.; Piersol, A. G. — Random Data: Analysis and Measurement Procedures. Wiley-Interscience, New York, pp. 38-41, 1971.

63. Blokhintsev, D. I. — Acoustics of a Nonhomogeneous Moving Medium. NACA TM 1399, 1956.

64. Kraichnan, R. K. — The Scattering of Sound in a Turbulent Medium. Jour. of the Acoustical Society of America, Vol. 25, No. 6, pp. 1096-1104, 1953.

65. Clifford, S. F. Brown, E. H. — Propagation of Sound in a Turbulent Atmosphere. Jour. of the Acoustical Society of America, Vol. 48, No. 5, pp. 1123-1127, 1970.

66. Nayar, B. M. Siddon, T. E. Chu, W. T. — Properties of the Turbulence in the Transition Region of a Round Jet Univ. of Toronto, Institute for Aerospace Studies, UTIAS TN 131, 1969.

67. Bradshaw, P. Ferriss, D. H. Johnson, R. F. — Turbulence in the Noise Producing Region of a Circular Jet. National Physical Laboratory, Aerodynamics Division, Rep. 1054, 1963.

68. Nossier, N. S. N. — Correlation of Jet Noise Data in Terms of a Self Noise-Shear Noise Model. Univ. of Toronto, Institute for Aerospace Studies, UTIAS TN 193, 1975.

69. McLaughlin, D. K. Tiederman, W. G. — Biasing Correction for Individual Realization of Laser Anemometer Measurements in Turbulent Flows. The Physics of Fluids, Vol. 16, No. 12, pp. 2082-2088, 1973.

70. Steenstrup, F. V. — Counting Techniques Applied to Laser Doppler Anemometry. DISA Information No. 18, pp. 21-25, 1975.

71. Jerri, A. J. — The Shannon Sampling Theorem - Its Various Extensions and Applications: A Tutorial Review. Proc. of the IEEE, Vol. 65, No. 11, pp. 1565-1596, 1977.

72. Cliff, W. C. Fuller, C. E. Sandborn, V. A. — Simultaneous Comparison of Turbulent Gas Fluctuations by Laser Doppler and Hot Wire. AIAA Jour., Vol. 11, No. 5, pp. 748-749, 1973.

73. Bass, H. E. Douglas Shields, F. — Absorption of Sound in Air: High Frequency Measurements. Jour. of the Acoustical Society of America, Vol. 63, No. 3, pp. 571-576, 1977.

74. Grosche, F. R. Jones, J. H. Wolhold, G. A. — Measurements of the Distribution of Sound Source Intensities in Turbulent Jets. AIAA Paper No. 73-989, 1973; see also Aeroacoustics: Jet and Combustion Noise; Duct Acoustics, H. T. Nagamatsu, Ed., Vol. 37 of the Progress in Astronautics and Aeronautics Series, pp. 79-92, 1975.

75. Fisher, M. J.
Harper-Bourne, M.
Glegg, S. A. L.
Jet Engine Noise Source Location: The Polar Correlation Technique. Jour. of Sound and Vibration, Vol. 51, No. 1, pp. 23-54, 1977.

76. Billingsley, J.
Kinns, R.
The Acoustic Telescope. Jour. of Sound and Vibration, Vol. 51, No. 1, pp. 23-54, 1977.

77. McCartney, J. R.
Ratio of Peak Frequencies of Jet Self and Shear Noise. Jour. of Sound and Vibration, Vol. 39, No. 2, pp. 269-272, 1975.

78. Pao, S. P.
Lowson, M. V.
Spectral Techniques in Jet Noise Theory. Wyle Laboratories Research Staff Rep. WR 68-21, 1969.

79. Batchelor, G. K.
The Theory of Homogeneous Turbulence. Cambridge University Press, Cambridge, pp. 45-54, 1956.

80. Townsend, A. A.
The Structure of Turbulent Shear Flow. Cambridge University Press, Cambridge, pp. 45-54, 1956.

81. Schlichting, H.
Boundary Layer Theory. McGraw-Hill, New York, 1968.

82. Davies, P.O.A.L.
Fisher, M. J.
Barratt, M. J.
The Characteristics of the Turbulence in the Mixing Region of a Round Jet. Jour. of Fluid Mechanics, Vol. 15, pp. 337-367, 1963.

83. Morse, P. M.
Vibration and Sound. McGraw-Hill, New York, pp. 346-357, 1948.

84. Rackl, R.
Two Causality Correlation Techniques Applied to Jet Noise. Ph.D. Dissertation, Dept. of Mech. Eng., Univ. of British Columbia, Appendix D, 1973.

85. Harris, F. J.
Trigonometric Transforms. Spectral Dynamics Corp., Tech. Publication DSP 005 6/76, pp. 12-19, 1976.

86. Harris, F. J.
On the Use of Windows for Harmonic Analysis with the Discrete Fourier Transform. Proc. of the IEEE, Vol. 66, No. 1, pp. 51-83, 1978.

87. Blackman, R. B.
Tukey, J. W.
The Measurement of Power Spectra. Dover Publications, New York, pp. 11-14, 1958.

88. Gradshteyn, I. S.
Ryzhik, I. M.
Table of Integrals, Series, and Products. Academic Press, New York, p. 7, 1965.

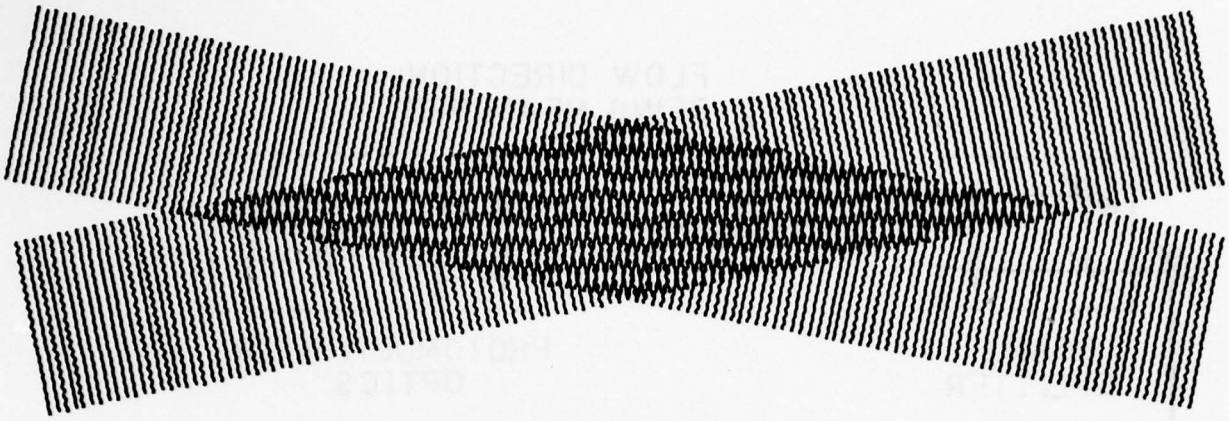


FIG. 3.1 MOIRE PATTERN MODEL OF THE INTERSECTION OF TWO COHERENT LIGHT BEAMS. LINES MAY BE THOUGHT OF AS SURFACES OF EQUAL PHASE. [REF. DURST, F., STEVENSON, W. H., MOIRE PATTERNS TO VISUALLY MODEL LASER DOPPLER SIGNALS, APPLIED OPTICA, VOL. 15, 1, PP. 137-144 (1976)]

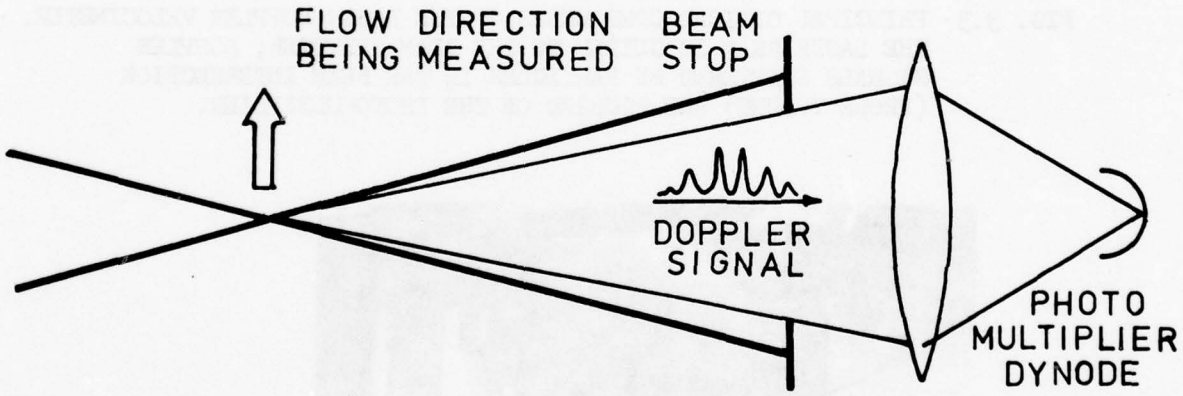


FIG. 3.2 SCHEMATIC OF THE DIFFERENTIAL MODE OF LASER DOPPLER SIGNAL DETECTION. 'DOPPLER BURSTS' SCATTERED BY PARTICLES TRAVERSING THE BEAM INTERSECTION ARE FOCUSED ON THE PHOTOMULTIPLIER DYNODE.

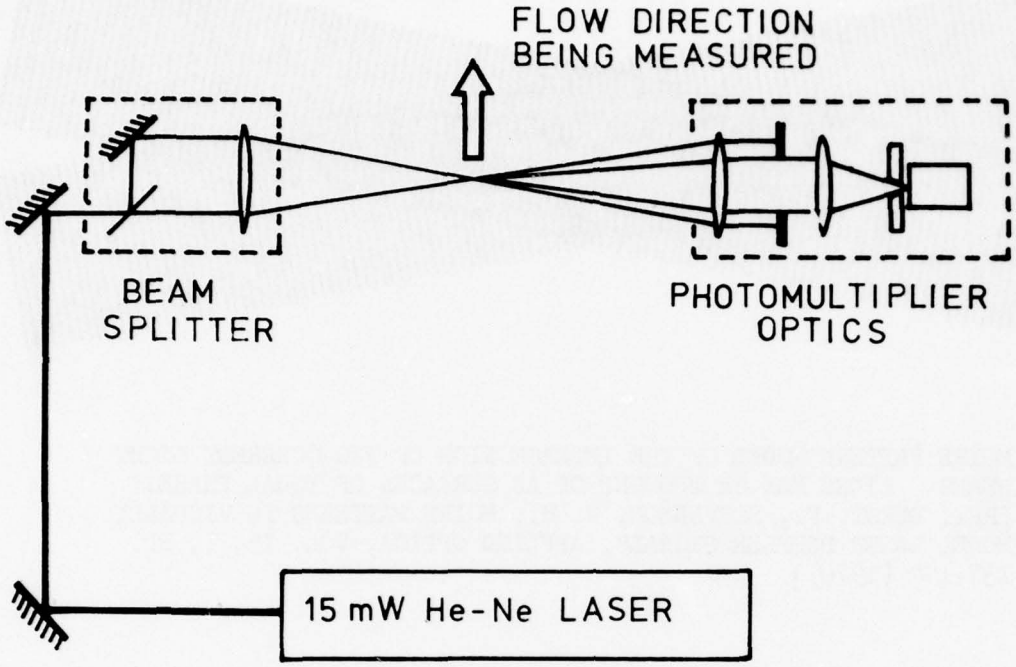


FIG. 3.3 PRINCIPAL OPTICAL COMPONENTS OF THE LASER DOPPLER VELOCIMETER. THE LASER BEAM IS GUIDED TO THE BEAM SPLITTER; DOPPLER SIGNALS SCATTERED BY PARTICLES IN THE BEAM INTERSECTION (PROBE VOLUME) ARE FOCUSED ON THE PHOTOMULTIPLIER.

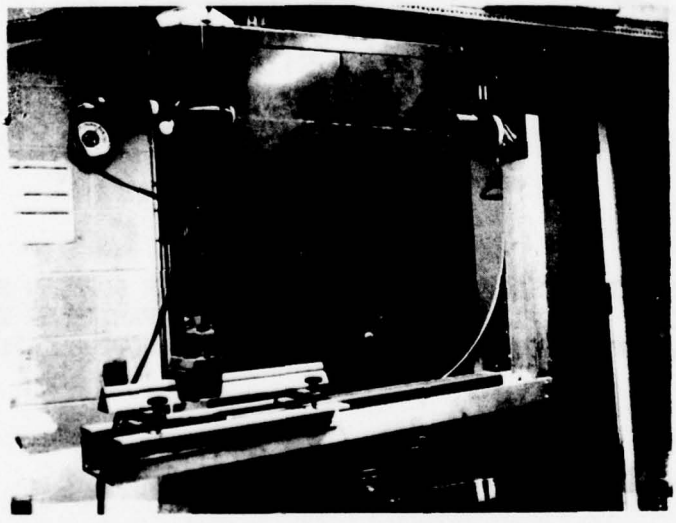


FIG. 3.4 LASER DOPPLER VELOCIMETER OPTICAL PACKAGE.

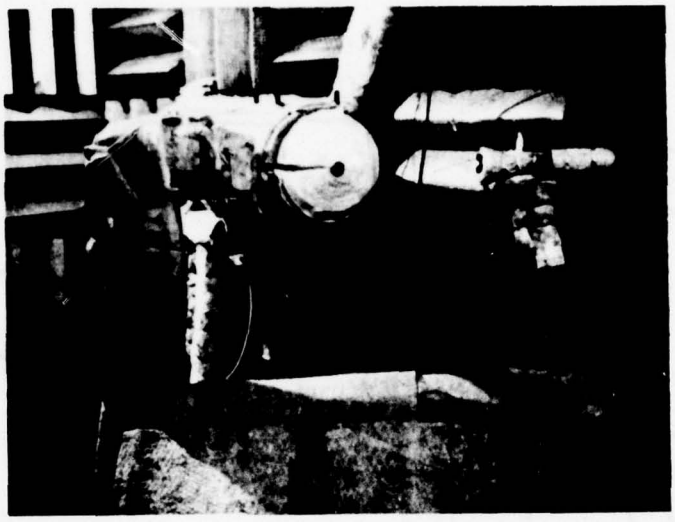


FIG. 3.5 LASER DOPPLER VELOCIMETER OPTICS AFTER INSTALLATION IN UTIAS ANECHOIC ROOM.

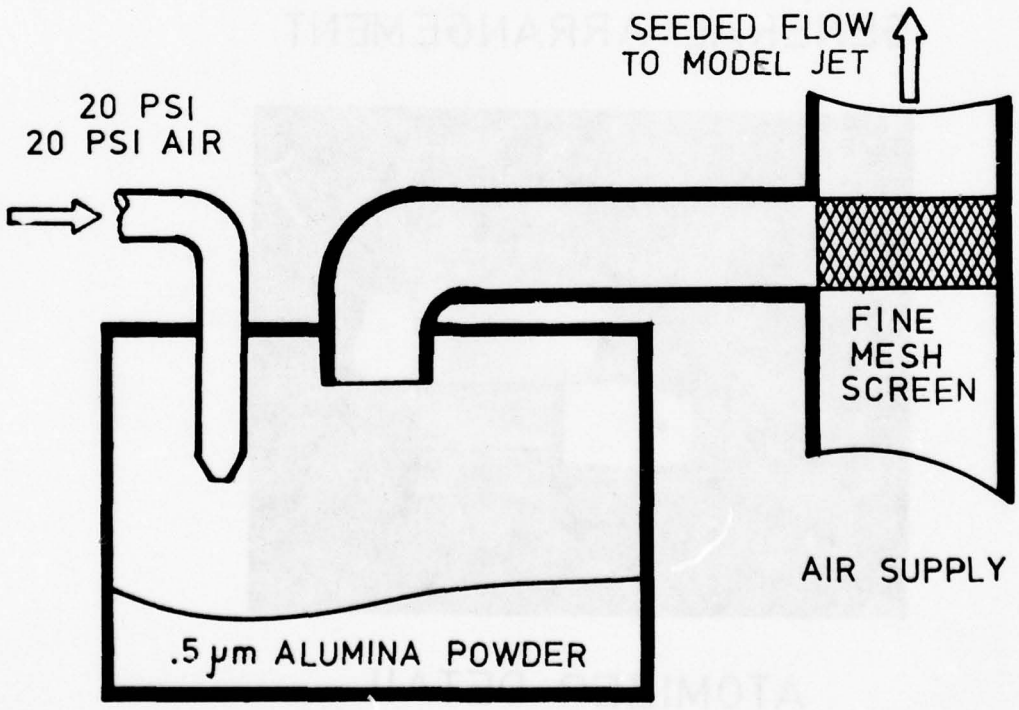
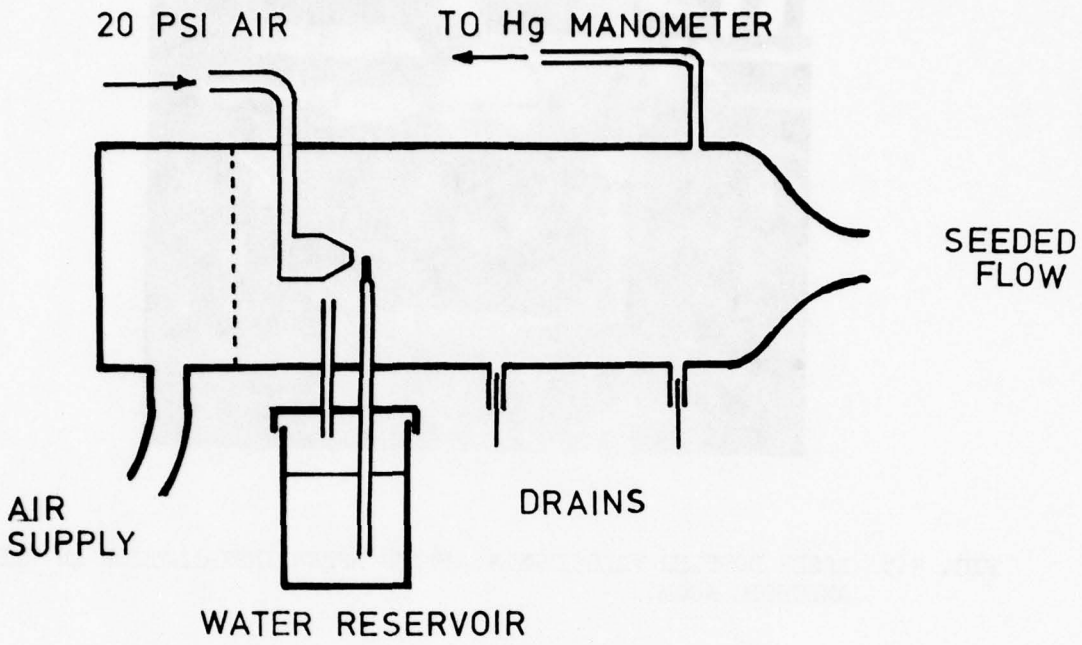
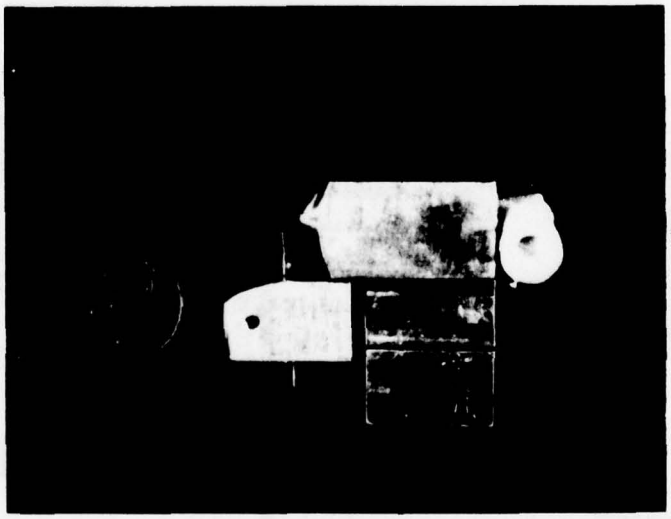


FIG. 3.6 SEEDING GENERATOR FOR .5 μm ALUMINA POLISHING POWDER.



GENERAL ARRANGEMENT



ATOMIZER DETAIL

FIG. 3.7 ATOMIZER INSTALLED IN UTIAS 3/4" MODEL JET.

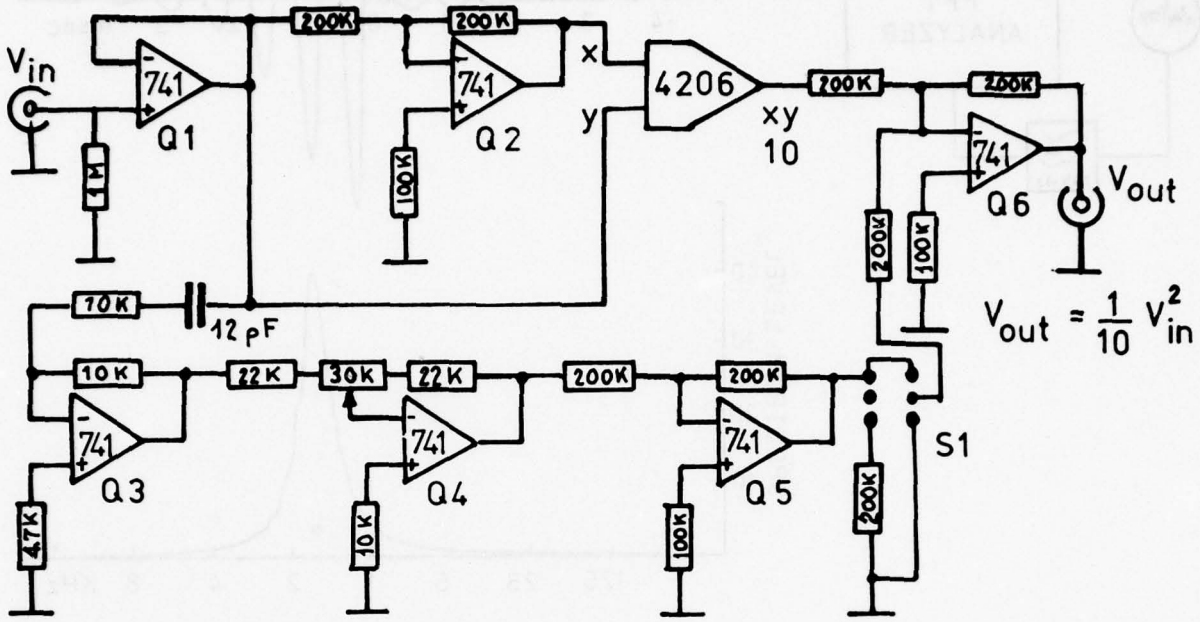


FIG. 3.8 ANALOG SQUARING CIRCUIT WITH AC FEEDTHROUGH CORRECTION.

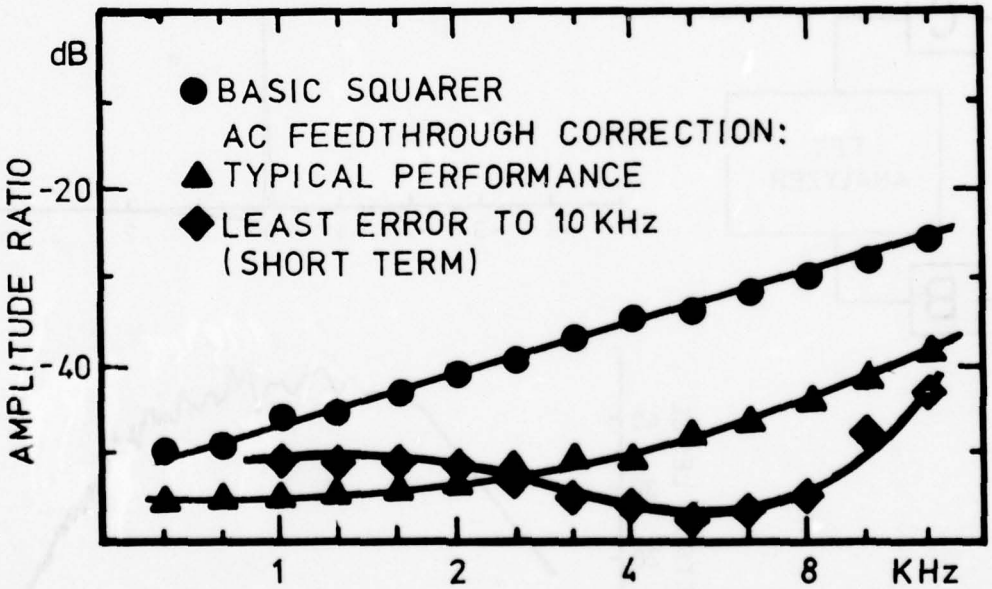


FIG. 3.9 AC FEEDTHROUGH AS A FUNCTION OF FREQUENCY f. VERTICAL SCALE: RATIO OF THE RMS OF THE RESIDUAL FREQUENCY AT f KHz AND THE SQUARED SIGNAL AT 2f KHz. NOTE THE f^{+1} DEPENDENCE OF THE BASIC SQUARER.

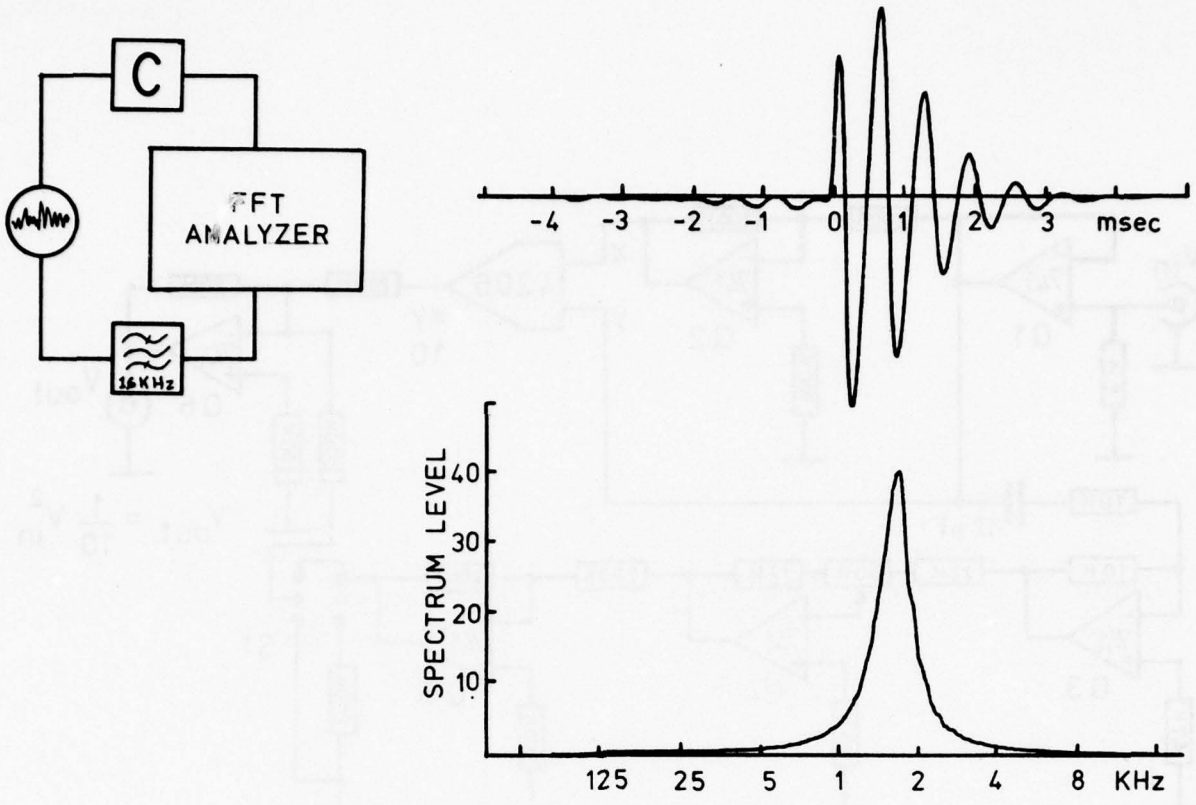


FIG. 4.1 MODEL EXPERIMENT ILLUSTRATING THE EFFECT OF SEVERELY MISMATCHED TRANSDUCERS ON THE ESTIMATES OF CROSS-CORRELATION AND CROSS-SPECTRAL DENSITY FUNCTIONS.

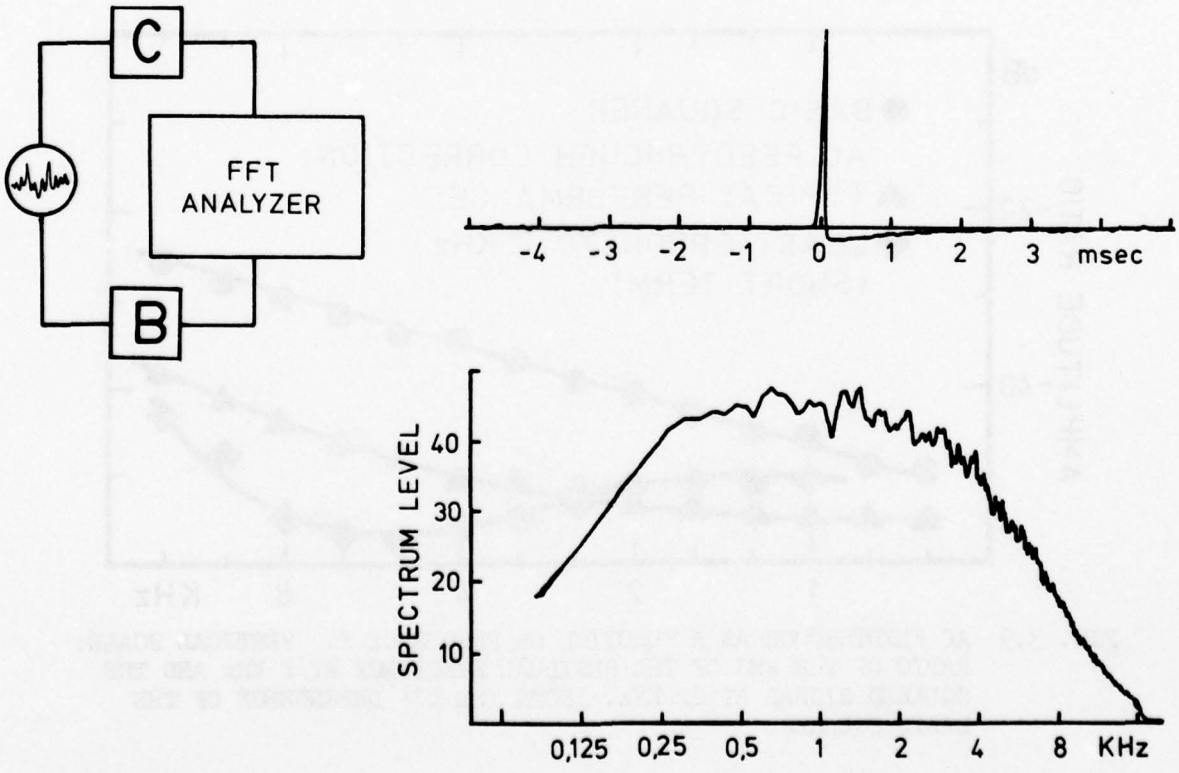


FIG. 4.2 MODEL EXPERIMENT ILLUSTRATING THE EFFECT OF SLIGHTLY MISMATCHED TRANSDUCERS ON THE ESTIMATES OF CROSS-CORRELATION AND CROSS-SPECTRAL DENSITY FUNCTIONS.

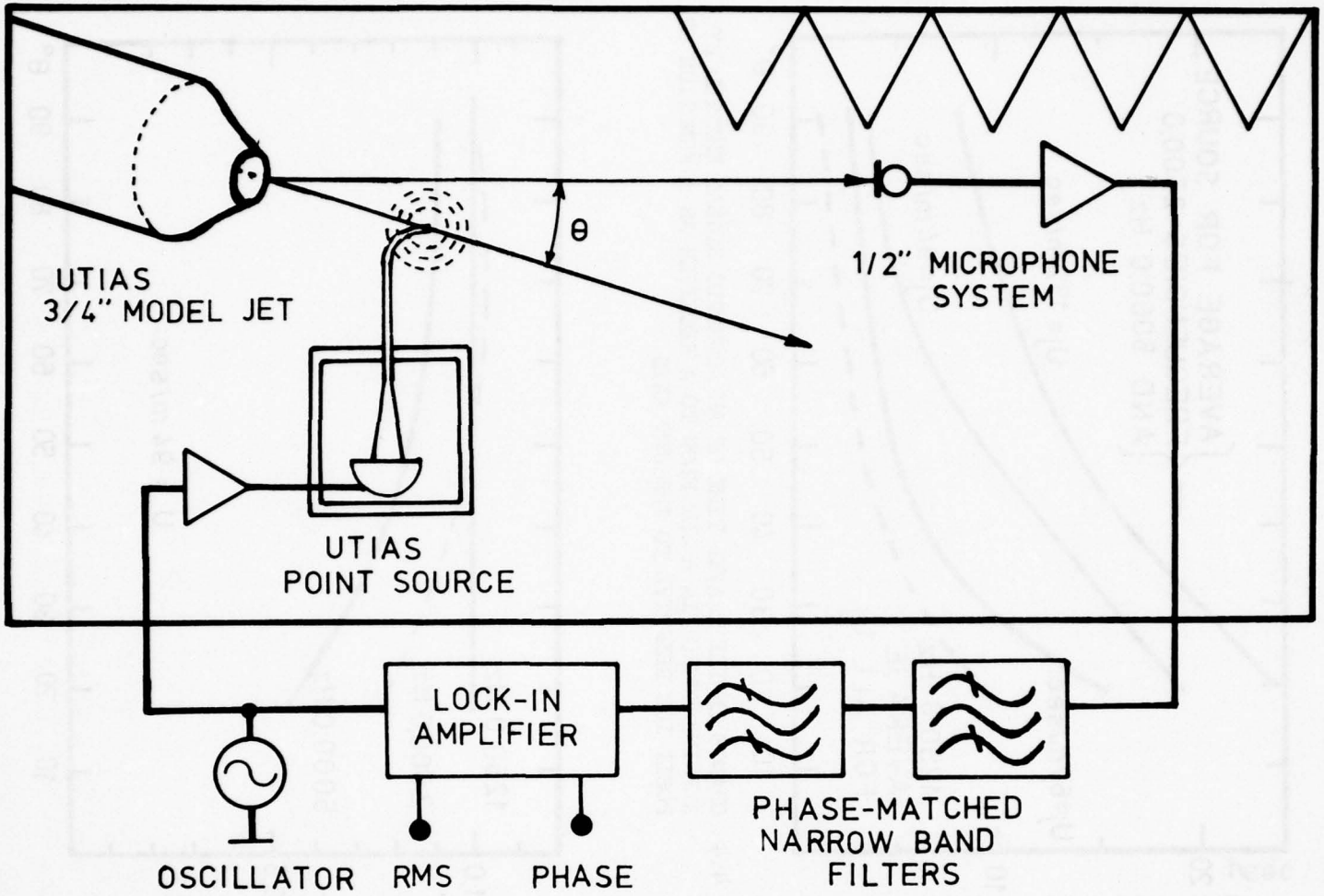


FIG. 4.3 EXPERIMENTAL ARRANGEMENT FOR THE DETECTION OF SOUND-FLOW INTERACTION. THE CHANGE IN RMS LEVEL AND PHASE OF THE PURE TIME EMITTED BY THE POINT SOURCE IS MEASURED FOR VARIOUS JET VELOCITIES, SOURCE AND RECEIVER POSITIONS.

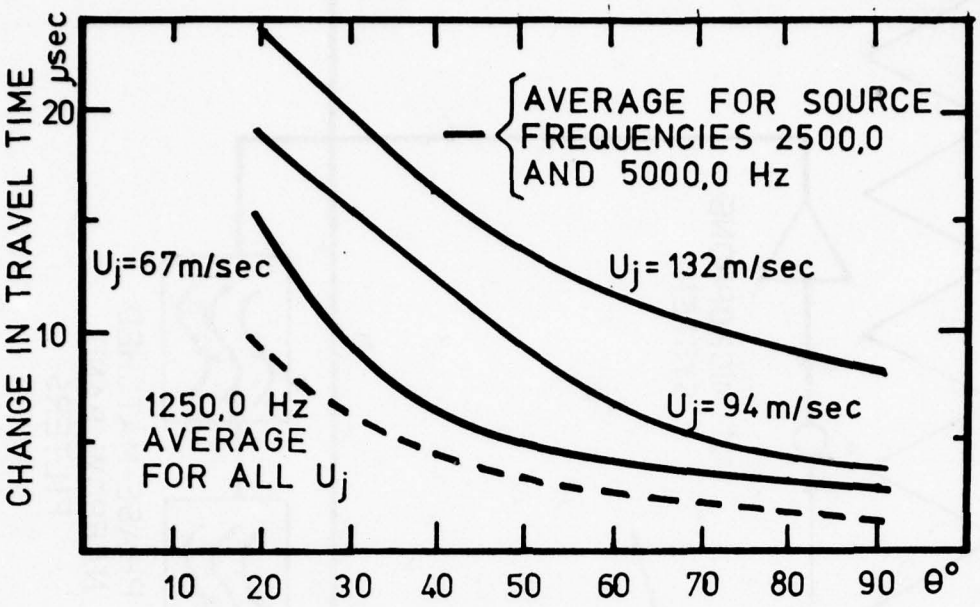


FIG. 4.4 CHANGE IN THE TRAVEL TIME OF AN ACOUSTIC SIGNAL EMITTED BY A POINT SOURCE IN A JET FLOW TO A RECEIVER AS A FUNCTION OF POSIT ION RELATIVE TO THE JET AXIS.

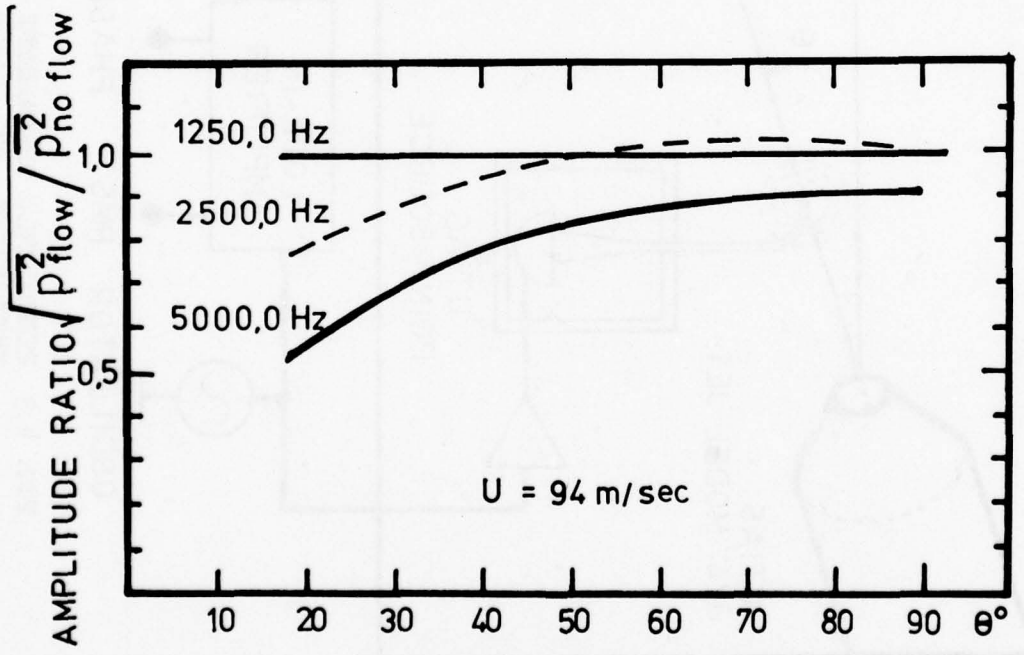


FIG. 4.5 NORMALIZED RMS LEVEL OF AN ACOUSTIC SIGNAL EMITTED BY A POINT SOURCE IN A JET FLOW AS A FUNCTION OF RECEIVER POSITION RELATIVE TO THE JET AXIS. REFRACTION IS THE MAJOR MECHANISM THAT MODIFIES THE DIRECTIVITY OF THE RADIATION EMITTED BY THE POINT SOURCE. (ATVARS ET AL, REF. 13)

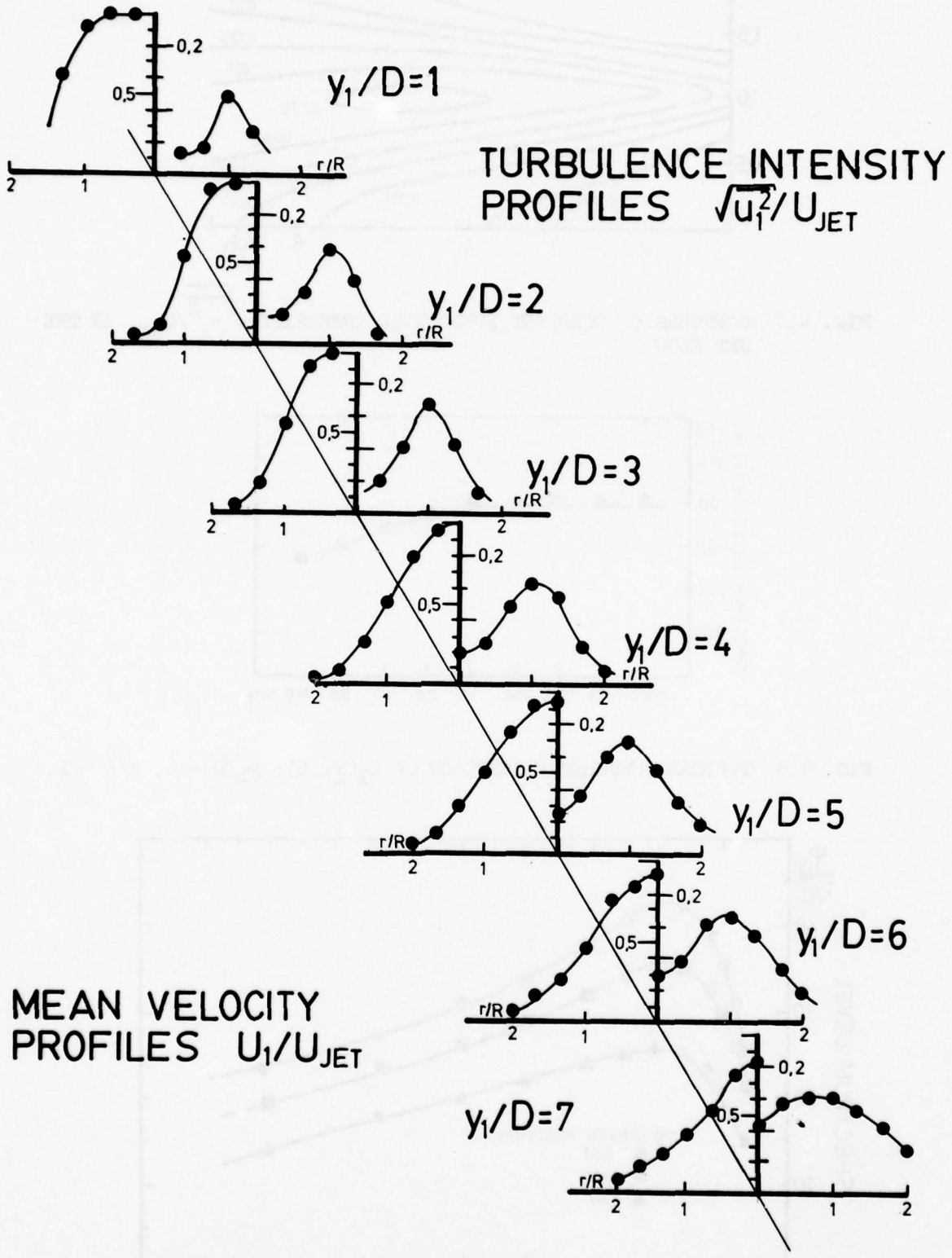


FIG. 4.6 MEAN VELOCITY AND TURBULENCE INTENSITY PROFILES OF THE UTIAS 3/4" MODEL JET (HOT WIRE ANEMOMETER DATA).

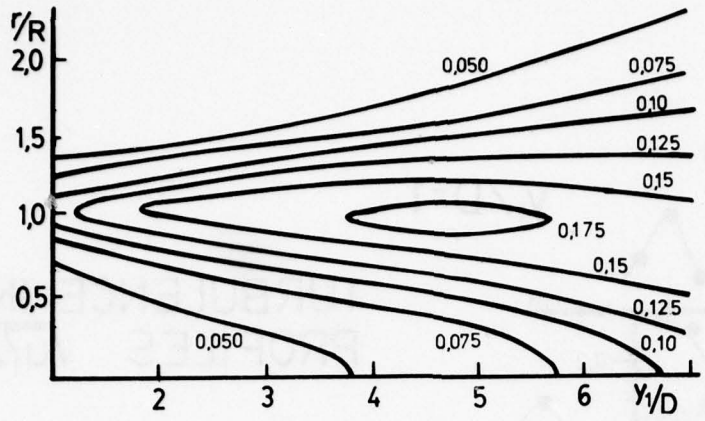


FIG. 4.7 CONTOURS OF CONSTANT TURBULENCE INTENSITY $\sqrt{\overline{u_1^2}}/U_{JET}$ IN THE JET FLOW.

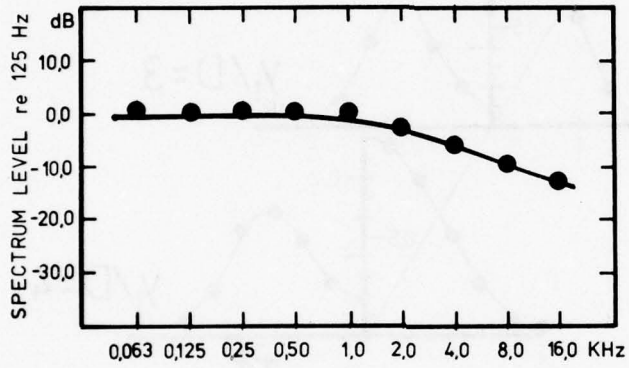


FIG. 4.8 TYPICAL TURBULENCE SPECTRUM OF $u_1(\underset{\sim}{y}, t)$; $y_1/D = 6$, $r/R = 1$.

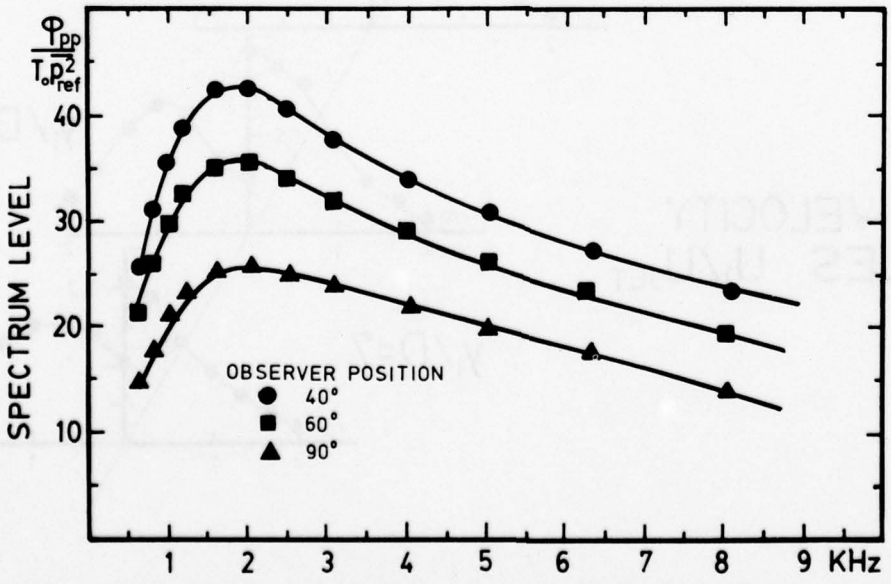


FIG. 4.9 FAR FIELD JET NOISE SPECTRA OF THE UTIAS 3/4" MODEL JET AT VARIOUS OBSERVER POSITIONS RELATIVE TO THE JET AXIS. JET VELOCITY 105 M/SEC, VERTICAL SCALE (LINEAR) IS REFERENCED TO AN ARBITRARY LEVEL.

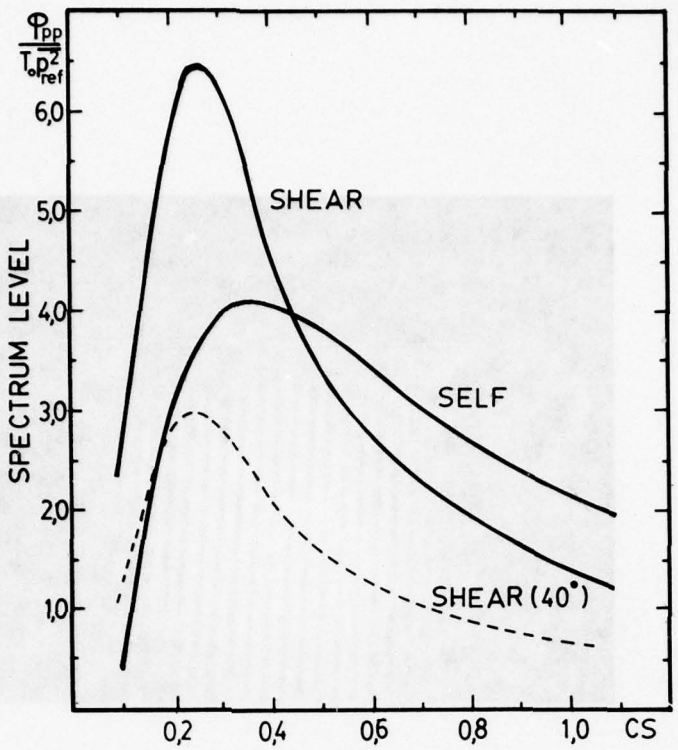


FIG. 4.10 RELATIVE AMPLITUDES OF SELF AND SHEAR NOISE SPECTRA COMPUTED FROM FAR FIELD JET NOISE MEASUREMENTS (FIG. 4.9). ---- SHEAR NOISE CONTRIBUTION AT 40° TO THE JET AXIS.

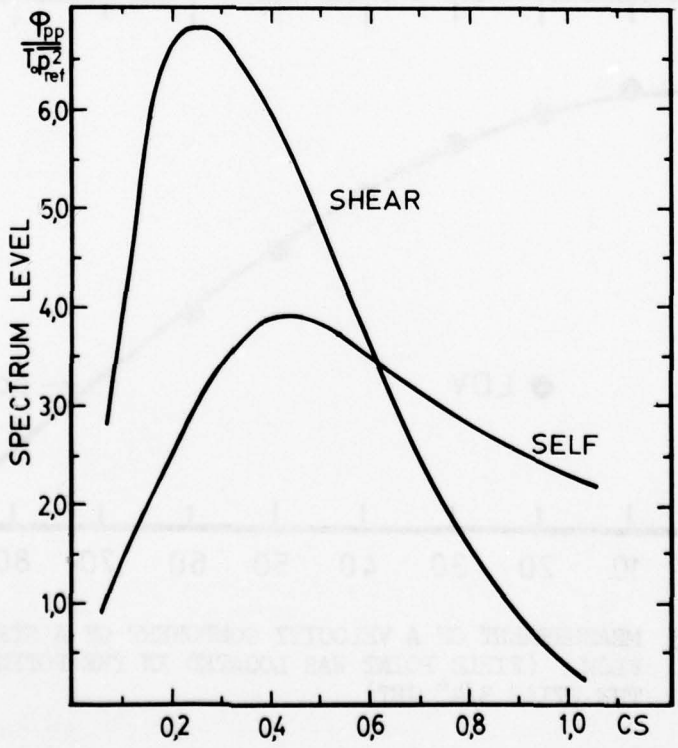


FIG. 4.11 RELATIVE AMPLITUDE OF SELF AND SHEAR NOISE SPECTRA; RE-PLOTTED FROM NOSSIER. [REF. 68, FIG. 10; ORIGINAL FAR FIELD DATA: AHEYA, K. K., CORRELATION AND PREDICTION OF JET NOISE, JOUR. OF SOUND AND VIBR., VOL. 29 (2), PP. 155-168 (1973); JET DIAMETER 1.52", JET VELOCITY 122 M/SEC]

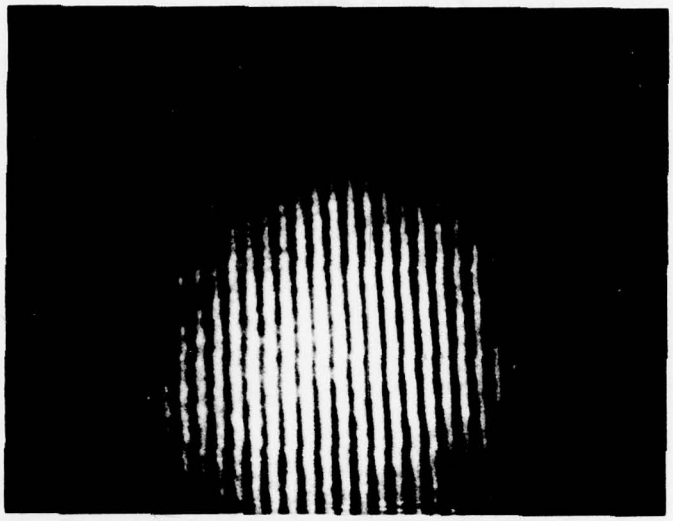


FIG. 4.12 IMAGE OF THE FRINGE PATTERN IN THE PROBE VOLUME.

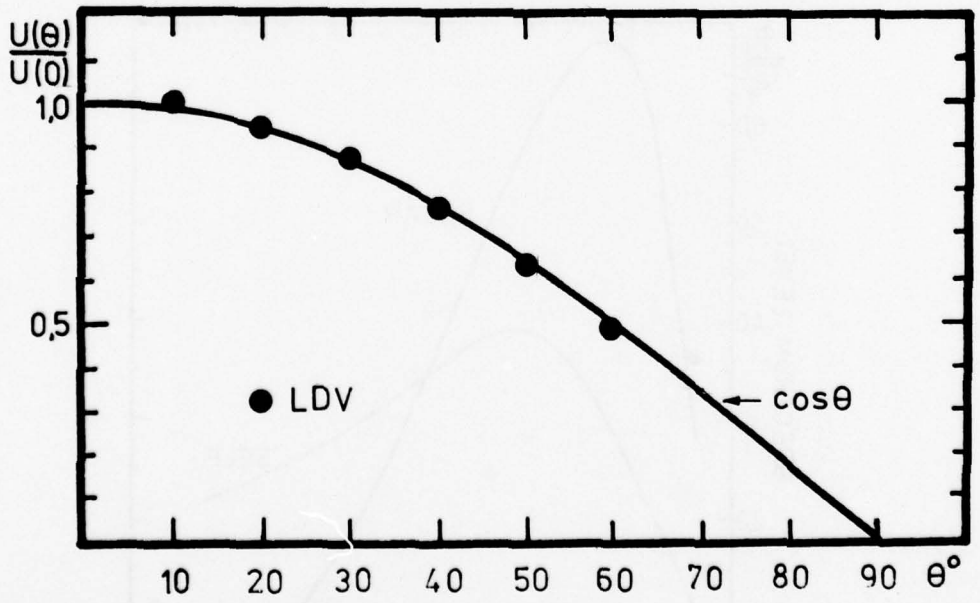


FIG. 4.13 MEASUREMENT OF A VELOCITY COMPONENT OF A STEADY LAMINAR FLOW. (FIELD POINT WAS LOCATED IN THE POTENTIAL CORE OF THE UTIAS 3/4" JET)

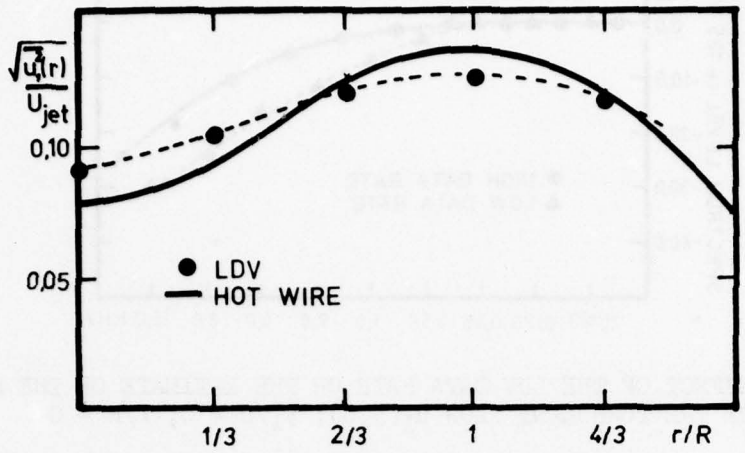


FIG. 4.14 TURBULENCE INTENSITY PROFILE OF THE JET FLOW AT $y_1/D = 6$: COMPARISON OF HOT WIRE WITH LDV.

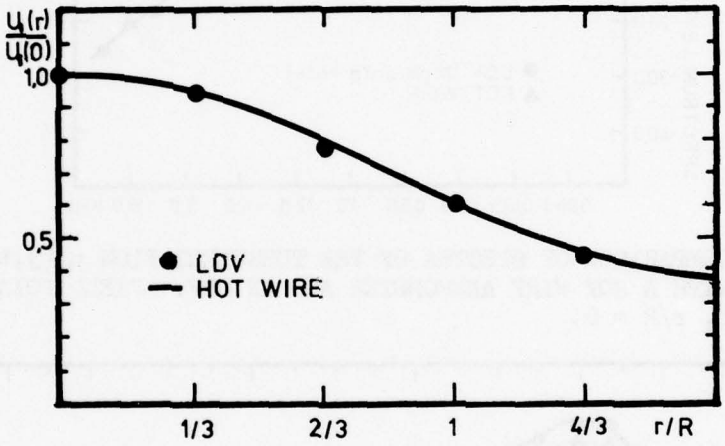


FIG. 4.15 MEAN VELOCITY PROFILE OF THE JET FLOW AT $y_1/D = 6$: COMPARISON OF HOT WIRE WITH LDV.

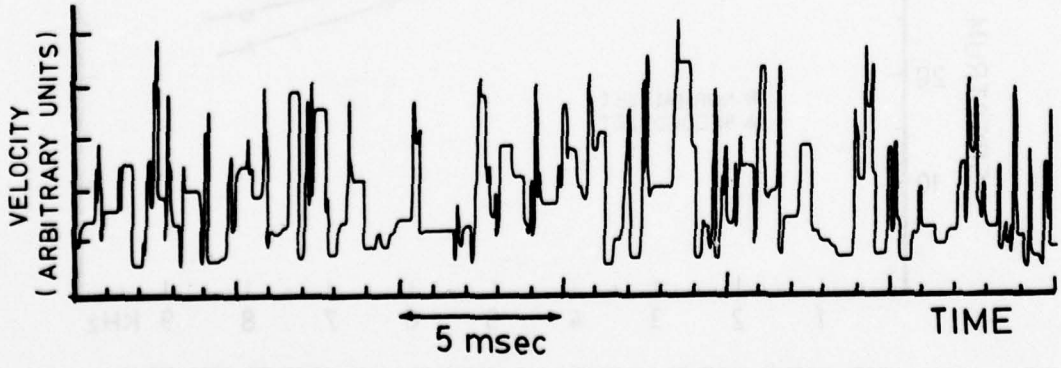


FIG. 4.16 TYPICAL OUTPUT OF THE LDV PROCESSOR. THE LAST VALID MEASUREMENT IS DISPLAYED UNTIL IT IS UPDATED BY A NEW ONE.

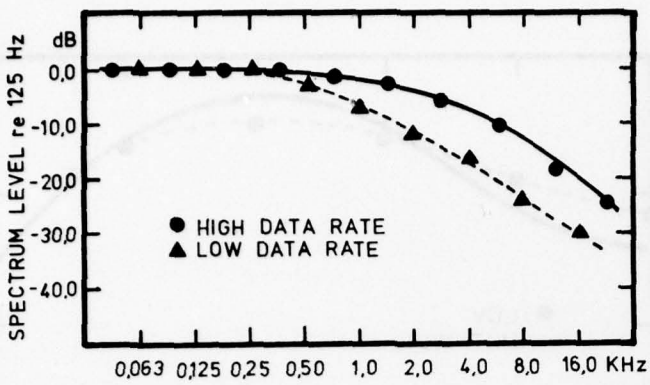


FIG. 4.17 EFFECT OF THE LDV DATA RATE ON THE ESTIMATE OF THE SPECTRUM OF THE TURBULENT FLOW $u_1(y,t)$; $y_1/D = 6$; $r/R = 0$.

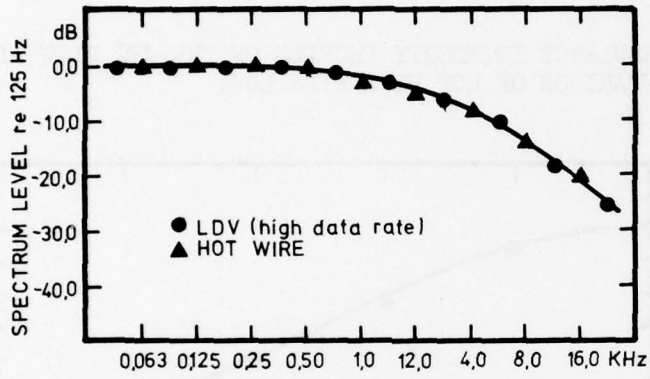


FIG. 4.18 COMPARISON OF SPECTRA OF THE TURBULENT FLOW $u_1(y,t)$ MEASURED WITH A HOT WIRE ANEMOMETER AND AN LDV. FIELD POINT: $y_1/D = 6$, $r/R = 0$.

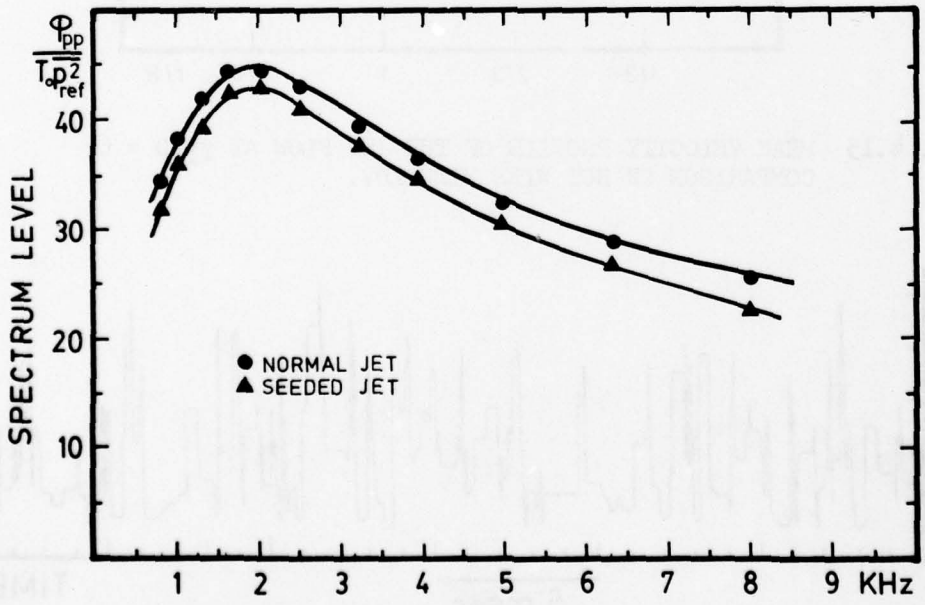


FIG. 4.19 FAR FIELD NOISE SPECTRA OF NORMAL AND SEEDED JET FLOW. THE SEEDED FLOW CONTAINS SMALL WATER DROPLETS ($\sim \mu m$). THE ADDITIONAL MASS RESULTS IN A VELOCITY DEFECT AND HENCE A REDUCTION IN SPECTRUM LEVEL.

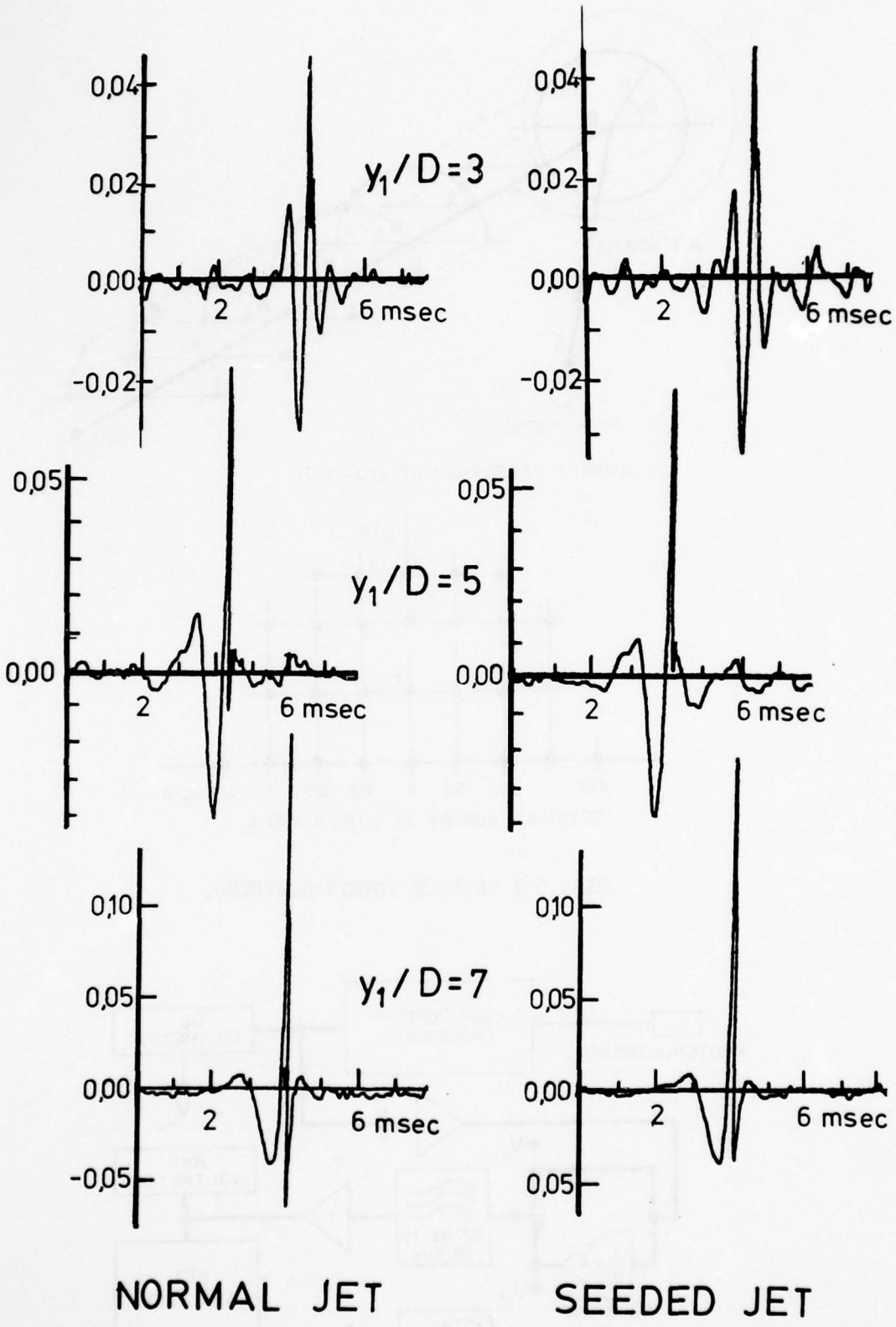
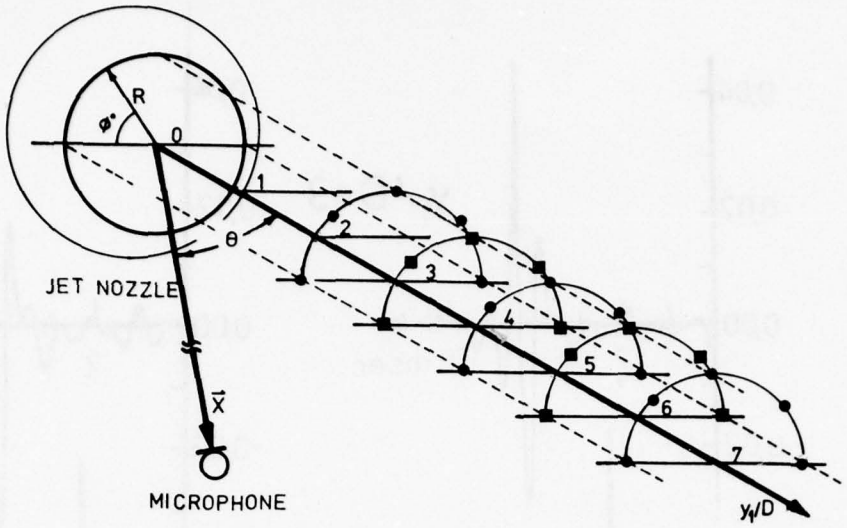
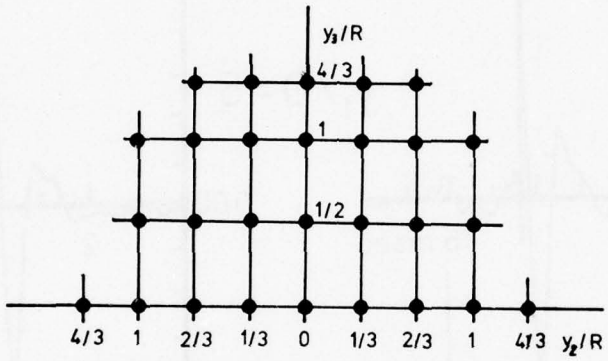


FIG. 4.20 COMPARISON OF NORMALIZED CROSS-CORRELATIONS OF NEAR AND FAR FIELD ACOUSTIC PRESSURES FOR SEEDED AND UNSEEDED JET FLOW.



SURVEY PERFORMED AT $y_1/D = 3$ TO 7



DETAILED SURVEY AT $y/D = 3$ AND 6

FIG. 5.1 SOURCE POINTS SURVEYED.

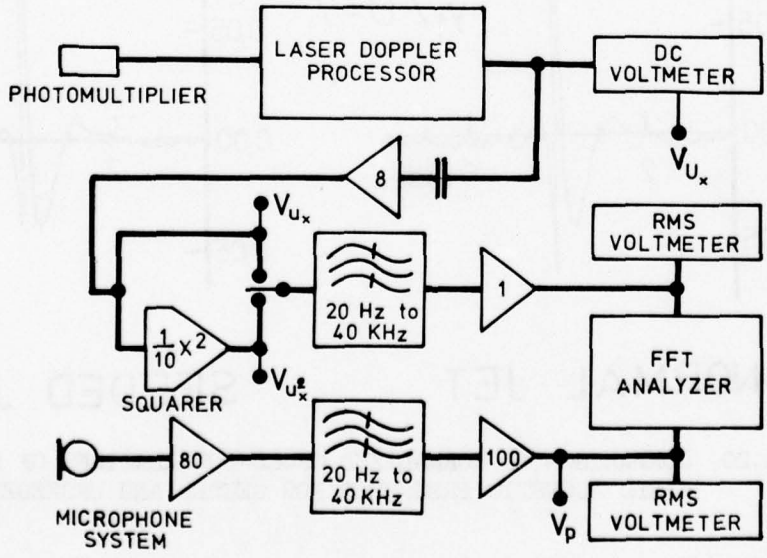


FIG. 5.2 SIGNAL PROCESSING SCHEMATIC.

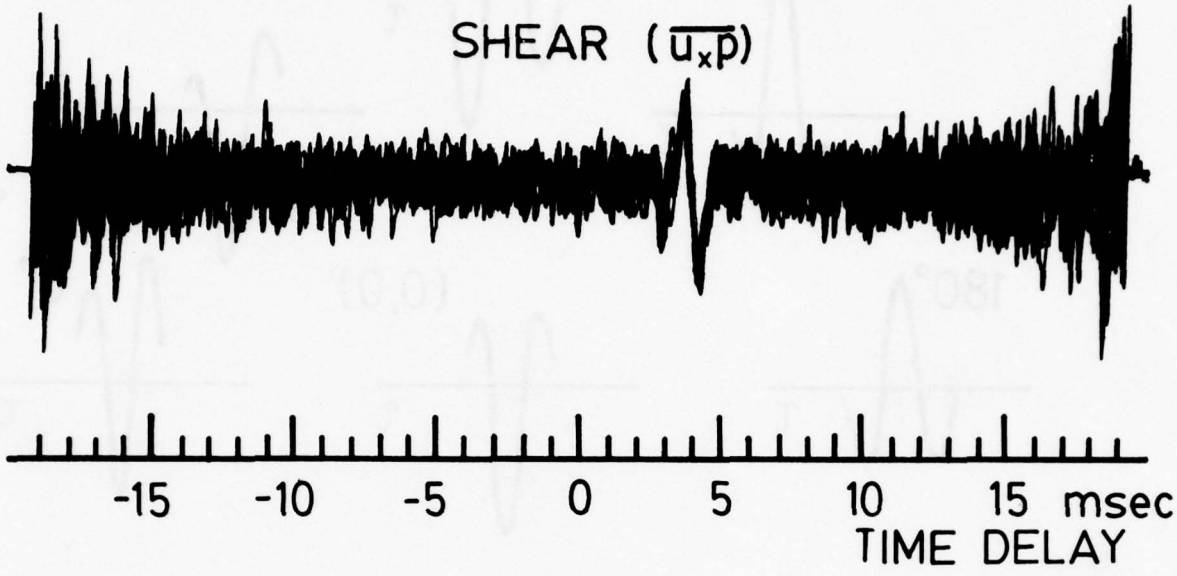


FIG. 6.1 MEASURED CROSS-CORRELATION OF THE INSTANTANEOUS TURBULENT FLOW $u_x(\underset{\rightarrow}{y}, t)$ AND THE FAR FIELD JET NOISE $p(\underset{\rightarrow}{x}, t)$. SOURCE POSITION: $y_1/D = 6$, $r/R = 0$.

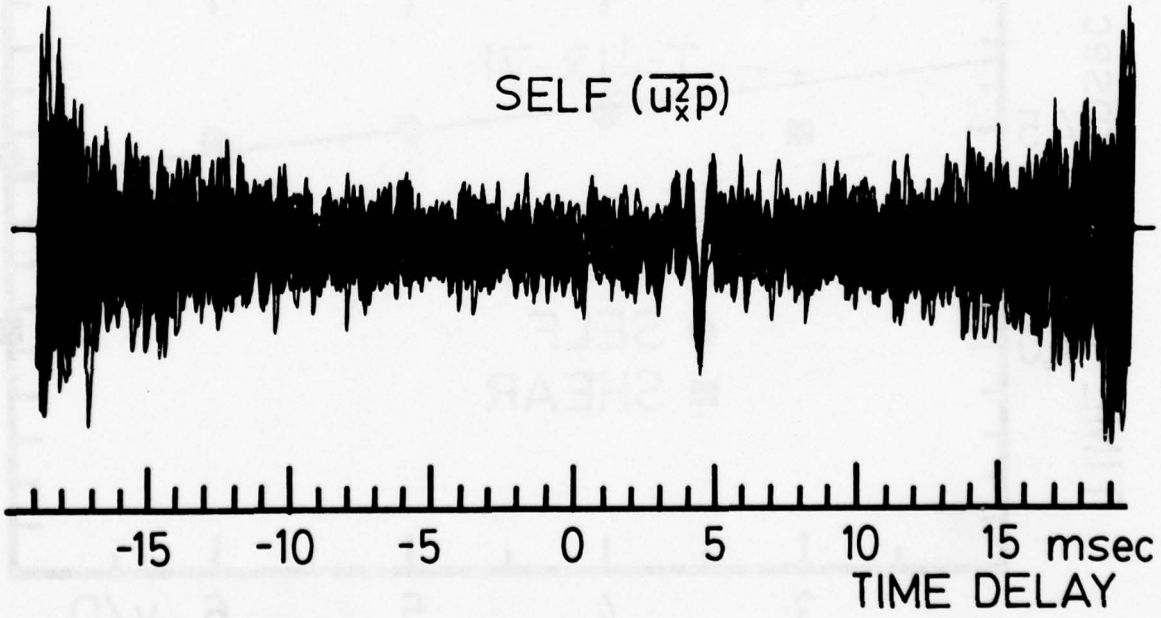


FIG. 6.2 MEASURED CROSS-CORRELATIONS OF THE SQUARE OF THE INSTANTANEOUS FLOW $u_x^2(\underset{\rightarrow}{y}, t)$ AND THE FAR FIELD JET NOISE $p(\underset{\rightarrow}{x}, t)$. SOURCE POSITION $y_1/D = 6$, $r/R = 0$.

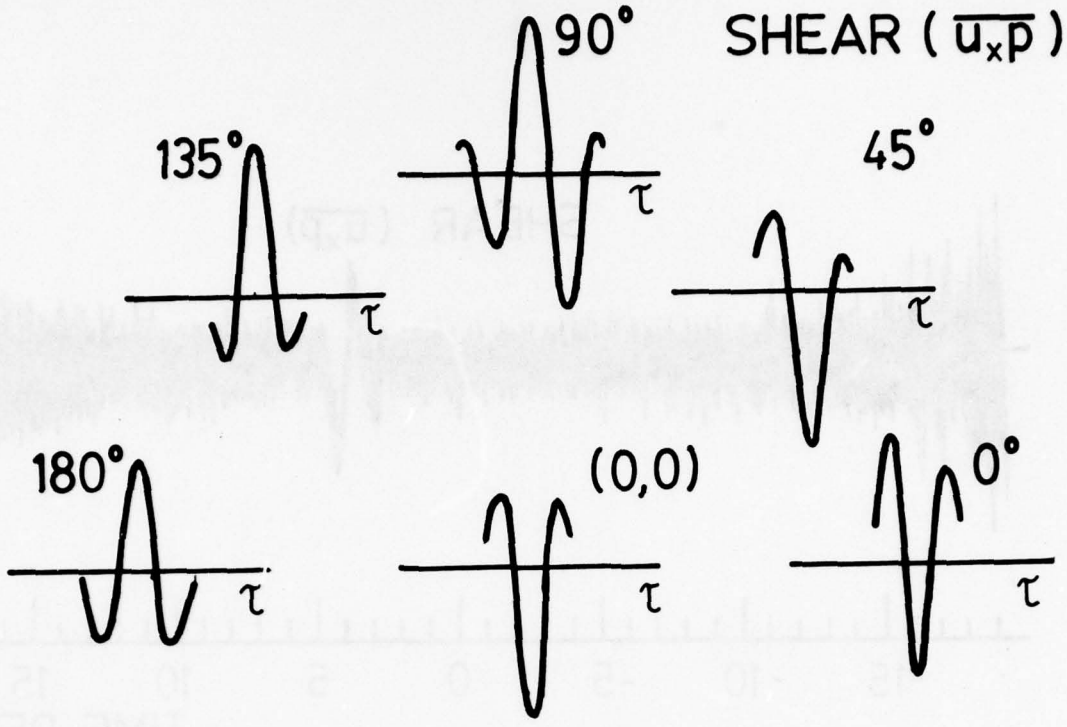


FIG. 6.3 ILLUSTRATION OF THE BEHAVIOUR OF THE 'SHEAR NOISE CORRELATION' $R_{u_x p}(\underset{\rightarrow}{x}, \underset{\rightarrow}{y}, \tau)$ AT $y_1/D = 6$.

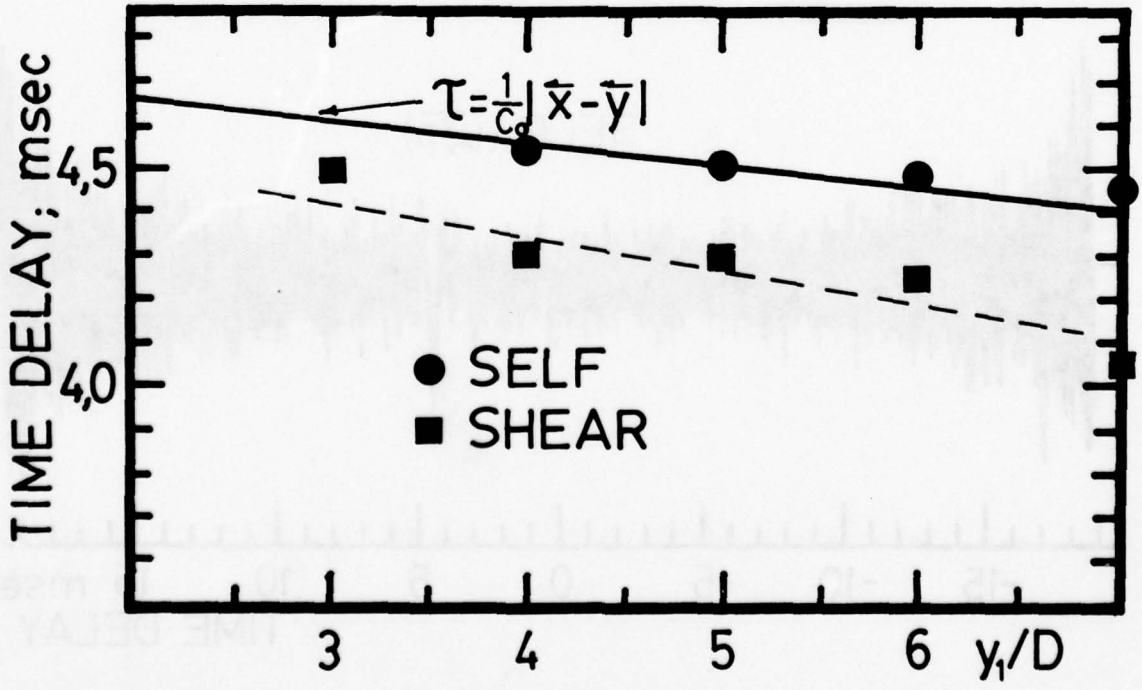


FIG. 6.4 TIME DELAY OF THE PEAK VALUES OF THE CROSS-CORRELATION $R_{u_x p}(\underset{\rightarrow}{x}, \underset{\rightarrow}{y}, \tau)$ (SHEAR) AND $R_{u_x 2p}(\underset{\rightarrow}{x}, \underset{\rightarrow}{y}, \tau)$ (SELF).

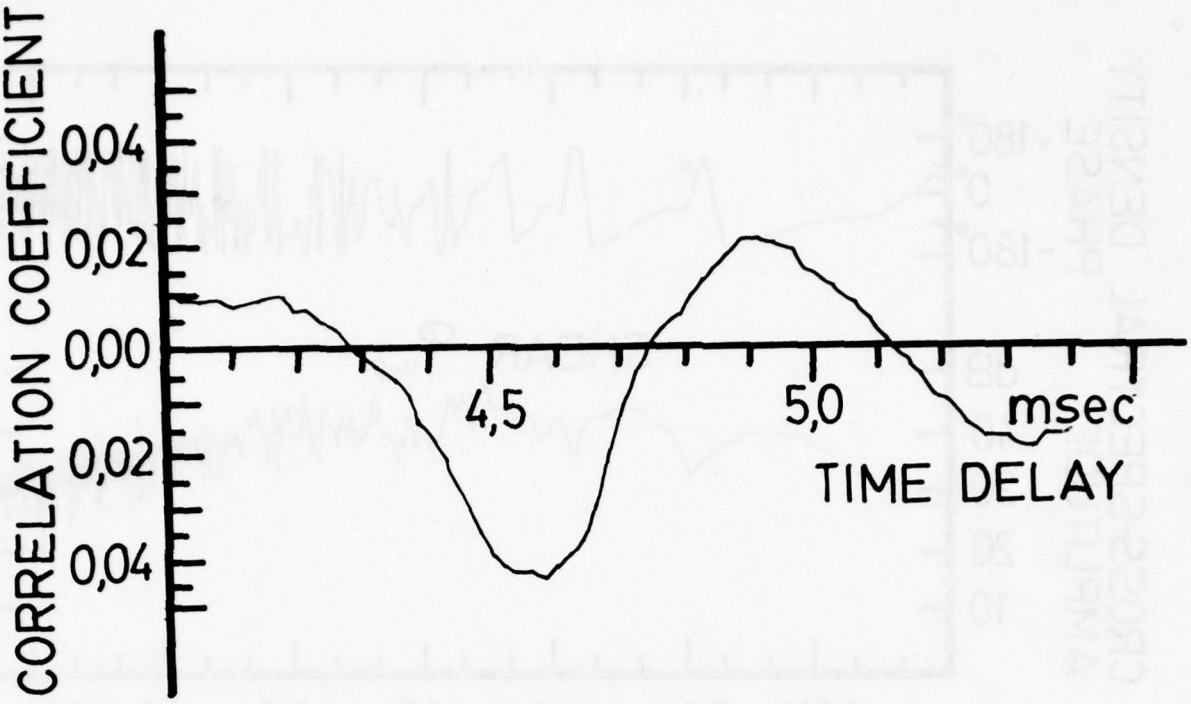


FIG. 6.5 NORMALIZED 'SHEAR NOISE CORRELATION' $R_{u_x p}(\underline{x}, \underline{y}, \tau)/\sqrt{\overline{u_x^2}(\underline{y})\overline{p^2}(\underline{x})}$ MEASURED WITH A HOT WIRE ANEMOMETER. SOURCE POSITION: $y_1/D = 6$, $r/R = 1$, $\phi = 0$.

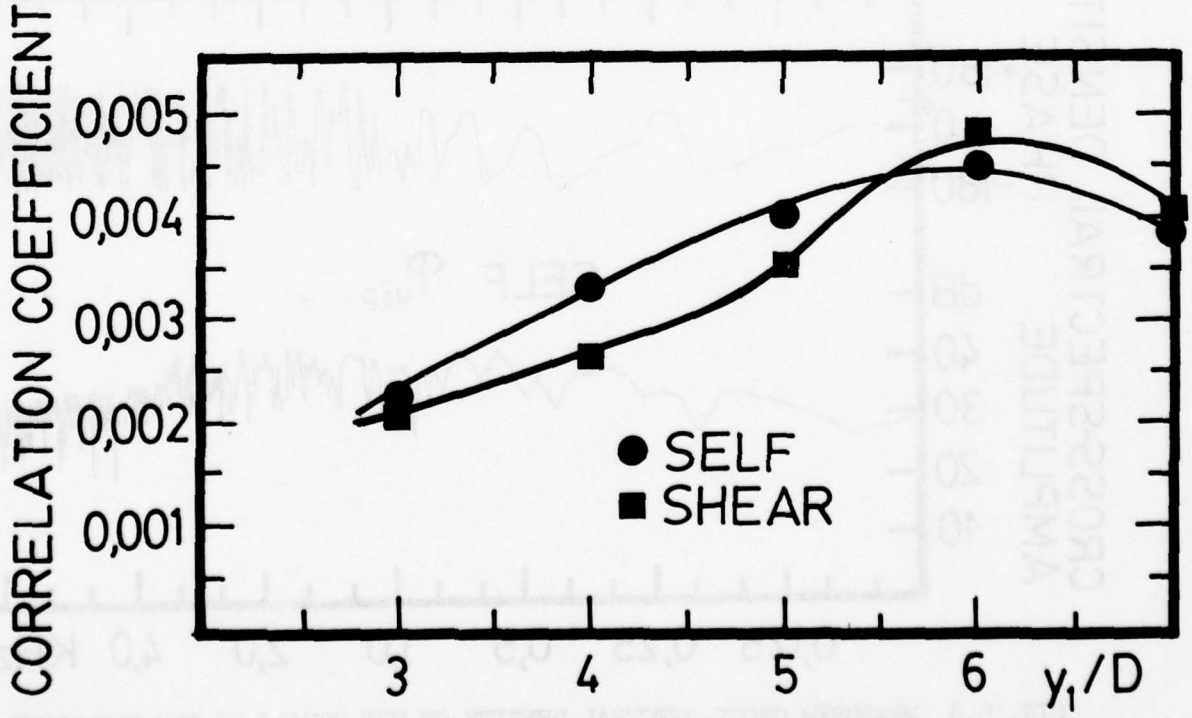


FIG. 6.6 NORMALIZED CROSS-CORRELATION COEFFICIENTS AS A FUNCTION OF AXIAL POSITION. ALL SOURCE POINTS ARE LOCATED ON THE LOCUS $r/R = 1$, $\phi = 0°$.

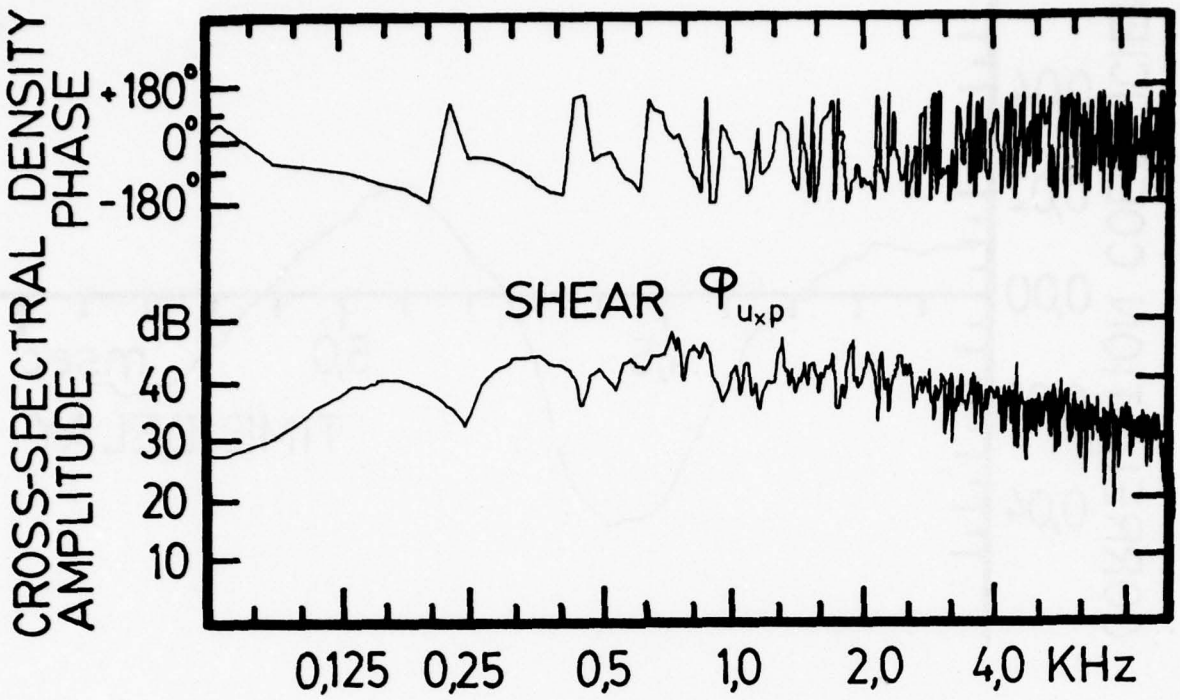


FIG. 6.7 MEASURED CROSS-SPECTRAL DENSITY OF THE TURBULENT FLOW $u_x(\underset{\sim}{y}, t)$ AND $p(\underset{\sim}{x}, t)$. SOURCE POINT $y_1/D = 6$, $r/R = 1$, $\phi = 135°$; OBSERVER IS AT 40° TO THE JET AXIS.

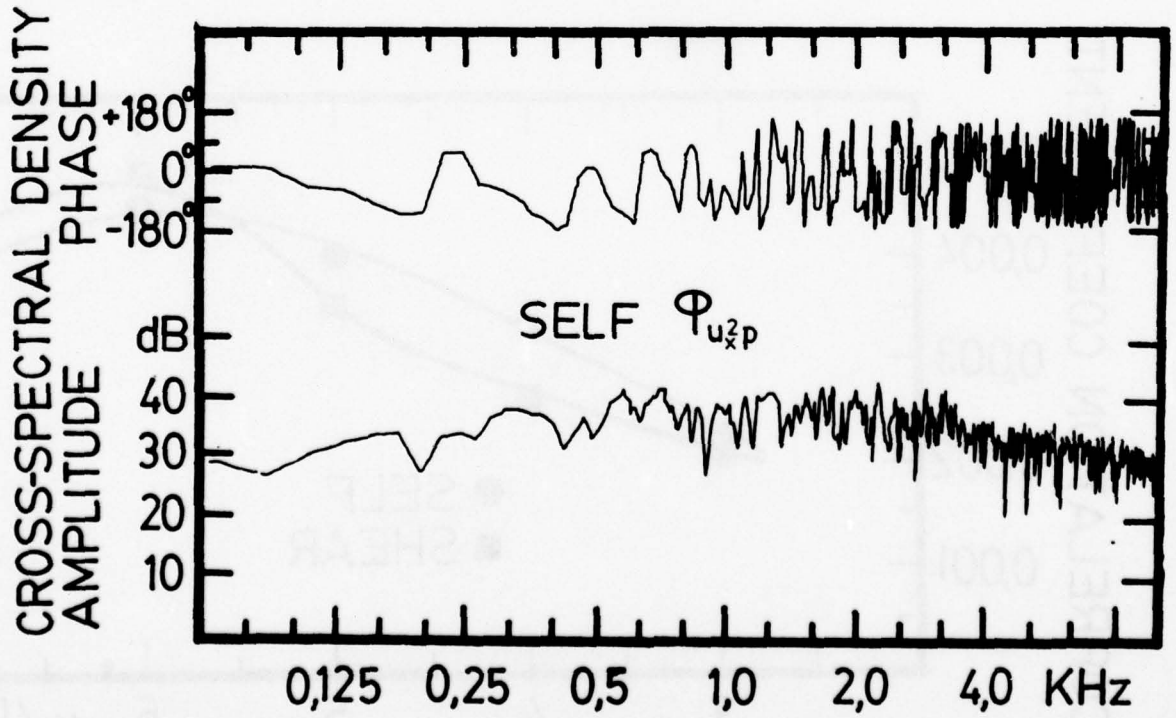


FIG. 6.8 MEASURED CROSS-SPECTRAL DENSITY OF THE SQUARE OF THE TURBULENT FLOW $u_x^2(\underset{\sim}{y}, t)$ AND $p(\underset{\sim}{x}, t)$. SOURCE POINT $y_1/D = 6$, $r/R = 1$, $\phi = 135°$; OBSERVER IS AT 40° TO THE JET AXIS.

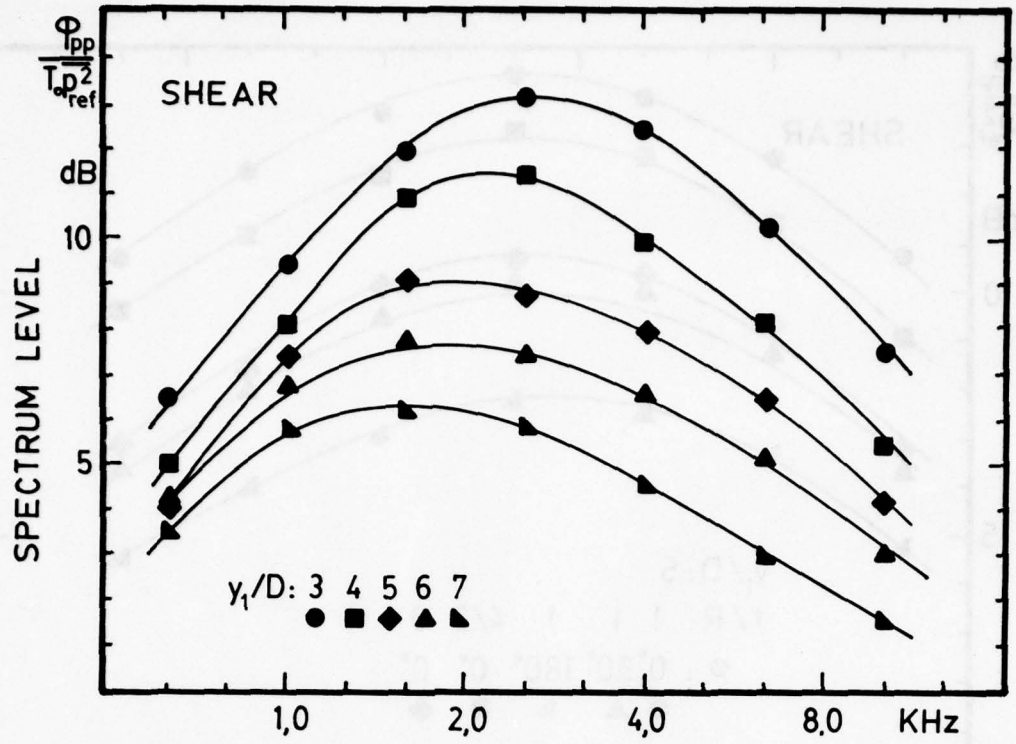


FIG. 6.9 RELATIVE CONTRIBUTION TO THE SHEAR NOISE SPECTRUM FROM A UNIT VOLUME OF JET. SOURCE POINTS ARE LOCATED ALONG THE LINE $r/R = 1$, $\phi = 0°$.

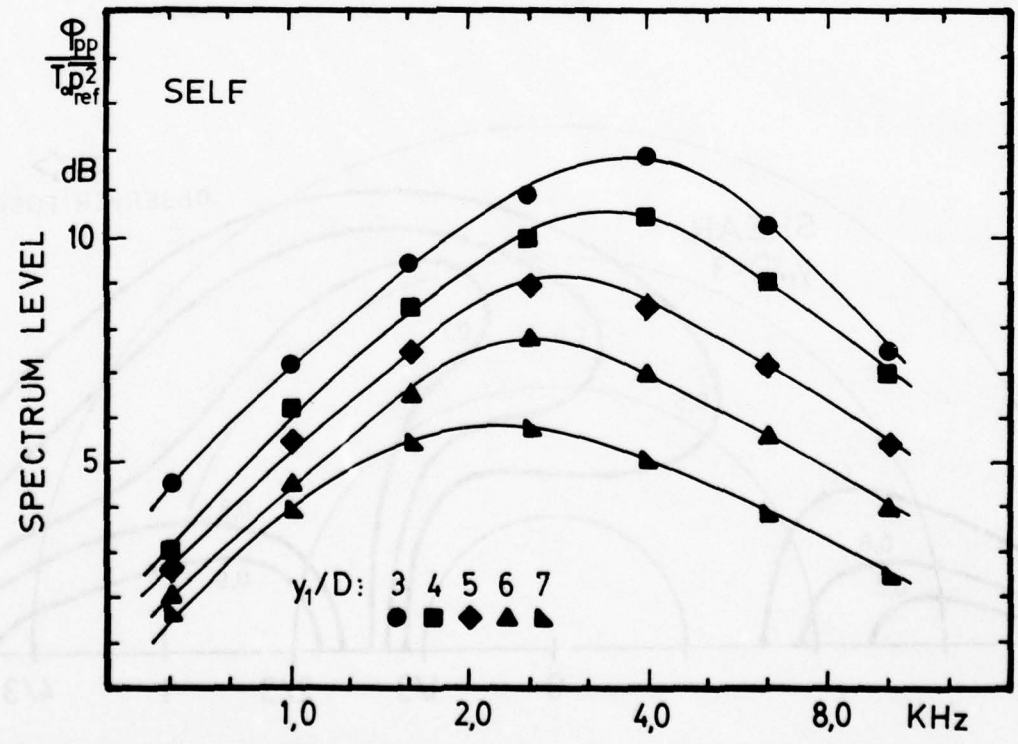


FIG. 6.10 RELATIVE CONTRIBUTION TO THE SELF NOISE SPECTRUM FROM A UNIT VOLUME OF JET. SOURCE POINTS ARE LOCATED ALONG THE LINE $r/R = 1$, $\phi = 0°$.

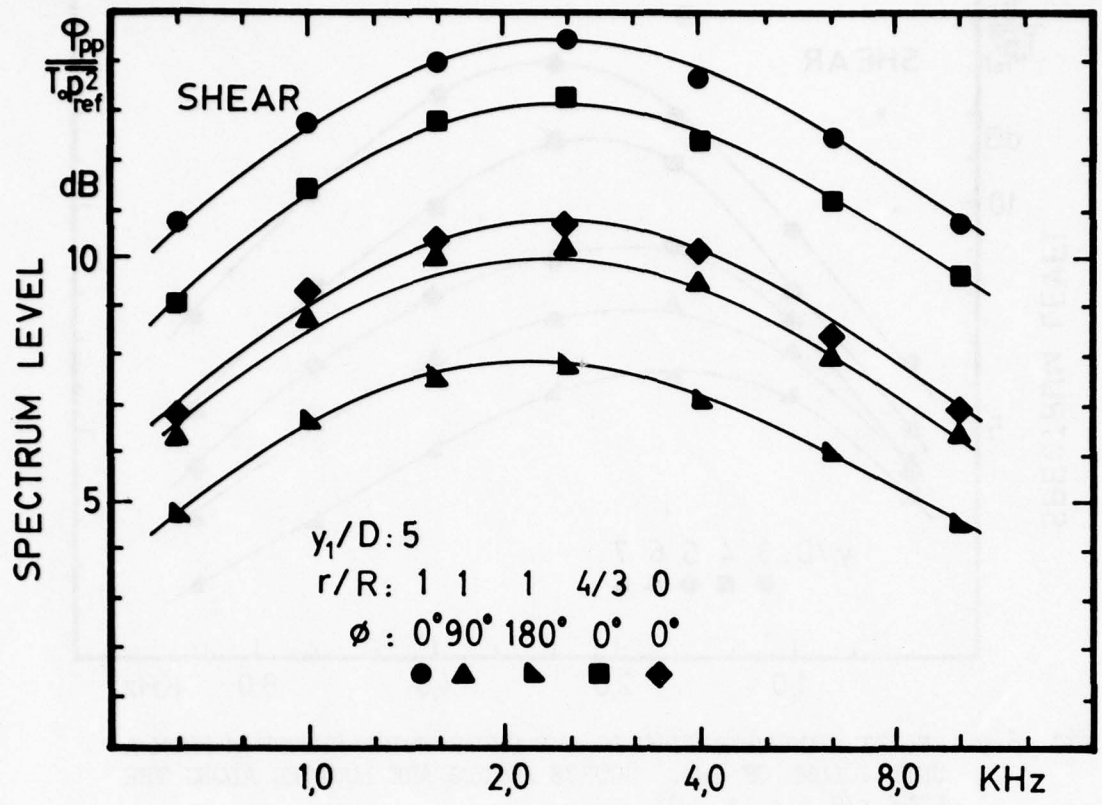


FIG. 6.11 RELATIVE CONTRIBUTION TO THE SHEAR NOISE SPECTRUM FROM A UNIT VOLUME OF JET. SOURCE POINTS ARE LOCATED OVER A CROSS-SECTION AT $y_1/D = 5$.

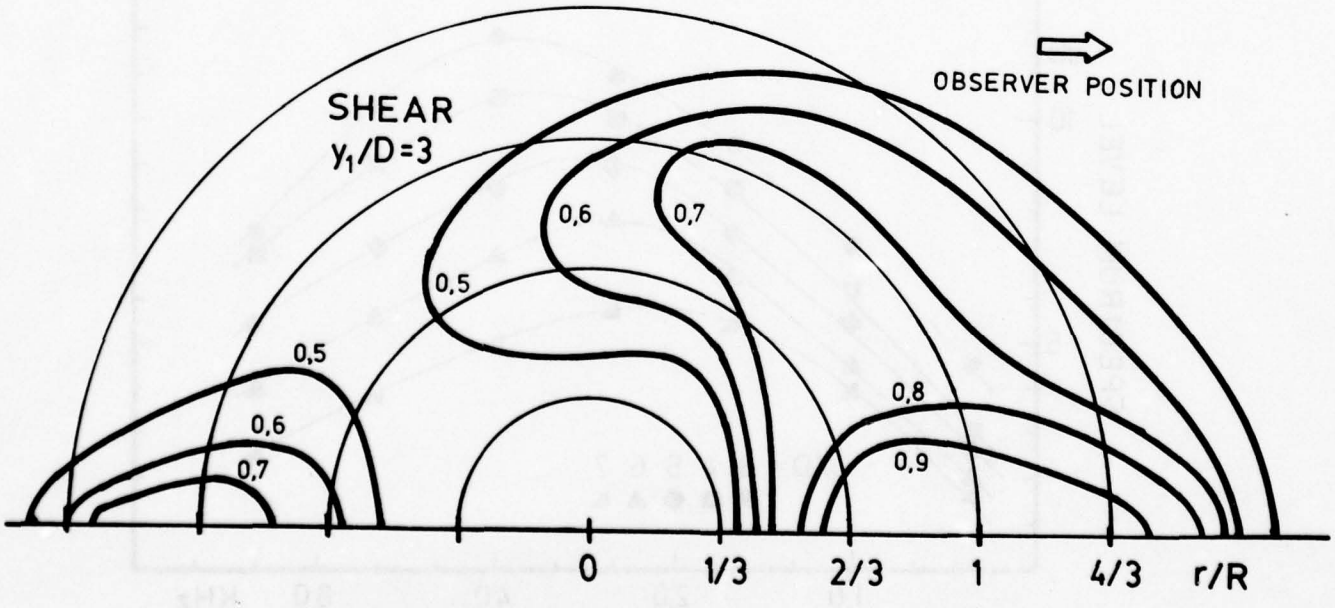


FIG. 6.12 CONTOURS OF EQUAL RELATIVE CONTRIBUTION FROM UNIT VOLUME TO THE OVERALL SHEAR NOISE FOR A SLICE OF JET AT $y_1/D = 3$ NORMALIZED BY THE CONTRIBUTION FROM $y_1/D = 3$, $r/R = 1$, $\phi = 0°$; OBSERVER IS AT 40° TO THE JET AXIS.

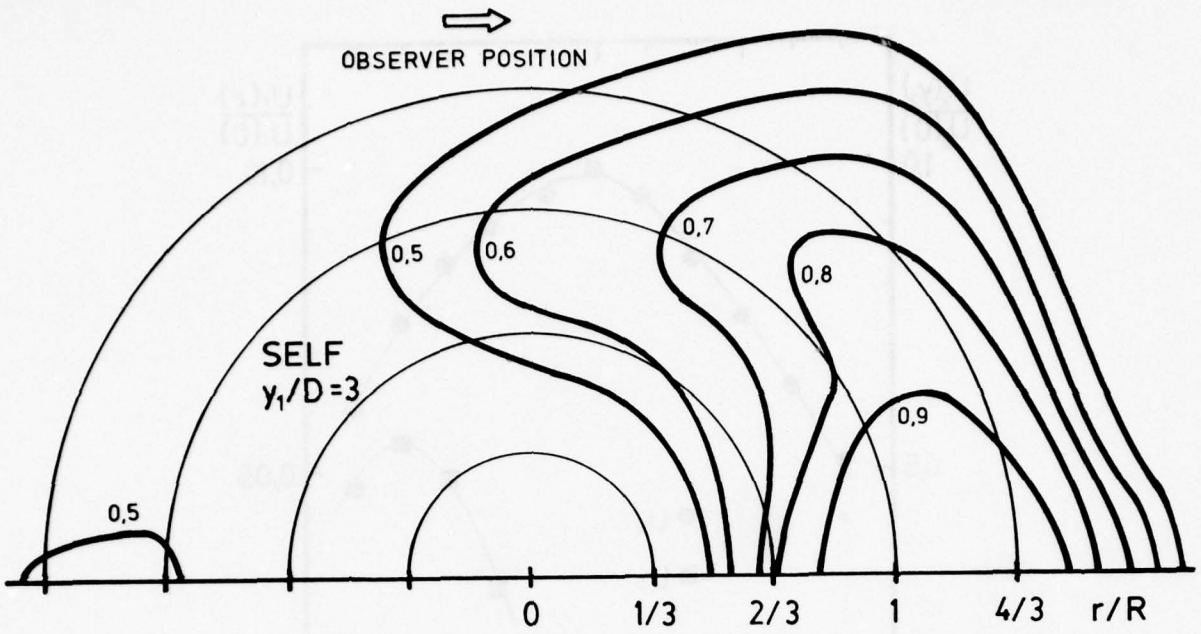
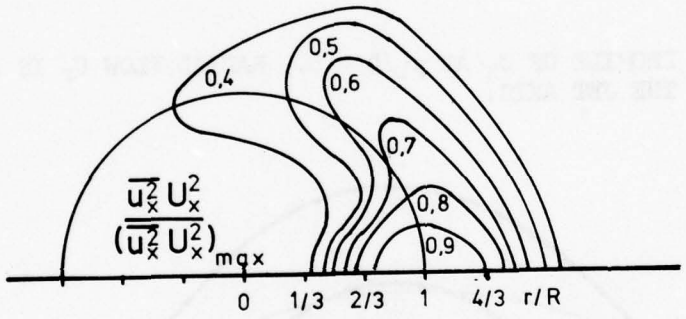


FIG. 6.13 CONTOURS OF EQUAL RELATIVE CONTRIBUTION PER UNIT VOLUME TO THE OVERALL SELF NOISE FOR A SLICE OF JET AT $y_1/D = 3$ NORMALIZED BY THE CONTRIBUTION FROM $y_1/D = 3$, $r/R = 1$, $\phi = 0°$; OBSERVER IS AT 40° TO THE JET AXIS.



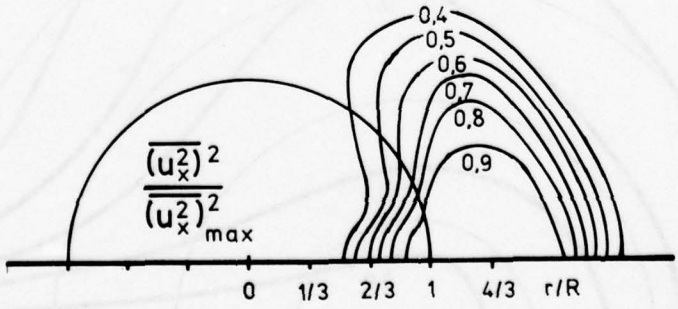


FIG. 6.14 NOMINAL SOURCE PATTERNS ($\bar{u}_x^2 U_x^2$ ~ SHEAR; $\overline{(u_x^2)^2}$ ~ SELF) AT $y_1/D = 3$. THE MAXIMA ARE FOUND IN THE NEIGHBOURHOOD OF $r/R = 1$, $\phi = 0°$. THE VELOCITY COMPONENTS IN THE $\vec{x}$ DIRECTION (40° TO THE JET AXIS) HAVE BEEN MEASURED.

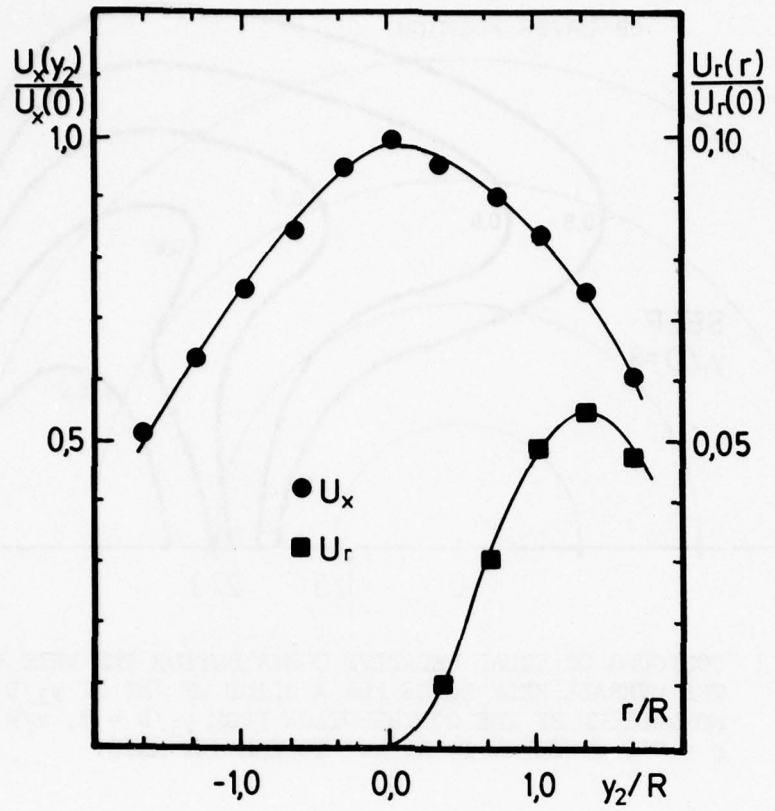


FIG. 6.15 PROFILE OF U_x AT $y_1/D = 6$. RADIAL FLOW U_r IS AWAY FROM THE JET AXIS.

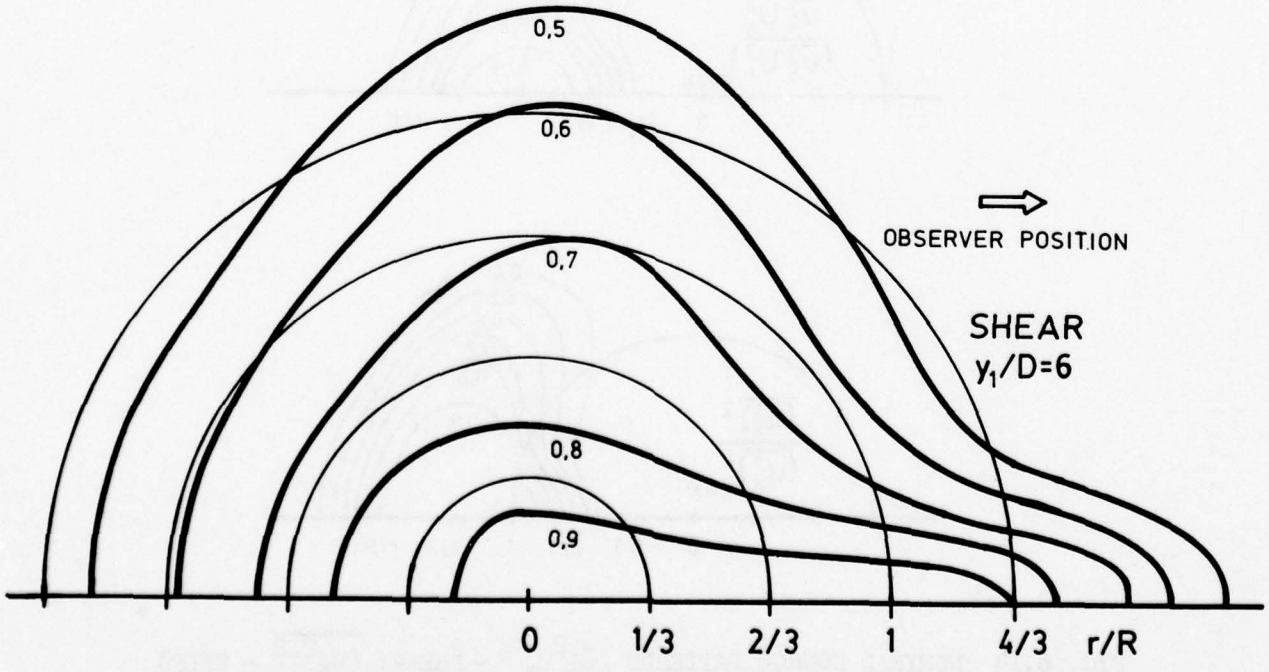


FIG. 6.16 CONTOURS OF EQUAL RELATIVE CONTRIBUTION PER UNIT VOLUME TO THE OVERALL SHEAR NOISE FOR A SLICE OF JET AT $y_1/D = 6$ NORMALIZED BY THE CONTRIBUTION FROM $y_1/D = 6$, $r/R = 1$, $\phi = 0°$; OBSERVER IS AT 40° TO THE JET AXIS.

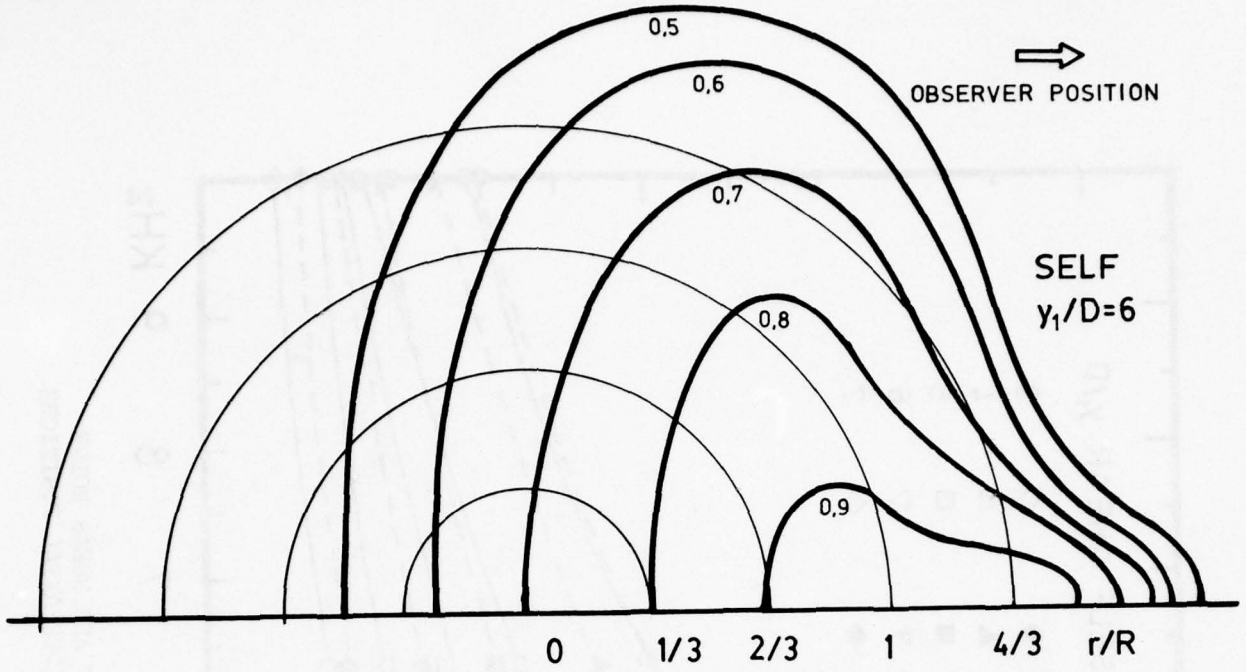
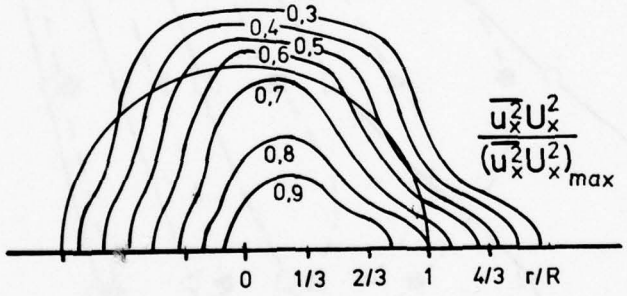


FIG. 6.17 CONTOURS OF EQUAL RELATIVE CONTRIBUT ION PER UNIT VOLUME TO THE OVERALL SELF NOISE FOR A SLICE OF JET AT $y_1/D = 6$, $r/R = 1$, $\phi = 0°$; OBSERVER IS AT 40° TO THE JET AXIS.



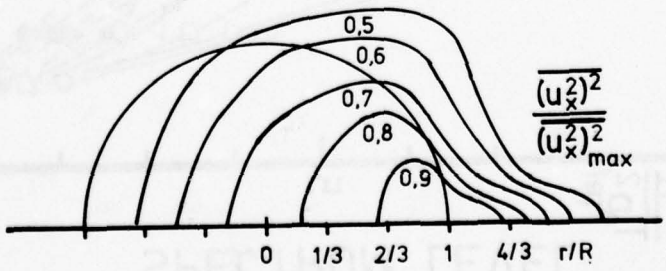


FIG. 6.18 NOMINAL SOURCE PATTERNS ($\overline{u_x^2 U_x^2}$ ~ SHEAR; $\overline{(u_x^2)^2}$ ~ SELF) AT $y_1/D = 6$. THE MAXIMA ARE FOUND IN THE NEIGHBOURHOOD OF $r/R = 1$, $\phi = 0°$. THE VELOCITY COMPONENTS IN THE $\underrightarrow{x}$ DIRECTION (40° TO THE JET AXIS) HAVE BEEN MEASURED.

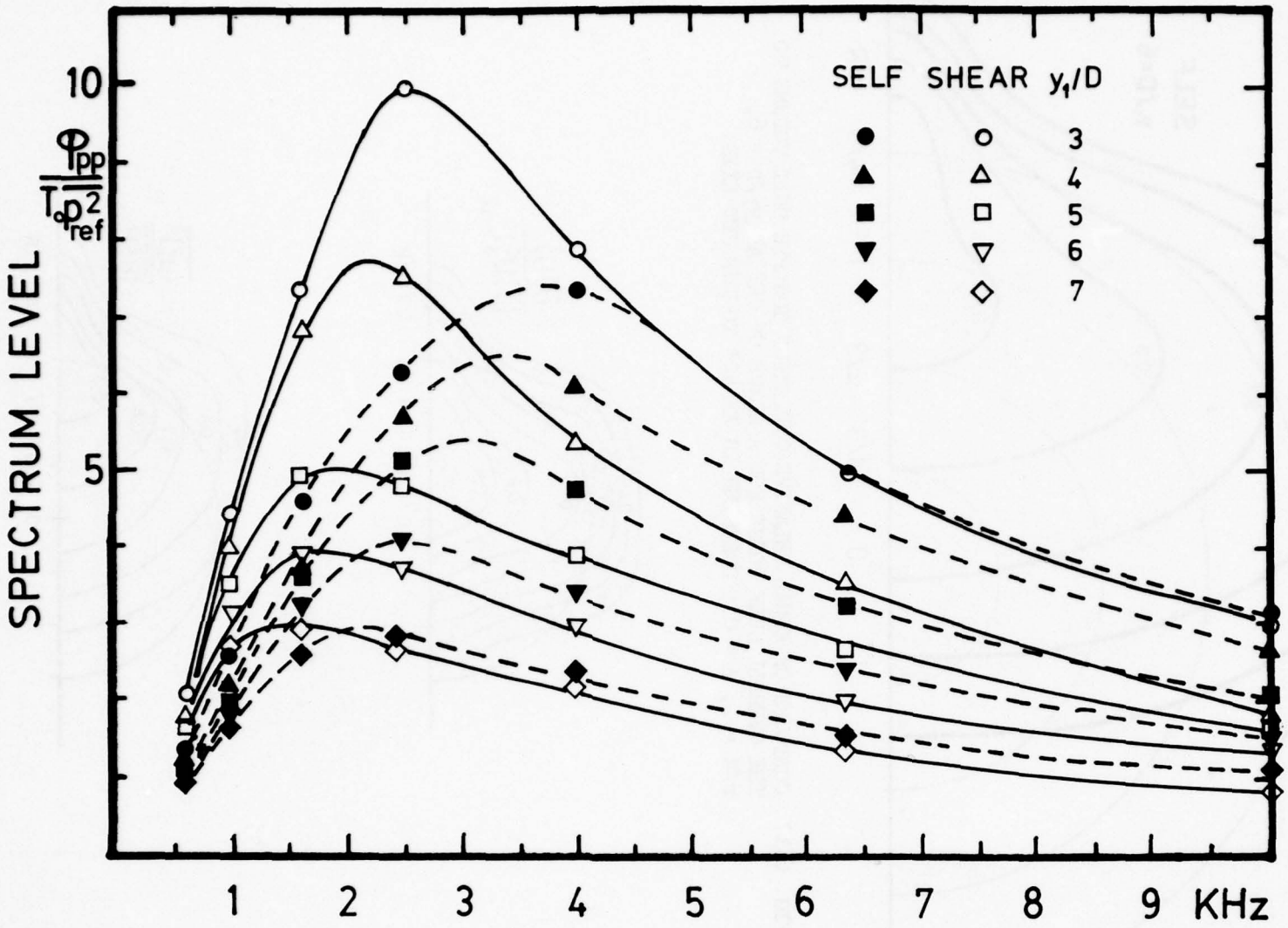


FIG. 6.19 CONTRIBUTIONS TO THE FAR-FIELD SELF AND SHEAR NOISE SPECTRA FROM A SLICE OF JET AT VARIOUS AXIAL POSITIONS.

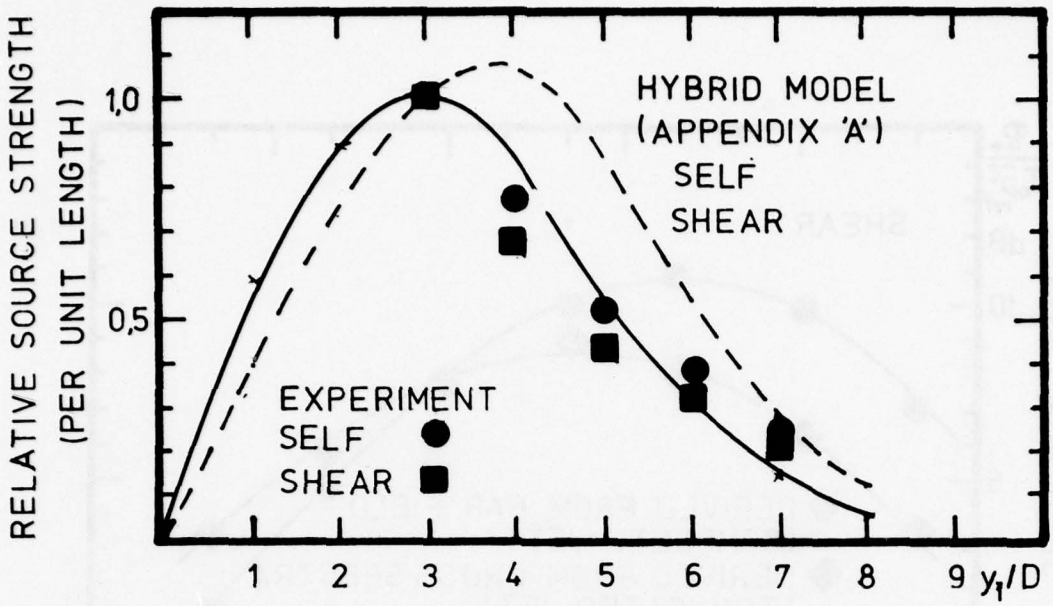


FIG. 6.20 RELATIVE OVERALL SELF AND SHEAR NOISE SOURCE STRENGTHS PER UNIT LENGTH AS A FUNCTION OF AXIAL POSITION; COMPARISON OF EXPERIMENT AND A HYBRID MODEL PROPOSED IN APPENDIX A. THE DATA HAS BEEN NORMALIZED BY THE RESPECTIVE VALUES AT $y_1/D = 3$.

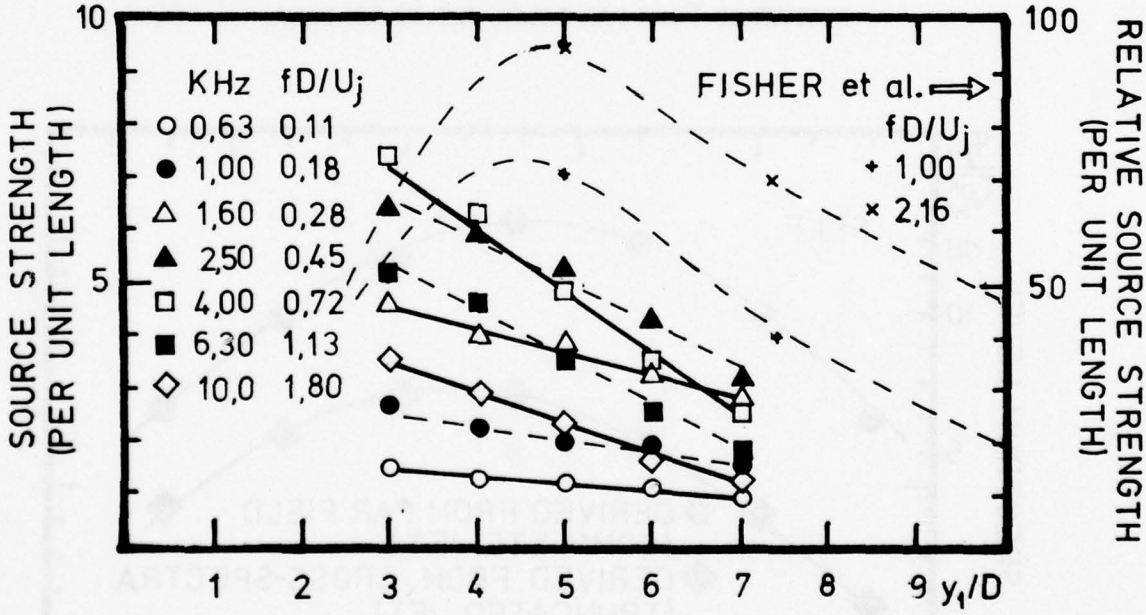


FIG. 6.21 ACOUSTIC SOURCE STRENGTH PER UNIT LENGTH AS A FUNCTION OF FREQUENCY AND AXIAL SOURCE POSITION. SOURCE STRENGTH DISTRIBUTIONS INFERRED FROM A POLAR CORRELATION SOURCE LOCATION TECHNIQUE (FISHER ET AL, REF. 75) ARE SHOWN FOR QUALITATIVE COMPARISON.

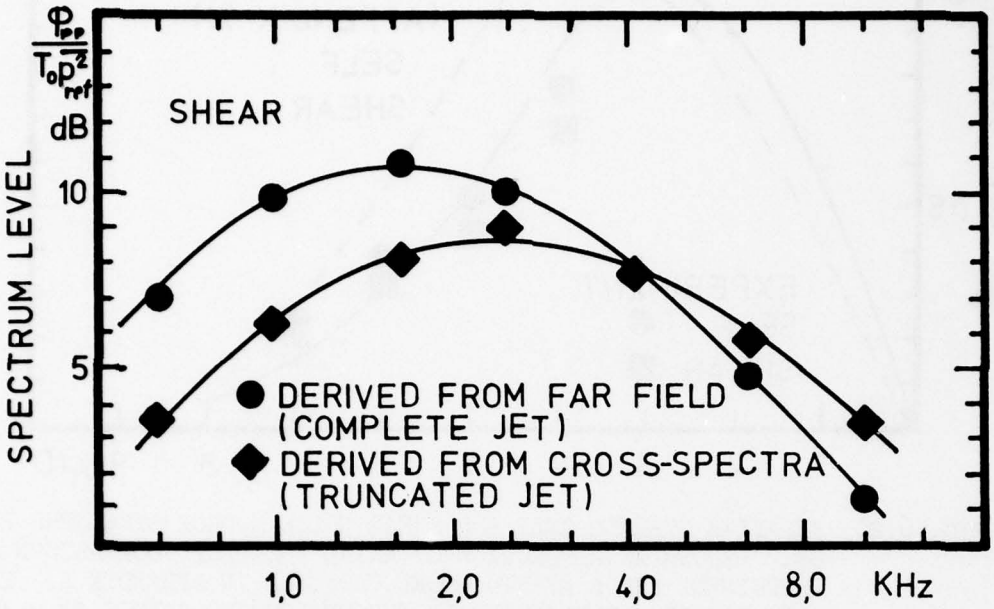


FIG. 6.22 COMPARISON OF THE FAR FIELD SHEAR NOISE SPECTRUM COMPUTED FROM CROSS SPECTRAL DENSITY MEASUREMENTS WITH THE ONE EXTRACTED FROM FAR FIELD JET NOISE DATA.

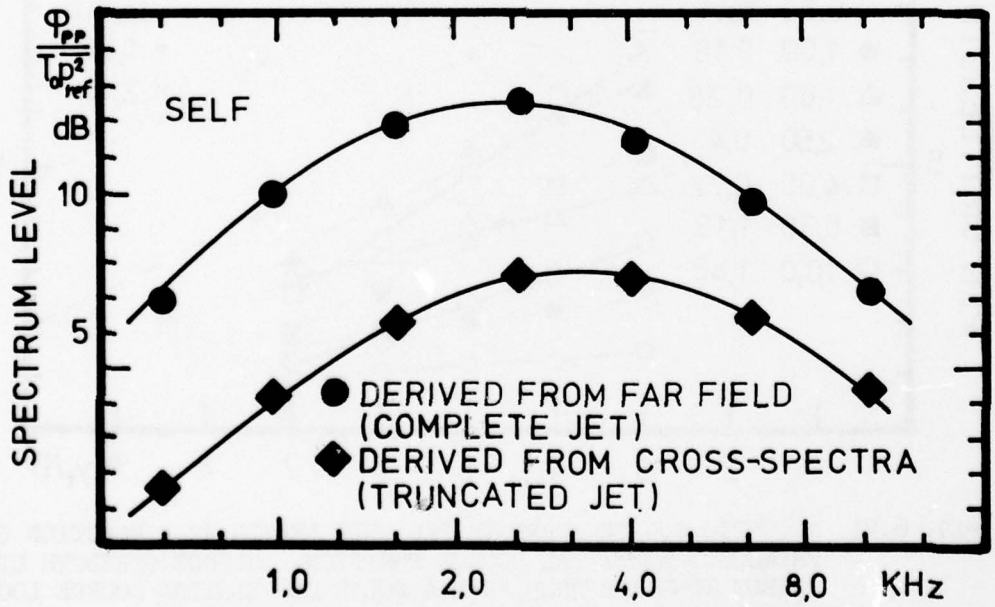


FIG. 6.23 COMPARISON OF THE FAR FIELD SELF NOISE SPECTRUM COMPUTED FROM CROSS-SPECTRAL DENSITY MEASUREMENTS WITH THE ONE EXTRACTED FROM FAR FIELD JET NOISE DATA.

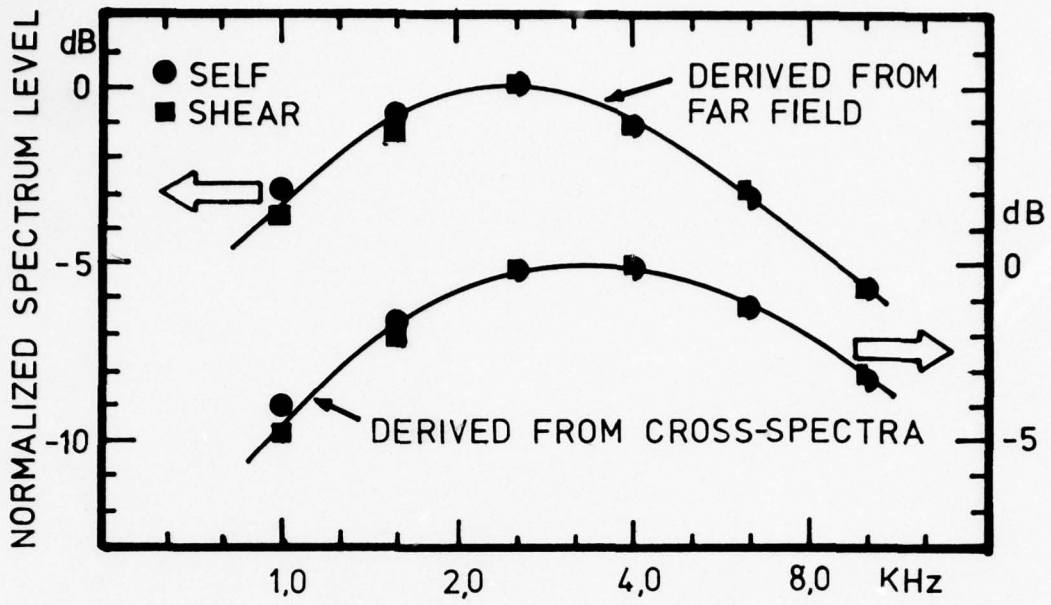


FIG. 6.24 TEST OF THE SIMILARITY OF THE PEAK NORMALIZED SELF AND SHEAR NOISE SPECTRA AFTER A FREQUENCY SHIFT: BOTH SHEAR NOISE SPECTRA HAVE BEEN SHIFTED IN FREQUENCY BY A FACTOR OF 1.6.

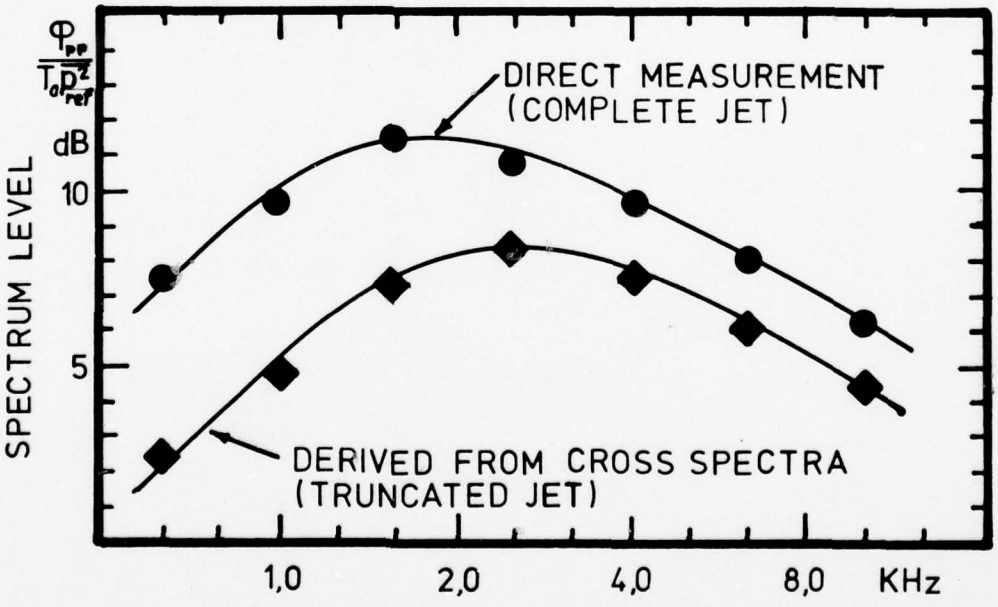


FIG. 6.25 OVERALL FAR FIELD JET NOISE SPECTRUM AT 40° TO THE JET AXIS: COMPARISON OF DIRECT MEASUREMENT WITH PREDICTION BASED ON CROSS-SPECTRAL DENSITY MEASUREMENTS.

APPENDIX A

A SIMPLE JET NOISE MODEL

Some properties of jet noise are computed from a simple turbulence-plus-mean flow model which is largely equivalent to that of Ribner (Ref. 10). The analytical approach follows along the lines of Pao and Lowson (Ref. 78). By transformation to the wave number-frequency space, some of the rather complex coordinate transformations (see, for example, Ribner UTIA Report 86, Ref. 6) are exchanged for more straightforward Fourier transforms.

The turbulence model that will be used to describe the two point velocity correlations in the jet satisfies the criterion of homogeneous isotropic turbulence (Batchelor, Ref. 79) convected by the local jet flow. The cross-correlation of the velocity $u_i(\underset{\rightarrow}{x},t)$ and $u_j(\underset{\rightarrow}{y}+\underset{\rightarrow}{\xi}, t-\tau)$ defined in a reference frame moving at the convection velocity U_c is modelled as:

$$\overline{u_i(\underset{\rightarrow}{y},t)u_j(\underset{\rightarrow}{y}+\underset{\rightarrow}{\xi}, t-\tau)} = u_1^2(\underset{\rightarrow}{y}) \left\{\delta_{ij}(1-a^2|\underset{\rightarrow}{\xi}|^2) + a^2\xi_i\xi_j\right\} e^{-a^2(|\underset{\rightarrow}{\xi}|^2 + \alpha^2 U_c^2 \tau^2)} \tag{A1}$$

The parameters a, α, and U_c are weak functions of position and determine the spatial and temporal scales of the correlation. For convenience these parameters are treated as being constant within a correlation volume. The turbulence model is identical to the one discussed by Pao and Lowson (Ref. 78); extensive use of such a model was also made in earlier work by Lilley (Ref. 5) and Ribner (Ref. 10). The Gaussian was chosen for its well behaved Fourier transform; even after repeated differentiation one does not encounter convergence problems. Mathematical expediency has dictated the choice of the model correlation; consequently, the turbulence, which is neither isotropic nor homogeneous, is not described with great accuracy.

The model cross-correlations and cross-spectral densities relevant to Ribner's self and shear noise formalism take the form:

$$\overline{u_x u_x'}(\underset{\rightarrow}{y},\underset{\rightarrow}{\xi},\tau) = \overline{u_1^2(\underset{\rightarrow}{y})} \left(1-a^2\xi_3^2 - a^2(\xi_2\cos\theta-\xi_1\sin\theta)^2\right) e^{-a^2(|\underset{\rightarrow}{\xi}|^2 + \alpha^2 U_c^2 \tau^2)} \tag{A2}$$

$$\overline{u_x^2 u_x'^2}(\underset{\rightarrow}{y},\underset{\rightarrow}{\xi},\tau) = 2(\overline{u_x u_x'})^2 + (\overline{u_x^2})^2 \tag{A3}$$

u_x is the velocity in the x direction (the observer is located at $\underset{\rightarrow}{x}$), $\underset{\rightarrow}{\xi}$ the separation between field points in the turbulent flow, and τ is the time delay. As the source term of the jet noise is proportional to $\partial^2/\partial t^2\ (u_x + U_x)^2$, only $2(u_x u_x')^2$ in Eq. A3 will contribute to the jet noise correlation, $(\overline{u_x^2})^2$ being invariant with respect to τ.

The cross-spectra in wave-number-frequency space are given by the respective four dimensional Fourier transforms as:

$$\Phi_{u_x u_x}(\underset{\rightarrow}{y},\underset{\rightarrow}{k},\omega) = \frac{\overline{u_1^2}(\underset{\rightarrow}{y})}{16a^4\alpha U_c \pi^2} \frac{k_3^2 + (k_2\cos\theta - k_1\sin\theta)^2}{4a^2} e^{-\frac{1}{4a^2}\left(|\underset{\rightarrow}{k}|^2 + \frac{\omega^2}{\alpha^2 U_c^2}\right)} \tag{A4}$$

$$\Phi_{u_x^2 u_x^2}(\underset{\rightarrow}{y},\underset{\rightarrow}{k},\omega) = \frac{[\overline{u_x^2}(y)]^2}{32a^4\alpha U_c \pi^2} \left\{\frac{1}{2} + \left(\frac{k_3^2 + (k_2\cos\theta - k_1\sin\theta)^2}{16a^2}\right)^2\right\} e^{-\frac{1}{8a^2}\left(|\underset{\rightarrow}{k}|^2 + \frac{\omega^2}{\alpha^2 U_c^2}\right)} \tag{A5}$$

$\underset{\rightarrow}{k}$ and ω are the wave number vector and the radian frequency respectively.

The mean velocity profile is modelled as:

$$U_o = U_1(y_1) e^{-c^2(y_2^2 + y_3^2)} \tag{A6}$$

with c and U_1 slowly varying functions of axial position y_1. The mean velocity component in the direction of an observer at $\underset{\rightarrow}{x}$ is:

$$U_x = U_o \cos\theta \tag{A7}$$

The Gaussian is a reasonable description of the mean velocity profile in the transition region and the fully developed jet; however, it fails to model the flow near the jet nozzle (mixing region) with sufficient accuracy. A better model of the mean velocity profile in the mixing region would have been (Ref. 80):

$$U = U_s \frac{A}{2\pi} \int_{\xi}^{\infty} e^{-\frac{A}{2}(s - \xi_o)^2} ds \tag{A8}$$

Lilley (Ref. 5) suggests $A \approx 300$ and $\xi_o \approx .03$. Ribner (Ref. 10) models the two-point correlation as

$$U\left(\underset{\rightarrow}{y} + \frac{r_2}{2}\right) U'\left(\underset{\rightarrow}{y} - \frac{r_2}{2}\right) = U^2(\underset{\rightarrow}{y}) e^{-\sigma\pi r_e^2/L^2} \tag{A9}$$

rather than modelling U itself.

One must keep in mind that the correlation functions and the mean velocity profile are but crude estimates of the ones that would be measured in a real jet flow. The spatial and temporal behaviour of the model functions is hopefully illustrative of the general nature of the 'real' functions.

Jet Noise Estimate

The shear noise contribution to the total far field acoustic pressure according to the theory of Ref. 10 is:

$$p_{SH}(\underset{\rightarrow}{x},t) = \frac{\rho_o}{2\pi c_o^2 |\underset{\rightarrow}{x}|} \int U_x(\underset{\rightarrow}{y}) \frac{\partial^2}{\partial t^2} u_x(\underset{\rightarrow}{y}, t - c_o^{-1} |\underset{\rightarrow}{x} - \underset{\rightarrow}{y}|) d\underset{\rightarrow}{y} \qquad (A10)$$

The shear noise auto-correlation is evaluated from a double volume integral:

$$R_{SH}(\underset{\rightarrow}{x},\tau) = \frac{\rho_o^2}{4\pi^2 c_o^4 |\underset{\rightarrow}{x}|^2} \iint U_x(\underset{\rightarrow}{z}_1) U_x(\underset{\rightarrow}{z}_2)$$

$$\cdot \overline{\frac{\partial^2}{\partial t^2} u_x(\underset{\rightarrow}{z}_1, t - c_o^{-1} |\underset{\rightarrow}{x} - \underset{\rightarrow}{z}_1|) \frac{\partial^2}{\partial t^2} u_x(\underset{\rightarrow}{z}_2, t - \tau - c_o^{-1} |\underset{\rightarrow}{x} - \underset{\rightarrow}{z}_2|)} d\underset{\rightarrow}{z}_1 d\underset{\rightarrow}{z}_2 \qquad (A11)$$

Ribner (Ref. 10) has argued that cross-terms such as $[\partial^2/\partial t^2(u_x)\ \partial^2/\partial t^2(u_x^2)]$ which are found in a more rigorous description, will be small or identically zero. After transformation of the variables $\underset{\rightarrow}{z}_1 = \underset{\rightarrow}{y} - 1/2\ \underset{\rightarrow}{\eta}$, $\underset{\rightarrow}{z}_2 = \underset{\rightarrow}{y} + 1/2\ \underset{\rightarrow}{\eta}$, and application of the identity

$$\frac{\partial^2}{\partial t^2} u_x \frac{\partial^2}{\partial t^2} u'_x = \frac{\partial^4}{\partial \tau^4} u_x u'_x \qquad (A12)$$

the auto-correlation takes the form:

$$R_{SH}(\underset{\rightarrow}{x},\tau) = \frac{\rho_o^2}{4\pi^2 c_o^4 |\underset{\rightarrow}{x}|^2} \iint U_x\left(\underset{\rightarrow}{y} - \frac{1}{2}\underset{\rightarrow}{\eta}\right) U_x\left(\underset{\rightarrow}{y} + \frac{1}{2}\eta\right)$$

$$\cdot \overline{\frac{\partial^4}{\partial \tau^4} u_x\left(\underset{\rightarrow}{y} - \frac{1}{2}\underset{\rightarrow}{\eta},\ t\right) u_x\left(\underset{\rightarrow}{y} + \frac{1}{2}\underset{\rightarrow}{\eta},\ t - \tau - \frac{\underset{\rightarrow}{\eta} \cdot \underset{\rightarrow}{x}}{|\underset{\rightarrow}{x}| c_o}\right)} d\underset{\rightarrow}{y} d\underset{\rightarrow}{\eta} \qquad (A13)$$

The integration over $\underset{\rightarrow}{\eta}$ evaluates the contribution to $R_{SH}(\underset{\rightarrow}{x},\tau)$ from a correlation volume at $\underset{\rightarrow}{y}$. It is convenient to replace the cross-correlation by the equivalent Fourier integral representation. An observer moving at the convection velocity would measure:

$$\overline{u_x u'_x} = \int \Phi_{u_x u_x}(\underset{\rightarrow}{y}, \underset{\rightarrow}{k}, \omega) e^{-i\underset{\rightarrow}{k} \cdot \underset{\rightarrow}{\xi}} e^{-i\omega\tau} d\underset{\rightarrow}{k} d\omega \qquad (A14)$$

Substitution of $\vec{\xi} - \vec{U}_c\tau$ for $\vec{\xi}$ changes the moving frame correlations to fixed frame correlations:

$$\overline{u_x u'_x} = \int \Phi_{u_x u_x}(\vec{y},\vec{k},\omega) e^{-i\vec{k}\cdot(\vec{\xi}-\vec{U}_c\tau)} e^{-i\omega\tau} \, d\vec{k} \, d\omega \qquad \text{(A15)}$$

It follows that

$$R_{SH}(\vec{x},\tau) = \frac{\rho_o^2}{4\pi^2 c_o^4 |\vec{x}|^2} \iiint U_x^2(\vec{y})(\omega - \vec{k}\cdot\vec{U}_c)^4 \Phi_{u_x u_x}(\vec{y},\vec{k},\omega)$$
$$e^{-i(\omega - \vec{k}\cdot\vec{U}_c)} e^{-i\left(\vec{k} + (\omega - \vec{k}\cdot\vec{U}_c)\frac{\vec{x}}{c_o|\vec{x}|}\right)\cdot\vec{\eta}} e^{-\frac{c^2}{2}(\eta_3^2 + \eta_2^2)} \, d\vec{y} \, d\omega \, d\vec{k} \, d\vec{\eta} \qquad \text{(A16)}$$

The grouping of the variables in the exponentials suggests a change of variables:

$$\vec{q} = \vec{k} + (\omega - \vec{k}\cdot\vec{U}_c)\frac{\vec{x}}{c_o|\vec{x}|}$$
$$\Omega = (\omega - \vec{k}\cdot\vec{U}_c) \qquad \text{(A17)}$$

The Jacobian of this transformation is unity. The new variables will simplify the integration over the wave number-frequency space; convection effects are also accounted for [viz $(\omega - \vec{k}\cdot\vec{U}_c)$]. Refraction of sound has been suppressed by replacing the perturbed density ρ within the jet by the ambient value ρ_o (Ref. 24). Integrating over $\vec{\eta}$ and q_1 results in:

$$R_{SH}(\vec{x},\tau) = \frac{\rho_o^2}{16a^4\alpha U_c} \cdot \frac{1}{\pi c_o^4 |\vec{x}|} \int U_x^2(\vec{y}) \, u_1^2(\vec{y}) \Omega^4 \frac{q_3^2 + q_2^2\cos^2\theta}{4a^2}$$
$$e^{-\frac{2a^2 + c^2}{4a^2c^2}(q_2^2 + q_3^2)} e^{\frac{q_2}{2a^2}\frac{\Omega}{c_o}\sin\theta} e^{-\frac{c^2}{4a^2\alpha^2 U_c^2}\Omega^2} e^{-i\Omega\tau} \, d\vec{y} \, d\Omega \, dq_2 \, dq_3 \qquad \text{(A18)}$$

where $C = [(1 - M_c\cos\theta)^2 + \alpha^2 M^2]^{1/2}$ is the convection factor first found by Ribner (Ref. 5) and Ffowcs-Williams (Ref. 11); M_c is the convection Mach number, $c_o M_c = U_c$ is typically half the jet velocity (Ref. 82). After integration over q_2 and q_3, one finds that the shear noise auto-correlation is the Fourier transform of the spectral contributions from all correlation volumes in the jet flow:

$$R_{SH}(\underset{\rightarrow}{x},\tau) = \frac{\rho_o^2}{8\pi\alpha U_c c_o^4 |\underset{\rightarrow}{x}|^2} \frac{c^2}{a^2} \frac{1}{2a^2 + c^2} \int U_x^2(\underset{\rightarrow}{y}) \overline{u_1^2}(\underset{\rightarrow}{y}) \Omega^4$$

$$\left(1 + \cos^2 + \frac{1}{2}\frac{c^2}{a^2}\frac{1}{2a^2 + c^2}\frac{\Omega^2}{c_o^2} \sin^2\theta \cos^2\theta\right) e^{-\frac{c_{SH}^2}{4a^2\alpha^2 U_c^2}\Omega^2} e^{-i\Omega\tau} \, d\underset{\rightarrow}{y} \, d\Omega \tag{A19}$$

For the shear flow the convection factor comes out to be:

$$C_{SH} = \left[(1 - M_c\cos\theta)^2 + \alpha^2 M_c^2 \left(1 - \frac{c^2}{2a^2 + c^2}\sin^2\theta\right)\right]^{1/2} \tag{A20}$$

There is virtually no difference between C and C_{SH} at low convection Mach numbers.

The volume integral of all spectral contributions (deleting the Fourier transformation in Eq. A19) defines the power spectrum of the shear noise. The spectral contribution from a unit volume is:

$$d\varphi_{SH} \cong \frac{\rho_o^2}{8\pi\alpha U_c c_o^4 |\underset{\rightarrow}{x}|^2} \frac{c^2}{a^2} \frac{\Omega^4}{(2a^2 + c^2)^2} U_x^2(\underset{\rightarrow}{y}) \overline{u_1^2}(\underset{\rightarrow}{y})(1 + \cos^2\theta) e^{-\frac{c_{SH}^2}{4a^2\alpha^2 U_c^2}\Omega^4} d\underset{\rightarrow}{y} \tag{A21}$$

The peak frequency of $d\varphi_{SH}$ is

$$f_{p_{SH}} = \frac{\sqrt{2}\, a\alpha U_c}{\pi C_{SH}} \tag{A22}$$

since $.5[a^{-2}c^2\sin^2\theta \cdot \cos^2\theta/(2a^2 + c^2)]$ is much smaller than $(1 + \cos^2\theta)$.

The mean square pressure $\overline{p_{SH}^2} = R_{SH}(x,0)$ can be written in the form:

$$\overline{p_{SH}^2} = \int_V Q_{SH} \, d\underset{\rightarrow}{y}$$

$$Q_{SH} = \frac{3\rho_o^2 U_x^2(\underset{\rightarrow}{y}) \overline{u_1^2}(\underset{\rightarrow}{y}) \alpha^4 M_c^4}{\pi |\underset{\rightarrow}{x}|^2 C_{SH}^5} \frac{\sigma}{(2 + \sigma)^2} a \left(1 + \cos^2 + \frac{5\sigma}{2 + \sigma}\frac{\alpha^2 M_c^2}{C_{SH}^2}\sin^2\theta\cos^2\theta\right) \tag{A23}$$

where $\sigma = c^2/a^2$; $\sigma < 1$, as the correlation length (α 1/a) cannot be greater than the jet diameter (α 1/c). Q_{SH} can be interpreted as the shear noise

contribution per unit volume to the overall mean square pressure. The integral of Q_{SH} over the local cross-section of the jet would correspond to the shear noise contribution to the source strength per unit length. The basic directivity of Q_{SH} is proportional to:

$$\frac{U_x^2}{U_1^2}(1 + \cos^2\theta) = \cos^2\theta(1 + \cos^2\theta) \tag{A24}$$

The basic directivity is modified by the convection factor resulting in a downstream bias and refraction which is not included herein. Ribner (Ref. 10) as well as Pao and Lowson (Ref. 78) have obtained the same basic directivity for the shear noise term. (Pao and Lowson defined the shear noise source term to be

$$\text{SHEAR NOISE} \; \alpha \; \frac{\partial U_i}{\partial y_j} \frac{\partial u_j}{\partial y_i} \tag{A25}$$

which appears to be equivalent in an integral sense to Ribner's definition used herein.)

A similar analysis may be performed for the self noise given by:

$$p_{SF}(\underrightarrow{x},t) = \frac{\rho_o}{4\pi c_o^2 |\underrightarrow{x}|} \int \frac{\partial^2}{\partial t^2} u_x^2(\underrightarrow{y}, t - c_o^{-1}|\underrightarrow{x} - \underrightarrow{y}|) d\underrightarrow{y} \tag{A26}$$

The mean square self noise pressure is:

$$\overline{p_{SF}^2} = \int Q_{SF} \, d\underrightarrow{y} \tag{A27}$$

with

$$Q_{SF} = \frac{3\sqrt{2}}{4\sqrt{\pi}} \frac{\rho_o^2}{c^5} \frac{[\overline{u_1^2}(\underrightarrow{y})]^2}{|\underrightarrow{x}|^2} \alpha^4 M_c^4 a$$

The spectral distribution is proportional to

$$d\varphi_{SF} = \frac{\rho_o^2}{128\pi a^4 \alpha U_c c_o^4 |\underrightarrow{x}|} [\overline{u_1^2}(\underrightarrow{y})]^2 \Omega^4 \, e^{-\frac{c^2}{8a^2\alpha^2 U_c^2}\Omega^2} \tag{A28}$$

and has a maximum at

$$f_{p_{SF}} = \frac{2a\alpha U_c}{\pi c} \tag{A29}$$

The ratio of the self and shear noise radiated by a unit volume of jet is:

$$\frac{Q_{SF}}{Q_{SH}} = \frac{\sqrt{2}\ (2+\sigma)^2}{\sigma} \frac{\overline{u_1^2}(\underset{\rightarrow}{y})}{U_1^2(\underset{\rightarrow}{y})} \frac{C_{SH}^5}{C^5} \frac{1}{\cos^2\theta(1+\cos^2\theta)} \qquad \text{(A30)}$$

The ratio is governed by the spatial scales of the mean flow and the turbulence (σ), the turbulence intensity distribution and the basic directivity of the shear noise (the basic self noise is omnidirectional). Convection effects C_{SH}^5/C^5 tend to cancel.

The self and shear noise spectral contributions peak at different frequencies. Nossier and Ribner (Ref. 37) have found that the peak self and shear noise frequencies extracted from far-field data differ by a factor of about 2. The Gaussian correlation model of the present analysis predicts a peak frequency ratio of $\sqrt{2}$. McCartney (Ref. 77) has discussed the dependence of the frequency shift on the choice of the temporal form of the correlation and cited several examples. The model self noise spectrum can be modified to exhibit the observed frequency shift: The argument of the exponential of the self noise spectrum $C^2/8a^2\alpha^2U_c^2$ is multiplied by a factor of 1/2. Hence the peak frequency, defined by the sensible solution of

$$\frac{\partial}{\partial\omega}\ \omega^4\ e^{-\frac{C^2}{16a^2\alpha^2U_c^2}\omega^2} = 0 \qquad \text{(A31)}$$

becomes

$$\hat{f}_{p_{SF}} = \frac{2\sqrt{2}\ a\alpha U_c}{\pi C} = 2f_{p_{SH}} \qquad \text{(A32)}$$

Integration over Ω results in a factor of $2^{5/2}$, thus

$$\frac{Q_{SF}}{Q_{SH}} = \frac{(2+\sigma)^2}{\sigma} \frac{\overline{u_1^2}}{U_1^2} \frac{C_{SH}^5}{C^5} \frac{2}{\cos^2\theta(1+\cos^2\theta)} \qquad \text{(A33)}$$

The jet half width is given by the empirical relation $b_{1/2} = .0848y_1$ (Ref. 81); thus $c = 9.82/y_1$. The turbulence scale is estimated to be $L_1 = .13y_1$ (Ref. 82), and as $a = \sqrt{\pi}/L$ the square of the ratio of the length scales becomes $\sigma = .52$. σ is somewhat sensitive to the choice of L_1 and $b_{1/2}$; therefore, the value of $\sigma = .45$ used by Ribner (Ref. 9) has been chosen. This yields

$$\frac{Q_{SF}}{Q_{SH}} = 1.2 \frac{2}{\cos^2\theta(1+\cos^2\theta)}$$

a value compatible with the work of Nossier and Ribner (Ref. 37).

Strength Distribution of Noise Sources Along a Jet

The functions Q_{SF} and Q_{SH} describe the contribution of a unit volume to the overall self and shear noise respectively. It is often assumed that the temporal and spatial scales of the turbulence do not change over a slice of jet. If the behaviour of $\overline{u_1^2}$ U_1^2 and $(\overline{u_1^2})^2$ are known, one may estimate the contribution of a slice of jet to the overall jet noise.

The individual contributions to $\overline{p^2}$ from unit volume given by Eqs. A23 and A27 may be written as:

$$Q_{SH} = \frac{3\rho_o^2 U_x^2(\underline{y}) u_1^2(y)}{\pi^2 |\underline{x}|^2 C_{SH} c_o^4} \frac{a^4 \alpha^4 U_c^4}{C_{SH}^4} \frac{\sigma}{(2+\sigma)^2} \frac{1}{a^3} \left(1 + \cos^2\theta + \frac{5\sigma}{2+\sigma} \frac{\alpha^2 M_c^2}{C_{SH}^2} \sin^2\theta\cos^2\theta \right)$$

$$= \frac{3\rho_o^2 U_x^2(\underline{y}) \overline{u_1^2}(\underline{y})}{\pi^2 |\underline{x}|^2 C_{SH} c_o^4} \omega_o^4 L^3 \frac{\sigma}{(2+\sigma)^2} \left(1 + \cos^2\theta + \frac{5\sigma}{2+\sigma} \frac{\alpha^2 M_c^2}{C_{SH}^2} \sin^2\theta\cos^2\theta \right) \quad \text{(A34)}$$

Similarly,

$$Q_{SF} = \frac{3\sqrt{2}\,\rho_o^2}{4\pi^2} \frac{[\overline{u_1^2}(\underline{y})]}{c_o^4 |\underline{x}|^2 C} \omega_o^4 L^3 \quad \text{(A35)}$$

ω_o is a typical frequency that is assumed to scale as $U_1(y_1)/y_1$ (Ref. 1); the correlation length L varies as y_1. Thus the contributions of a slice of jet scale as:

$$\beta_{SF}(y_1) = \frac{U_1^4(y_1)}{y_1} \int_{A(y_1)} [u_1^2(\underline{y})]^2 \, dA \quad \text{(A36)}$$

$$\beta_{SH}(y_1) = \frac{U_1^4(y_1)}{y_1} \int_{A(y_1)} [u_1^2(\underline{y}) U_x^2(\underline{y})] dA \quad \text{(A37)}$$

The area integrals have been evaluated from measured turbulence intensities $\sqrt{u_1^2}/U_I$ and mean velocities of the UTIAS 3/4" model jet (see Fig. 4.6). The functions $\beta_{SH}(y_1/D)/\beta_{SH}(3)$ and $\beta_{SF}(y_1/D)/\beta_{SF}(3)$ are shown in Fig. A1; they are proportional to relative self-shear noise contributions to the far-field acoustic power from a unit length of jet.

Ribner (Ref. 7) and others (Refs. 5, 8) used similarity and scaling arguments to predict that the source strength distribution per unit length follows a y_1^0 law (i.e. constant contribution of a slice of jet to the far field acoustic power) in the mixing region, and a y^{-7} law in the fully developed jet. The present model is a hybrid combining scaling considerations ($\omega_o \propto U_1/y_1$,

$L \alpha y_1$) and certain products of measured jet flow velocities, as described by Eqs. A36 and A37. The peak turbulence intensity is not constant in the mixing region reaching a maximum value near $y_1/D = 5$. Hence Ribner's y_1° law, predicated on the assumption of constant turbulence intensity, is not satisfied. Downstream of the potential core ($y_1/D > 4$) β_{SF} and β_{SH} decrease rapidly, and do approach the y_1^{-7} law predicted for the fully developed jet.

Hypothetical Cross-Correlations

The procedure of estimating the cross-correlations $\overline{u_x(\underset{\rightarrow}{y},t)p(\underset{\rightarrow}{x},t-\tau)}$ and $\overline{u_x^2(\underset{\rightarrow}{y},t)p(\underset{\rightarrow}{x},t-\tau)}$ is similar to the one employed in the computation of the far field pressure. The analysis evaluates the cross-correlation functions that would be measured, if the flow were accurately described by the assumed correlations of the model.

The shear noise correlation is:

$$R_{u_x p}(\underset{\rightarrow}{x},\underset{\rightarrow}{y},\tau) = \overline{u_x(\underset{\rightarrow}{y},t)p(\underset{\rightarrow}{x},t+\tau)}$$

$$= \frac{1}{2\pi c_o^2}\frac{\rho_o}{|\underset{\rightarrow}{x}|}\int \overline{U_x(\underset{\rightarrow}{y}+\underset{\rightarrow}{\xi})\, u_x(\underset{\rightarrow}{y},t)\frac{\partial^2}{\partial t^2}u_x(\underset{\rightarrow}{y}+\underset{\rightarrow}{\xi},\, t+\tau-c_o^{-1}|\underset{\rightarrow}{x}-\underset{\rightarrow}{y}-\underset{\rightarrow}{\xi}|)}\, d\underset{\rightarrow}{\xi} \qquad \text{(A38)}$$

where $\underset{\rightarrow}{\xi}$ is the separation of an arbitrary point and the source point $\underset{\rightarrow}{y}$. The cross-correlation $u_x u_x'$ is non-zero only for small values of $|\xi|$ (correlation volume of u_x). The variation of the mean velocity U_x over the correlation volume will distort the integrand. For the case of homogeneous isotropic turbulence and flow parallel to the jet axis, the integrand will be maximum at $\underset{\rightarrow}{y}+\underset{\rightarrow}{\epsilon}$, where $\underset{\rightarrow}{\epsilon}$ is a slight offset towards the jet centre line. Upon substitution for U_x and replacement of the cross correlation $\partial^2/\partial\tau^2(\overline{u_x u_x'})$ with the equivalent Fourier integral, $R_{u_x p}(\underset{\rightarrow}{x},\underset{\rightarrow}{y},\tau)$ becomes:

$$R_{u_x p}(\underset{\rightarrow}{x},\underset{\rightarrow}{y},\tau) = -\frac{1}{2\pi c_o^2}\frac{\rho_o}{|\underset{\rightarrow}{x}|}U_1\cos\theta\int (\omega-\underset{\rightarrow}{k}\cdot\underset{\rightarrow}{U}_c)^2\,\varphi_{u_x u_x}(\underset{\rightarrow}{y},\underset{\rightarrow}{k},\omega)$$

$$e^{-i(\omega-\underset{\rightarrow}{k}\cdot\underset{\rightarrow}{U}_c)(\tau-c_o^{-1}|\underset{\rightarrow}{x}|)}\; e^{i\underset{\rightarrow}{k}\cdot\underset{\rightarrow}{y}}\; e^{-i\left(\underset{\rightarrow}{k}+(\omega-\underset{\rightarrow}{k}\cdot\underset{\rightarrow}{U}_c)\frac{\underset{\rightarrow}{x}}{c_o|\underset{\rightarrow}{x}|}\right)\cdot(\underset{\rightarrow}{y}+\underset{\rightarrow}{\xi})}$$

$$e^{-c^2[(y_2+\xi_2)^2+(y_3+\xi_3)^2]}\, d\omega\, d\underset{\rightarrow}{k}\, d\underset{\rightarrow}{\xi} \qquad \text{(A39)}$$

After the change of variables:

$$\underset{\rightarrow}{y} = \underset{\rightarrow}{y}+\underset{\rightarrow}{\xi}$$

$$\underset{\rightarrow}{q} = \left(\underset{\rightarrow}{k}+(\omega-\underset{\rightarrow}{k}\cdot\underset{\rightarrow}{U}_c)\frac{\underset{\rightarrow}{x}}{c_o|\underset{\rightarrow}{x}|}\right) \qquad \text{(A40)}$$

$$\Omega = \omega - \underset{\rightarrow}{k}\cdot\underset{\rightarrow}{U}_c$$

one observes that

$$\int e^{-i\vec{q}\cdot\vec{\eta}}\, e^{-c^2(\eta_2^2+\eta_3^2)}\, d\vec{\eta} \qquad (A41)$$

is the three dimensional Fourier transform of $e^{-c^2(\eta_3^2+\eta_2^2)}$ and

$$R_{u_x p}(\vec{x},\vec{y},\tau) = -\frac{\rho_o \overline{u_1^2} U_1 \cos\theta}{16\pi a^4 c^2 \alpha U_c c_o^2 |\vec{x}|} \int \Omega^2 \frac{q_3^2 + q_2^2\cos^2\theta}{4a^2} e^{-\frac{a^2+c^2}{4a\tau^2}(q_3^2+q_2^2)}$$

$$\frac{1}{e^{2a^2}} \frac{\Omega}{c_o} q_2 \sin\theta \; e^{i(q_2 y_2 + q_3 y_3)} \; e^{-\frac{c^2}{4a^2\alpha^2 U_c^2}\Omega^2} \; e^{-i\Omega(\tau - c_o^{-1}|\vec{x}-\vec{y}|)} \; d\Omega\, dq_2\, dq_3 \qquad (A42)$$

A lengthy but straightforward integration results in:

$$R_{u_x p}(\vec{x},\vec{y},\tau) = -\frac{\sqrt{\pi}}{2} \frac{\rho_o \overline{u_1^2} U_1 \cos\theta}{a\hat{C}_{SH}^3 |\vec{x}|} \alpha^2 M_c^2 \frac{\sigma}{(1+\sigma)^2} e^{-\frac{\sigma}{1+\sigma} a^2 (y_2^2+y_3^2)}$$

$$\left\{ \left(1 + \cos^2\theta - 2a^2 \frac{\sigma}{1+\sigma}(y_3^2 + y_2^2\cos^2\theta) + 3\frac{\sigma}{1+\sigma}\frac{\alpha^2 M_c^2}{\hat{C}_{SH}^2} \sin^2\theta\cos^2\theta \right) \right.$$

$$\left(1 - 2\frac{a^2\alpha^2 U_c^2}{\hat{C}_{SH}^2}\hat{\tau}^2 \right) + \sin 2\theta \frac{\sigma}{1+\sigma} \frac{\alpha M_c \cos\theta}{\hat{C}_{SH}} \frac{a\alpha U_c}{\hat{C}_{SH}} \hat{\tau} \left(2ay_2 - \alpha M_c \sin\theta \frac{a\alpha U_c}{\hat{C}_{SH}} \hat{\tau} \right)$$

$$\left. \left(3 - 2\frac{a^2\alpha^2 U_c^2}{\hat{C}_{SH}^2}\hat{\tau}^2 \right) \right\} e^{-\frac{a^2\alpha^2 U_c^2}{\hat{C}_{SH}^2}\hat{\tau}^2} \qquad (A43)$$

where

$$\hat{\tau} = \tau - c_o^{-1}|\vec{x} - \vec{y}| - \frac{\sigma}{1+\sigma} c_o^{-1} y_2 \sin\theta$$

$$\hat{C}_{SH} = \left[(1 - M_c\cos^2\theta)^2 + \alpha^2 M_c^2 \left(1 - \frac{\sigma}{1+\sigma}\sin^2\theta \right) \right]^{1/2}$$

$$\sigma = \frac{c^2}{a^2}$$

The 'interaction' of the mean shear and the two point turbulent velocity correlation has generated two functions, one of which is even about $\hat{\tau} = 0$, the other odd. In effect the mean shear has destroyed the homogeneity and the isotropy of the correlation. The turbulence structure of the jet flow is not homogeneous and isotropic, and one would expect the measured cross-correlations of the shear noise source term with the far field sound to be somewhat sensitive to the position of the source point in the jet.

The relative amplitudes of the even and odd functions predicted above are plotted in Fig. A2. The apparent position of the source has shifted from $\underset{\rightarrow}{y}$ to $(y_1, (1+\sigma)^{-1} y_2, y_3)$. The shift is not very significant from the point of view of the percentage change in arrival time. The shift may become significant if axial variations in the mean flow (neglected herein) are considered.

In order to compute the contribution to the far field shear noise from a unit volume at $\underset{\rightarrow}{y}$, one must double differentiate the cross-correlation with respect to τ and evaluate the result at $\tau = c_o^{-1} |\underset{\rightarrow}{x}-\underset{\rightarrow}{y}|$ (in the frequency domain the cross-spectrum must be multiplied by $-(\omega-\underset{\rightarrow}{k}\cdot\underset{\rightarrow}{U}_c)^2$). The apparent source shift implies that the resulting function is evaluated near, but not at, its maximum. Should one neglect the small time shift one would overestimate the shear noise contribution (the same applies to the estimate of the far field shear noise spectrum; here the time shift takes the form of an additional phase angle). The error can be considerable, as the double time derivative brings about a narrower peak.

The cross-correlation $R_{u_x p}(\underset{\rightarrow}{x}, y, \tau)$ may be normalized by the RMS values of u_x and p which are given by:

$$\sqrt{\overline{u_x^2}} = \sqrt{\overline{u_1^2}} \tag{A44}$$

$$\sqrt{\overline{p^2}} \cong \frac{\sqrt{6}\,\rho_o \sqrt{\overline{u_1^2}}\, U_1 \alpha^2 M_c^2}{\pi\, |\underset{\rightarrow}{x}|\, c^{5/2}} \sqrt{a} \left(\frac{\overline{u_1^2}}{U_1^2} + \frac{\sigma}{(2+\sigma)^2} \frac{\cos^2\theta(1+\cos^2\theta)}{2} \right)^{1/2} V_{JET}^{1/2} \tag{A45}$$

For the present model the strongest shear noise correlation is predicted to be along the jet axis ($y_2 = y_3 = 0$); thus, the normalized correlation is estimated by:

$$\frac{R_{u_x p}}{\sqrt{\overline{u_x^2}\,\overline{p^2}}} = \frac{\pi^{3/4}}{\sqrt{6}} \frac{1}{a^{3/2} V_{JET}^{1/2}} \frac{\sigma}{(1+\sigma)^2} \frac{\cos\theta(1+\cos^2\theta)}{\frac{2\sqrt{\sigma}}{(2+\sigma)} \left(1 + \frac{\cos^2\theta(1+\cos^2\theta)}{2} \right)^{1/2}} \tag{A46}$$

which takes the form

$$\frac{R_{u_x p}}{\sqrt{\overline{u_x^2}\,\overline{p^2}}} \approx .16 \sqrt{\frac{L^3}{V_{JET}}} \tag{A47}$$

for $\sigma = .45$, $L = \sqrt{\pi}\, a^{-1}$, $\theta = 40°$.

V_{JET}/L^3 has been interpreted (Ref. 39) as the number of uncorrelated volume sources assumed to be of equal strength; the correlation coefficient, therefore, is inversely proportional to the square root of the number of uncorrelated sources in the jet.

The self noise correlation is:

$$R_{u_x^2 p}(\underset{\rightarrow}{x},\underset{\rightarrow}{y},\tau) = \frac{\rho_o}{4\pi c_o^2 |\underset{\rightarrow}{x}|} \int \overline{u_x^2(\underset{\rightarrow}{y},t) \frac{\partial^2}{\partial t^2} u_x(\underset{\rightarrow}{y} + \underset{\rightarrow}{\xi},\ t + \tau - c_o^{-1} |\underset{\rightarrow}{x} - \underset{\rightarrow}{y} - \underset{\rightarrow}{\xi}|)}\, d\underset{\rightarrow}{\xi} \tag{A48}$$

does not suffer from the shear flow interaction. After some algebra:

$$R_{u_x^2 p}(\underset{\rightarrow}{x},\underset{\rightarrow}{y},\tau) = \frac{\sqrt{2\pi}}{4} \frac{\rho_o \overline{(u_1^2)^2} \alpha^2 M_c^2}{c^5 |\underset{\rightarrow}{x}|} \left(1 - 4 \frac{a^2 \alpha^2 U_c^2}{c^2} (\tau - \tau_o)^2\right) e^{-\frac{2a^2\alpha^2 U_c^2}{c^2}(\tau-\tau_o)^2} \quad ; \quad \tau_o = c_o^{-1} |\underset{\rightarrow}{x} - \underset{\rightarrow}{y}| \tag{A49}$$

The normalized self noise correlation is given by:

$$\frac{R_{u_x^2 p}}{\overline{(u_x^2)^2}\ \overline{p^2}} = \frac{\pi^{3/4}}{\sqrt{12}} \frac{1}{a^{3/2} V_{JET}^{1/2}} \frac{1}{\left(1 + \frac{\cos^2\theta(1 + \cos^2\theta)}{2}\right)^{1/2}} = .24 \sqrt{\frac{L^3}{V_{JET}}} \tag{A50}$$

when $\sigma = .45$, $L = \sqrt{\pi}\, a^{-1}$, $\theta = 40°$.

Summary

A simple turbulence-plus-mean flow model has been used to illustrate what is hoped to be the general nature of the measured functions $R_{u_x p}$ and $R_{u_x^2 p}$. The model predicts that the peak of the shear noise correlation $R_{u_x p}$ will occur at a time delay different from the travel time $c_o^{-1} |\underset{\rightarrow}{x}-\underset{\rightarrow}{y}|$. Measured $R_{u_x p}$ cross-correlations (see Section 6.1) indicate that the predictions considerably underestimate the shift in the time delay.

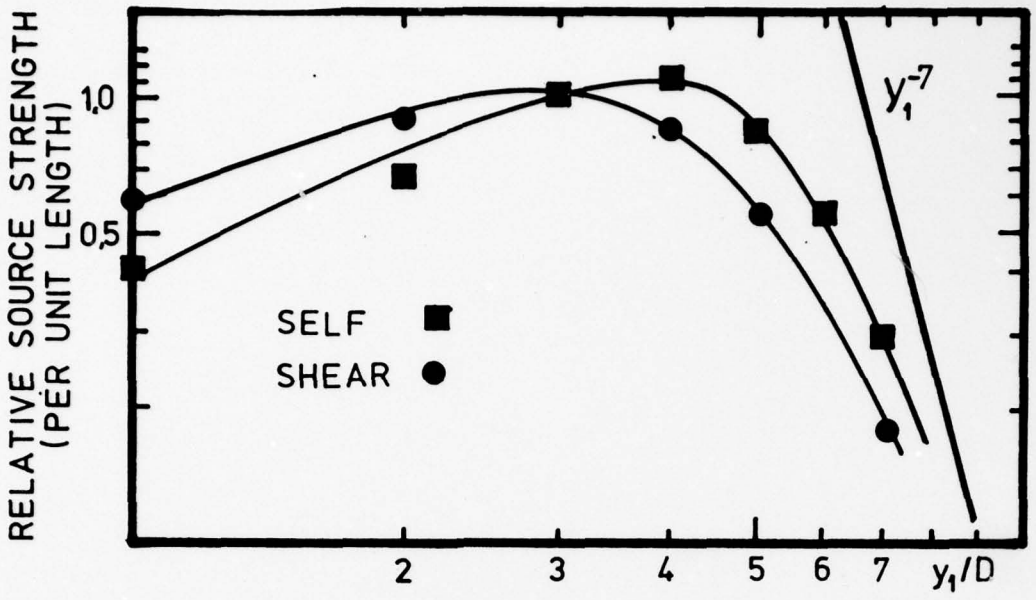


FIG. A.1 RELATIVE SOURCE STRENGTH PER UNIT LENGTH AS A FUNCTION OF AXIAL POSITION. THE CURVES HAVE BEEN NORMALIZED BY THEIR RESPECTIVE VALUES AT $y_1/D = 3$.

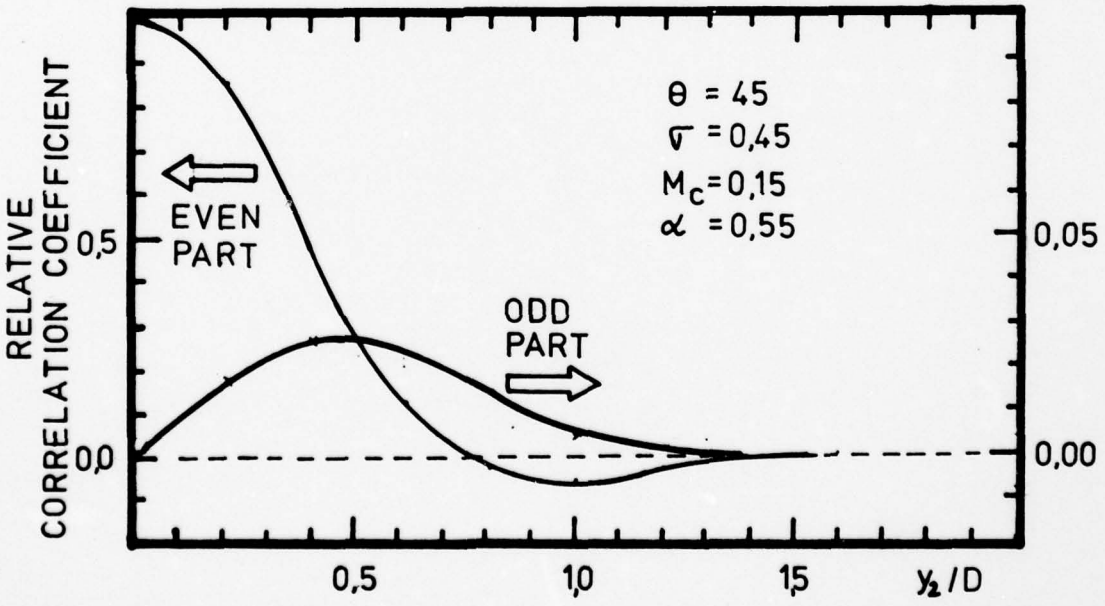


FIG. A.2 RADIAL PROFILE OF THE PEAK VALUES OF THE EVEN AND ODD PARTS OF THE MODEL CROSS-CORRELATION $R_{u_x p}(\underset{\rightarrow}{x}, \underset{\rightarrow}{y}, \tau)$, NORMALIZED BY THE PEAK VALUE AT $y_2/D = 0$.

AD-A062 605 TORONTO UNIV DOWNSVIEW (ONTARIO) INST FOR AEROSPACE --ETC F/G 20/1
DIRECT CORRELATION OF NOISE AND FLOW OF A JET USING LASER DOPPL--ETC(U)
JUN 78 W G RICHARZ AFOSR-75-2808

UNCLASSIFIED UTIAS-230 AFOSR-TR-78-1641 NL

2 OF 2
ADA
062605



END
DATE
FILMED
3 -79
DDC

APPENDIX B

NOISE GENERATED BY TRANSDUCER-FLOW INTERACTION

Even though the principal velocity measuring system used during the present investigation was the Laser Doppler Velocimeter, some thought was given to the problem of transducer-flow interaction, as the hot-wire anemometer will continue to be the most common velocity sensor used in fluid flow research. The instrument is available 'off the shelf' and does not entail the extensive ancillary system development required for the Laser Doppler Velocimeter. Furthermore, the volume of the active sensor is very small compared to the measuring volume of a Laser Doppler Velocimeter, making the hot-wire anemometer ideally suited to survey scale model flows.

A solid object, such as a hot wire probe and its supports, radiates sound when placed in a turbulent flow. Curle has provided an analytical framework that allows one to predict the sound generated by such flow-surface interactions (Ref. 42). The theory identifies fluctuating forces (lift for example) as sound generators. This is confirmed by direct correlation of the force with the radiated sound as was done by Clark and Ribner (Ref. 43). Curle shows that dipole radiation due to flow-surface interaction can be of comparable intensity with the quadrupole radiation of a turbulent flow, if the Mach number is small enough.

A hot wire probe when properly placed in a jet flow does not produce a measurable increase in the radiated noise (it is unlikely that a 1% increase in sound pressure level can be detected with any confidence). In Appendix A it is shown that the normalized cross-correlation coefficients of the velocity-pressure correlations are of order $N^{-\frac{1}{2}}$ if there are N uncorrelated radiators of equal strength Each source contributes an amount $\overline{\Delta p^2}$ to the mean square pressure. The mean square pressure generated by the probe-flow interaction is assumed to be $\epsilon\overline{\Delta p^2}$, $\epsilon = O(1)$. The new overall RMS sound pressure is $\sqrt{(N+\epsilon)\overline{\Delta p^2}}$ and as $N \gg \epsilon$ there is little change in the far field pressure. The correlation function of the measured velocity and the jet noise is now of order $(1+\epsilon)/\sqrt{N}$, as the sound generated by the probe is well correlated with the measured velocity, the turbulent flow being responsible for the fluctuating forces on the probe. Since $\epsilon = O(1)$ the error due to probe noise, which is an artifact of the measurement, can seriously 'contaminate' or obscure the jet noise-jet flow cross-correlation.

The interaction of a sound wave with a solid object generates a diffracted wave by virtue of the reaction of the surface to the forces exerted on it by the incident wave. If the body is at rest, the reaction is such as to maintain zero velocity normal to the surface. The velocity distribution necessary to cancel the incident normal velocity can be generated by a collection of acoustic sources located inside or on the surface of the body (Morse, Ref. 83).

Similar boundary conditions are encountered when a body is immersed in a turbulent flow. The forces exerted on the body, just as the stresses in the turbulent flow, act as sound sources. In the presence of solid boundaries the solution of the wave equation,

$$\frac{1}{c_o^2}\frac{\partial^2 p}{\partial t^2} - \nabla^2 p = \frac{\partial^2 \rho_o v_i v_j}{\partial y_i \partial y_j} \qquad \text{(B1)}$$

is given by (Ref. 47):

$$p(\underset{\rightarrow}{x},t) = \frac{1}{4\pi}\int_V \frac{\delta(t' - t + c_o^{-1}|\underset{\rightarrow}{x} - \underset{\rightarrow}{y}|)}{|\underset{\rightarrow}{x} - \underset{\rightarrow}{y}|}\frac{\partial^2}{\partial y_i \partial y_j}\rho_o v_i v_j(\underset{\rightarrow}{y},t')\, d\underset{\rightarrow}{y}\, dt'$$

$$+ \frac{1}{4\pi}\int_S \left\{ \ell_i \frac{\delta(t' - t + c_o^{-1}|\underset{\rightarrow}{x} - \underset{\rightarrow}{y}|)}{|\underset{\rightarrow}{x} - \underset{\rightarrow}{y}|}\frac{\partial}{\partial y_i} p(\underset{\rightarrow}{y},t') \right.$$

$$\left. - \ell_i p(\underset{\rightarrow}{y},t') \frac{\partial}{\partial y_i}\frac{\delta(t' - t + c_o^{-1}|\underset{\rightarrow}{x} - \underset{\rightarrow}{y}|)}{|\underset{\rightarrow}{x} - \underset{\rightarrow}{y}|} \right\} d\underset{\rightarrow}{y}\, dt' \qquad \text{(B2)}$$

where ℓ_i are the direction cosines of the outward drawn normal from the fluid. Equation B1 is an approximate description of sound generation by a turbulent flow. Curle (Ref. 42) has applied the divergence theorem two times to the volume integral and found that for the special case of a stationary surface the radiated sound pressure is:

$$p(\underset{\rightarrow}{x},t) = \frac{1}{4\pi}\int_V \frac{\partial^2}{\partial x_i \partial x_j}\rho_o v_i v_j(\underset{\rightarrow}{y},t')\frac{\delta(t' - t + c_o^{-1}|\underset{\rightarrow}{x} - \underset{\rightarrow}{y}|)}{|\underset{\rightarrow}{x} - \underset{\rightarrow}{y}|}\, d\underset{\rightarrow}{y}\, dt'$$

$$- \frac{1}{4\pi}\int_S \frac{\partial}{\partial x_i} F_i(\underset{\rightarrow}{y},t')\frac{\delta(t' - t + c_o^{-1}|\underset{\rightarrow}{x} - \underset{\rightarrow}{y}|)}{|\underset{\rightarrow}{x} - \underset{\rightarrow}{y}|}\, d\underset{\rightarrow}{y}\, dt' \qquad \text{(B3)}$$

where $F_i = \ell_i \delta_{ij} p$ is the force per unit area exerted on the fluid by the solid boundaries. In the far-field:

$$p(\underset{\rightarrow}{x},t) = \frac{\rho_o}{4\pi c_o^2 |\underset{\rightarrow}{x}|}\int_V \frac{\partial^2}{\partial t^2} v_x^2(\underset{\rightarrow}{y},t')\, \delta(t' - t + c_o^{-1}|\underset{\rightarrow}{x} - \underset{\rightarrow}{y}|)\, d\underset{\rightarrow}{y}\, dt'$$

$$+ \frac{1}{4\pi c_o |\underset{\rightarrow}{x}|}\int \frac{\partial}{\partial t'} F_x(\underset{\rightarrow}{y},t')\, \delta(t' - t + c_o^{-1}|\underset{\rightarrow}{x} - \underset{\rightarrow}{y}|)\, d\underset{\rightarrow}{y}\, dt' \qquad \text{(B4)}$$

The Reynolds stresses $\rho v_i v_j$ and the forces F_i have been replaced by the momentum flux $\rho_o v_x^2$ and a force F_x in the direction of the observer at $\underset{\rightarrow}{x}$. If there is no fluctuating force in the direction of the observer, then the observer will hear no sound due to flow-surface interaction. This can be illustrated by the simple example of an oscillating sphere (a dipole) set in

motion by a force in the horizontal plane. No sound is radiated in the direction normal to the dipole axis which coincides with the force vector.

The forces exerted on the body in a turbulent flow are of aerodynamic origin. Rackl (Ref. 84) reasons that the force can be modelled as:

$$F_x = \frac{1}{2} \rho_o K v_x^2 S \tag{B5}$$

where the pure number K is a function of the body geometry and S is the surface area exposed to the flow. The far field acoustic pressure becomes:

$$p(\underset{\rightarrow}{x},t) = \frac{1}{4\pi c_o^2} \frac{1}{|\underset{\rightarrow}{x}|} \int \frac{\partial^2}{\partial t'^2} \rho_o v_x^2(\underset{\rightarrow}{y},t') \, \delta(t' - t + c_o^{-1} |\underset{\rightarrow}{x} - \underset{\rightarrow}{y}|) \, d\underset{\rightarrow}{y} \, dt'$$

$$\frac{1}{8\pi c_o} \frac{S_{eff}}{|\underset{\rightarrow}{x}|} \int \frac{\partial}{\partial t'} \rho_o K v_x^2(\underset{\rightarrow}{y},t') \, \delta(t' - t + c_o^{-1} |\underset{\rightarrow}{x} - \underset{\rightarrow}{y}|) \, dt' \tag{B6}$$

provided the scale of the body is small compared with the scale of variation of v_x.

The cross-correlation of jet flow with the radiated jet noise gives rise to two types of correlations: one associated with the sound generated by the turbulent flow alone, the other generated by flow-probe interaction. The relative magnitudes of the two correlations can be estimated with the aid of a simple model. As was the case with the self and shear noise model, v separates into a mean velocity U_x and a turbulent velocity $u_x(y,t)$. The cross-correlations $R_{u_x p} = \overline{u_x(\underset{\rightarrow}{y},t) p(\underset{\rightarrow}{x},t+\tau)}$ and $R_{u_x 2p} = \overline{u_x^2(\underset{\rightarrow}{y},t) p(\underset{\rightarrow}{x},t+\tau)}$ are to be estimated. The measured $R_{u_x 2p}$ correlations are too poorly defined to be analyzed with any confidence; therefore, only the $R_{u_x p}$ correlation will be examined.

The velocity is well correlated over the prove sensor and the portion of the probe supports that are immersed in the correlation volume; hence, the cross-correlation is given by:

$$R_{u_x p}(\underset{\rightarrow}{x},\underset{\rightarrow}{y},\tau) = \frac{\rho_o}{2\pi c_o^2 |\underset{\rightarrow}{x}|} \int_V U_x(\underset{\rightarrow}{y} + \underset{\rightarrow}{\xi}) \frac{\partial^2}{\partial \tau^2} \overline{u_x(\underset{\rightarrow}{y},t) u_x(\underset{\rightarrow}{y} + \underset{\rightarrow}{\xi}, t + \tau - c_o^{-1} |\underset{\rightarrow}{x} - \underset{\rightarrow}{y} - \underset{\rightarrow}{\xi}|)} \, d\underset{\rightarrow}{\xi}$$

$$+ \frac{\rho_o K S_{eff} U_x(y)}{4\pi c_o |\underset{\rightarrow}{x}|} \frac{\partial}{\partial \tau} \overline{u_x(\underset{\rightarrow}{y},t) u_x(\underset{\rightarrow}{y},t + \tau - c_o^{-1} |\underset{\rightarrow}{x} - \underset{\rightarrow}{y}|)} \tag{B7}$$

S_{eff} is a measure of the surface area of the probe in the correlation volume.

The analysis in Appendix A shows that the convection effects are small at low Mach numbers; we shall neglect it here. Furthermore, the major

effect of the mean shear is to alter the directivity factor; hence it is assumed to be constant over a correlation volume. Thus the rather simple model correlation:

$$\overline{u_x u_x'} = \overline{u_1^2}\, e^{-a^2[(\xi_1 - U_c\tau)^2 + \xi_2^2 + \xi_3^2 + \alpha^2 U_c^2 \tau^2]} \tag{B8}$$

is chosen for mathematical convenience. Upon substitution in Eq. B7, the small Mach number approximation of the cross-correlation takes the form:

$$R_{u_x p}(\vec{x},\vec{y},\tau) = -\frac{\rho_o U_x \overline{u_1^2}}{\pi|\vec{x}|}\alpha^2 M_c^2 \left\{ \frac{\pi^{3/2}}{a}\left[1 - 2a^2\alpha^2 U_c^2(\tau - \tau_o)\right] e^{-a^2\alpha^2 U_c^2(\tau-\tau_o)^2} \right.$$

$$\left. + \frac{1}{2} S_{eff} \frac{1+\alpha^2}{\alpha^2} K a^2 c_o(\tau - \tau_o)\, e^{-a^2(1+\alpha^2)U_c^2(\tau-\tau_o)^2} \right\} \tag{B9}$$

$R_{u_x p}$ is the sum of an even function and an odd function. The latter is the 'contamination' caused by the probe-flow interference and must be small if the jet flow-jet noise correlation is to be estimated with reasonable accuracy. The ratio of the maximum values of the two correlations will give an indication of the importance of the probe noise. The even function:

$$R_e(\tau) = \frac{\pi^{3/2}}{a}\left[1 - 2a^2\alpha^2 U_c^2(\tau - \tau_o)^2\right] e^{-a^2\alpha^2 U_c^2(\tau-\tau_o)^2} \tag{B10}$$

has a maximum $\tau = \tau_o = c_o^{-1}|x-y|$, while the odd function

$$R_o(\tau) = \frac{1}{2} S_{eff} \frac{1+\alpha^2}{\alpha^2} K a^2 c_o(\tau - \tau_o) e^{-a^2(1+\alpha^2)U_c^2(\tau-\tau_o)^2} \tag{B11}$$

has a maximum at $\tau = \tau_o + \sqrt{2}/(2a(1+\alpha)^{1/2}U_c)$. The ratio of the maximum

$$\psi = \frac{R_{e_{max}}}{R_{o_{max}}} = \frac{(2\pi)^{1/2}\alpha^2 M_c}{a^2 S_{eff} K\sqrt{1+\alpha^2}} \tag{B12}$$

should be large, if the probe noise is negligible. This criterion may be met if the effective surface area is small and the Mach number relatively high.

Let L be a typical correlation length; it follows that $a^2 = \pi/L^2$ and $S_{eff} = 4\pi R_p L$, where R_p is the radius of the probe support needle (the hot wire sensor is much smaller than the probe support). The correlation length scales with the axial position in the jet: $L = .13\, D\, (y_1/D)$, D is the diameter of the jet nozzle. The Reynolds number of a cylindrical probe support of radius

.01" in a Mach .3 air jet is approximately equal to 3500, and the drag coefficient is near unity (Schlichting, Ref. 81). The parameter K is set to be equal to the drag coefficient, and α is chosen to be .55 (Ref. 10). For a jet diameter of 3/4" and $U_c = 1/2\ U$, the ratio of the maxima is:

$$\psi = .16 \frac{y_1}{D} \tag{B13}$$

The model predicts that the probe noise makes a significant contribution to the correlation function, when the probe is placed in the principal sound producing region of a jet flow, namely the first 15 jet diameters downstream of the nozzle. Such a prediction is compatible with the marked differences of the shear noise correlations measured with the Laser Doppler Velocimeter and the ones measured with the hot wire anemometer.

APPENDIX C

CROSS-SPECTRAL DENSITY ESTIMATES

COMPUTED BY A FAST FOURIER TRANSFORM ANALYZER

The fast Fourier transform (FFT) analyzer exploits the close relationship between the Fourier series coefficients of a periodic wave $\hat{s}(t)$ and the Fourier transform of the non-periodic version of the same wave shape, namely that the Fourier series coefficients are uniformly spaced samples of the Fourier transform of the non-period wave (Harris, Ref. 85). For the purpose of machine computation only a finite number of points at which $s(t)$ is known can be used, and similarly there will be a finite number of frequencies at which the Fourier transform of the truncated sequence of $S(\omega)$ can be computed. The fast Fourier analyzer estimates the Fourier transform of an arbitrary function $f(t)$, subject to the constraints imposed above.

The effect of the finite duration, during which $f(t)$ is being analyzed, is equivalent to passing the signal $f(t)$ through a time window $D(t)$:

$$D(t) \begin{cases} 0, & t < -\frac{T}{2} \\ \text{Some suitable function} & \\ 0, & t > \frac{T}{2} \end{cases} \qquad \text{(C1)}$$

$D(t)$ is chosen to minimize the errors inherent in the process of power spectral density estimation. The most common errors are spectral broadening (finite analysis time) and the generation of side lobes (discontinuities at the beginning and end of the window). The behaviour of time window has been discussed in some detail by Harris (Ref. 86).

The Fourier transform of the function $D(t)f(t)$ is

$$\hat{\mathcal{F}}(\omega) = \frac{1}{2\pi}\int_{-\infty}^{\infty} D(t)f(t)e^{i\omega t}\,dt \qquad \text{(C2)}$$

Consider the product of the Fourier transform estimates of $f(t)$ and $g(t)$:

$$\hat{\mathcal{F}}(\omega)\hat{\mathcal{G}}^*(\omega) = \frac{1}{4\pi^2}\int D(t)f(t)e^{i\omega t}D^*(t')g^*(t')e^{-i\omega t'}\,dt\,dt' \qquad \text{(C3)}$$

The window function has a finite duration and possesses a Fourier transform $\mathcal{D}(\omega)$:

$$D(t) = \int \mathcal{D}(\omega) e^{-i\omega\tau}\, d\omega \qquad (C4)$$

and

$$\hat{\mathcal{F}}(\omega)\hat{\mathcal{G}}(\omega) = \frac{1}{4\pi^2}\int \mathcal{X}(\omega_o)\mathcal{X}^*(\omega_1) f(t) g^*(t+\tau) e^{-i(\omega_o-\omega_1)t}\, e^{i(\omega_1-\omega)\tau}\, dt\, d\omega_1\, d\omega_o\, dt' \qquad (C5)$$

Each realization of $\hat{\mathcal{F}}\,\hat{\mathcal{G}}^*$ can be treated as a member of an infinite set of realizations $\hat{\mathcal{F}}_i\,\hat{\mathcal{G}}_i^*$, if the process is ergodic. The ensemble average is defined to be:

$$\langle \hat{\mathcal{F}}_i \hat{\mathcal{G}}_i \rangle = \hat{\Phi}_{ff}(\omega) = \frac{1}{4\pi^2}\int \mathcal{X}(\omega_o)\mathcal{X}^*(\omega_1) \langle f_i(t) g_i^*(t+\tau)\rangle e^{-i(\omega_o-\omega_1)t}\, e^{i(\omega_1-\omega)\tau}\, dt\, d\omega_1\, d\omega_o\, dt' \qquad (C6)$$

But

$$\langle f_i(t) g_i^*(t+\tau)\rangle = R_{fg}(\tau) = \lim_{T\to\infty} \frac{1}{2T}\int_{-T}^{T} f(t) g^*(t+\tau)\, dt \qquad (C7)$$

(Blackman, Tukey, Ref. 87), and the correlation function is independent of t. The integration with respect to time t will result in the delta function $2\pi\,\delta(\omega_o - \omega_1)$; thus

$$\hat{\Phi}_{fg}(\omega) = \int |\mathcal{X}(\omega_1)|^2\, \Phi_{fg}(\omega_1 - \omega)\, d\omega_1 \qquad (C8)$$

where $\Phi_{fg}(\omega)$ is the cross-spectral density of f(t) and g(t). The convolution integral accounts for the absence of all $|\tau| > T$, brought about by the finite window duration.

$\hat{\mathcal{F}}_i\,\hat{\mathcal{G}}_i^*(\omega)$. The FFT analyzer computes the average value of N realizations of Each average may then be treated as an estimate of $\hat{\Phi}_{fg}(\omega)$.

APPENDIX D

SOME PROPERTIES OF THE LASER DOPPLER SIGNALS

A laser beam travelling in the x_1 direction can be modelled by the wave

$$E_1(\underset{\rightarrow}{x},t) = E_o(x_1)e^{-a^2(x_1)(x_2^2+x_3^2)}\, e^{i(2\pi\nu_o t - kx_1)} \tag{D1}$$

ν_o is the frequency of the laser light with a wave number k. E_o and a are slowly varying functions of x_1 and account for the slow beam divergence. When two beams derived from a common source intersect at $\underset{\rightarrow}{x} = 0$ with the angle 2ϕ, the total field near $\underset{\rightarrow}{x} = 0$ is

$$\underset{\rightarrow}{E_T}(\underset{\rightarrow}{x},t) = 2E_o\, e^{-a^2(x_1^2\sin^2\phi+x_2^2\cos^2\phi+x_3^2)}\, e^{i(2\pi\nu_o t-kx_1\cos\phi)}$$

$$\cdot\cosh(2a^2x_1x_2\cos\phi\sin\phi+ikx_2\sin\phi) \tag{D2}$$

The intensity of the light is proportional to $|E_T|^2$. The intensity distribution

$$|E_T|^2 = 2E_o^2\, e^{-2a^2(x_1^2\sin^2\phi+x_2^2\cos^2\phi+x_3^2)}$$

$$\times\{\cosh(4a^2x_1x_2\cos\phi\sin\phi) + \cos(2kx_2\sin\phi)\} \tag{D3}$$

is the sum of a smooth function known as the Doppler pedestal and an interference pattern $\cos(2kx_2\sin\phi)$. The distance between two maxima in the interference pattern is the fringe spacing

$$d_f = \frac{\lambda}{2\sin\phi} \tag{D4}$$

The Gaussian intensity profiles of the laser beams confine the fringe pattern near the point of intersection x = 0 usually referred to as the probe volume (Fig. D1). Surfaces of constant fringe intensity are defined by

$$x_1^2\sin^2\phi + x_2^2\cos^2\phi + x_3^2 = \text{constant} \tag{D5}$$

The probe volume is in the shape of an ellipsoid. The interference fringes are parallel to the x_1x_3 plane and are separated by a distance df. The angle of intersection 2ϕ is usually in the range of 3° to 40°, and the ellipse in the x_1x_3 plane has a large eccentricity, whereas the ellipse in the x_2x_3

plane is nearly circular. For $|\underset{\sim}{x}|$ sufficiently large, the Doppler pedestal masks the fringe pattern, and the Doppler signal that is scattered by particles can no longer be detected. Signal to noise considerations limit the LDV processor to accept only Doppler signals that exceed a certain threshold level and the probe volume is bounded by the surface (Fig. D2)

$$x_1^2 \sin^2\phi + x_2^2 \cos^2\phi + x_3^2 = R^2 \tag{D6}$$

The processor further requires that the scattering particle cross at least N_o fringes (N_o is usually 8). A particle that traverses the probe volume near the outer boundary may not intercept a sufficient number of fringes. The computation procedure, already initiated, cannot be completed. The percentage of valid Doppler bursts in the total number of signals that initiate computation is defined to be the % validation. The largest possible value of the % validation is the ratio of the projected areas of the effective probe volume containing at least 8 fringes, and the actual probe volume. The analysis applies only for laminar flow. The presence of turbulence will degrade the % validation.

There is a total of $N = 2R/d_f$ fringes in the probe volume, and therefore the effective probe volume has semi-major axis

$$a_1 = (N^2 - N_o^2)^{1/2} \frac{d_f}{2\sin\phi} \tag{D7}$$

and semi-minor axis

$$b_1 = (N^2 - N_o^2)^{1/2} \frac{d_f}{2} \tag{D8}$$

The area ratio is

$$\frac{\pi a_1 b_1}{\pi a_o b_o} = 1 - \frac{N_o^2}{N^2} \tag{D9}$$

$100\,(1 - N_o^2/N^2)$ is the largest possible % validation. To make the best use of the scattering particles, the % validation should be near the theoretical maximum. The % validation is an indirect measure of the data rate. The data rate f_c depends on the number of particles $\mathcal{N}$ that cross the probe volume per unit time:

$$f_c = \mathcal{N}\left(1 - \frac{N_o^2}{N^2}\right) \tag{D10}$$

If a velocity component other than the x_2 direction is to be measured, the probe volume must be rotated about the x_1 or x_3 axis. As the probe volume is rotated, the scattering cross-section of the probe volume changes. If the scattering cross-sections of the probe volume and the

effective probe volume change at the same rate, then the % validation will be unaffected. The data rate changes, as the number of particles that cross the effective probe volume is a function of the scattering cross-section.

Rotation about the x_1 or x_2 axis is analogous to the case of laminar flow making an angle θ with respect to the normal of the interference fringes. Rotation about the x_1 axis is considered first. The particles that intercept the probe volume (Fig. D3) move along lines defined by:

$$y = -(z - \hat{z})\tan\theta \tag{D11}$$

and intersect the ellipse $y^2\cos^2\phi + z^2 = R^2 - x^2\sin^2\phi = R^2(x)$ at:

$$z = \frac{\hat{z}\tan^2\theta\cos^2\phi \pm [R^2(x)(1 + \tan^2\theta\cos^2\phi) - \hat{z}^2\tan^2\theta\cos^2\phi]^{1/2}}{1 + \tan^2\theta\cos^2\phi}$$

$$z_o = \frac{R(x)(1 + \tan^2\theta\cos^2\phi)^{1/2}}{\tan\theta\cos\phi} \tag{D12}$$

$$z_2 - z_1 = \frac{2}{1 + \tan^2\theta\cos^2\phi}[R^2(x)\,1 + \tan^2\theta\cos^2\phi - \hat{z}^2\tan^2\theta\cos^2\phi]^{1/2}$$

By inspection:

$$\frac{1}{2}\ell_o = z_o\sin\theta = \frac{\cos\theta}{\cos\phi}R(x)(1 + \tan^2\theta\cos^2\phi)^{1/2} \tag{D13}$$

The scattering cross-section of the probe volume is an ellipse with semi-minor axis:

$$b_o = \frac{1}{2}\ell_o(0) = \frac{\cos\theta}{\cos\phi}R(1 + \tan^2\theta\cos^2\phi)^{1/2} \tag{D14}$$

Since the probe volume is rotated about the x_1 axis, the semi-major axis is invariant:

$$a_o = \frac{R}{\sin\phi} \tag{D15}$$

The scattering cross-section of the effective probe volume is bounded by the locus of all points such that:

$$z_2 = z_1 = N_o d_f \tag{D16}$$

and

$$\frac{1}{2}\,\ell(x) = \frac{\cos\theta}{\cos\phi}\left(R^2(x) - \frac{N_o^2 d_f^2}{4}\,(1 + \tan^2\theta\cos^2\phi)\right)^{1/2}(1 + \tan^2\theta\cos^2\phi)^{1/2}$$

The semi-minor axis is defined by 1/2 $\ell(0)$ and the semi-major axis has length $\hat{x}$, where $\ell(\hat{x}) = 0$:

$$a_1 = \frac{1}{\sin\phi}\left(R^2 - \frac{N_o^2 d_f^2}{4}\,(1 + \tan^2\theta\cos^2\phi)\right)^{1/2} \tag{D17}$$

$$b_1 = \frac{\cos\theta}{\cos\phi}\left(R^2 - \frac{N_o^2 d_f^2}{4}\,(1 + \tan^2\theta\cos^2\phi)\right)^{1/2}(1 + \tan^2\theta\cos^2\phi)^{1/2} \tag{D18}$$

The area ratio

$$\frac{\pi a_1 b_1}{\pi a_o b_o} = 1 - \frac{N_o^2}{N^2}\,(1 + \tan^2\theta\cos^2\phi)$$

As θ is increased, a critical angle θ_{crit} is reached at which the area ratio is zero. At this particular angle (dead angle) and beyond, no valid velocity measurements can be made with the LDV system:

$$\theta_{crit} = \arctan\left[\frac{1}{\cos\phi}\left(\frac{N^2}{N_o^2} - 1\right)^{1/2}\right] \tag{D19}$$

A similar analysis can be performed for the case of rotation about the x_3 axis (Fig. D4). The results are:

$$\text{area ratio} = 1 - \frac{N_o^2}{N^2}\,(1 + \tan^2\theta\sin^2\phi)$$

$$\theta_{crit} = \arctan\left[\frac{1}{\sin\phi}\left(\frac{N^2}{N_o^2} - 1\right)^{1/2}\right] \tag{D20}$$

In many systems the angle ϕ is of the order of a few degrees, and the latter configuration offers a better % validation, whereas the former possesses a superior data rate (Figs. D5, D6).

In the present investigation rotation about the x_3 axis was chosen, even though this particular configuration is not the best from the point of view of maximum achievable data rate. The system does, however, make use of nearly all particles that cross the probe volume and it is less susceptible to mean velocity changes across the probe volume.

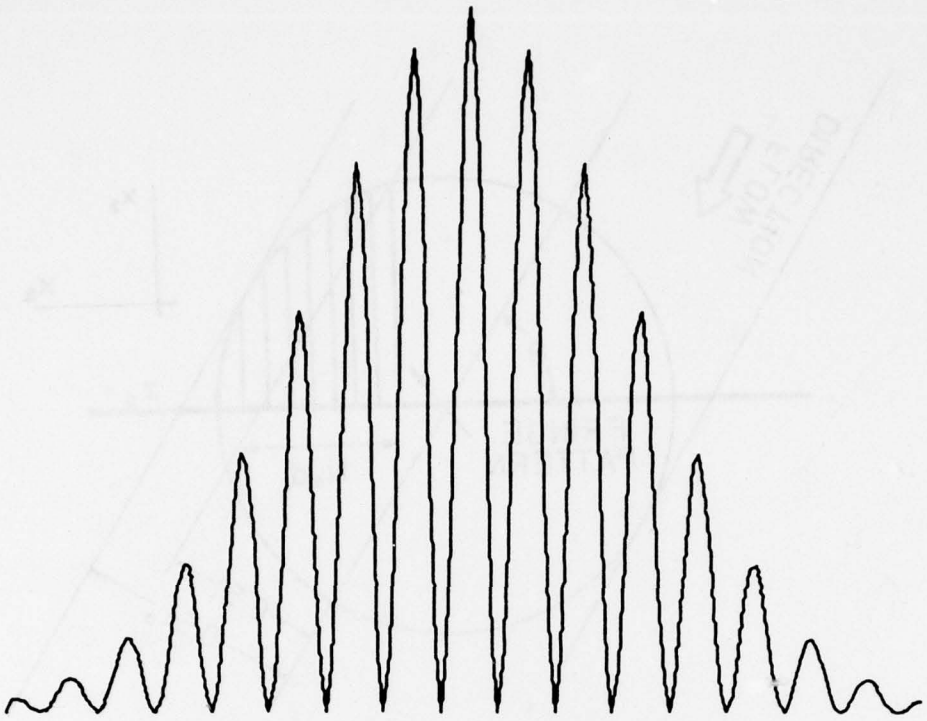


FIG. D.1 INTENSITY OF THE FRINGE PATTERN IN THE PROBE VOLUME ALONG THE LINE $x_3 = x_1 = 0$.

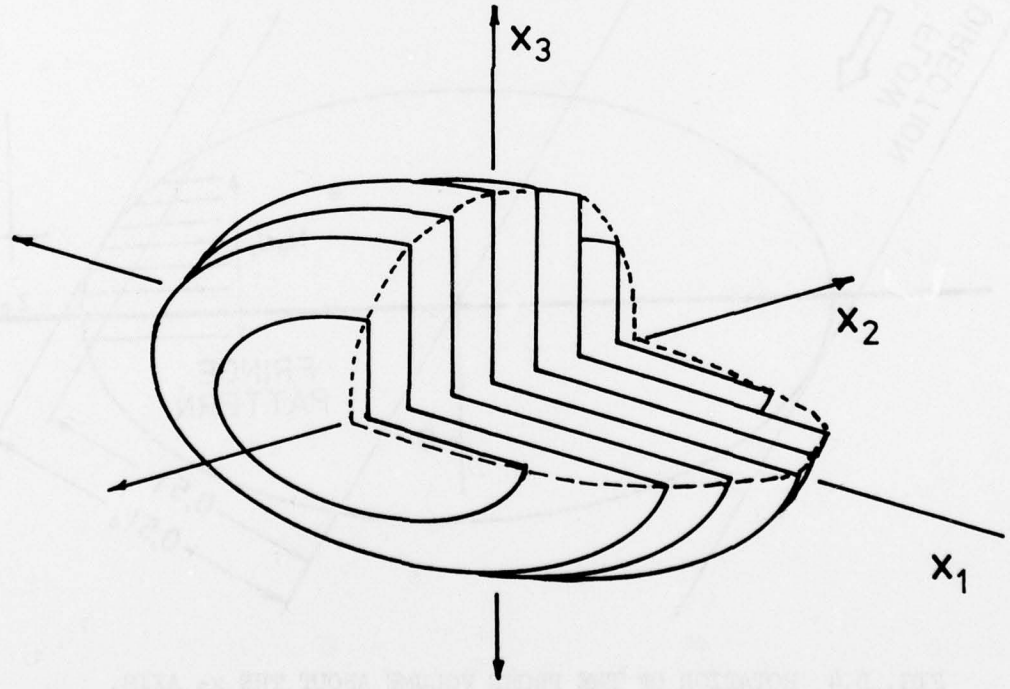


FIG. D.2 HYPOTHETICAL PROBE VOLUME.

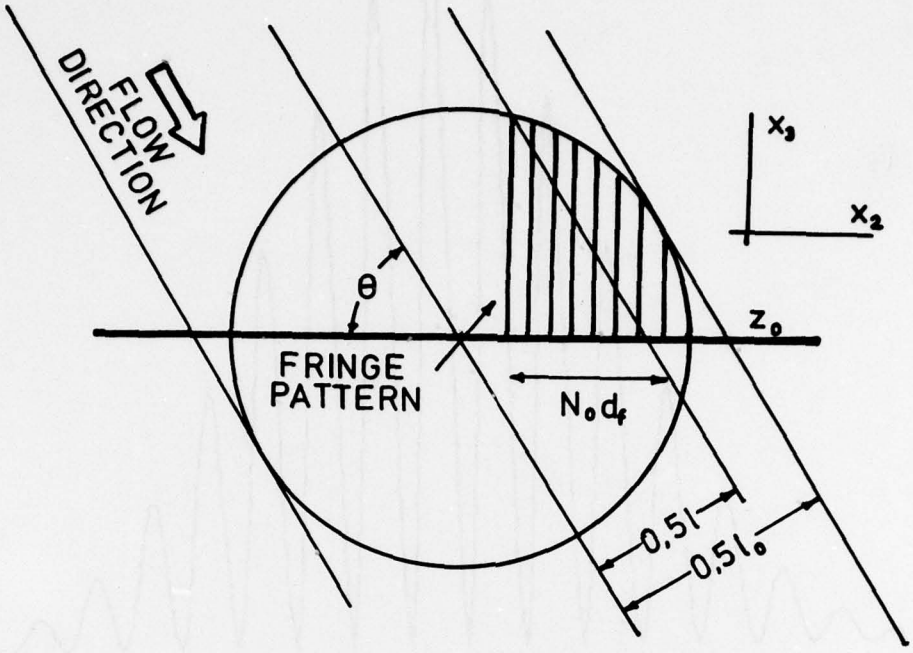


FIG. D.3 ROTATION OF THE PROBE VOLUME ATOUT THE x_1 AXIS.

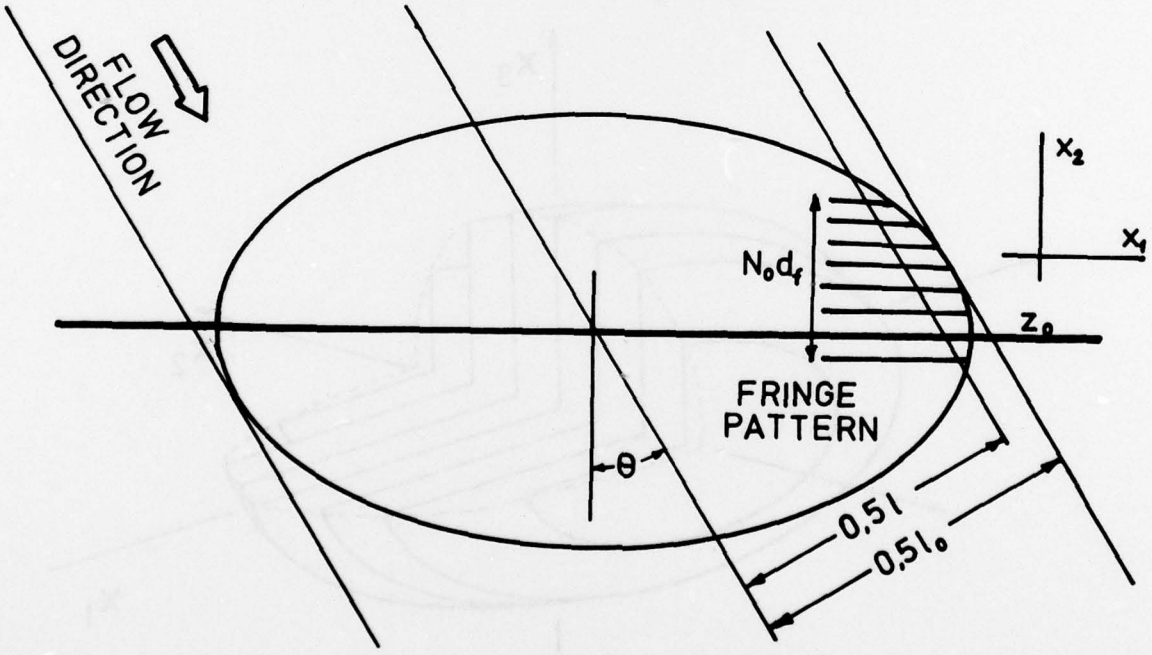


FIG. D.4 ROTATION OF THE PROBE VOLUME ABOUT THE x_3 AXIS.

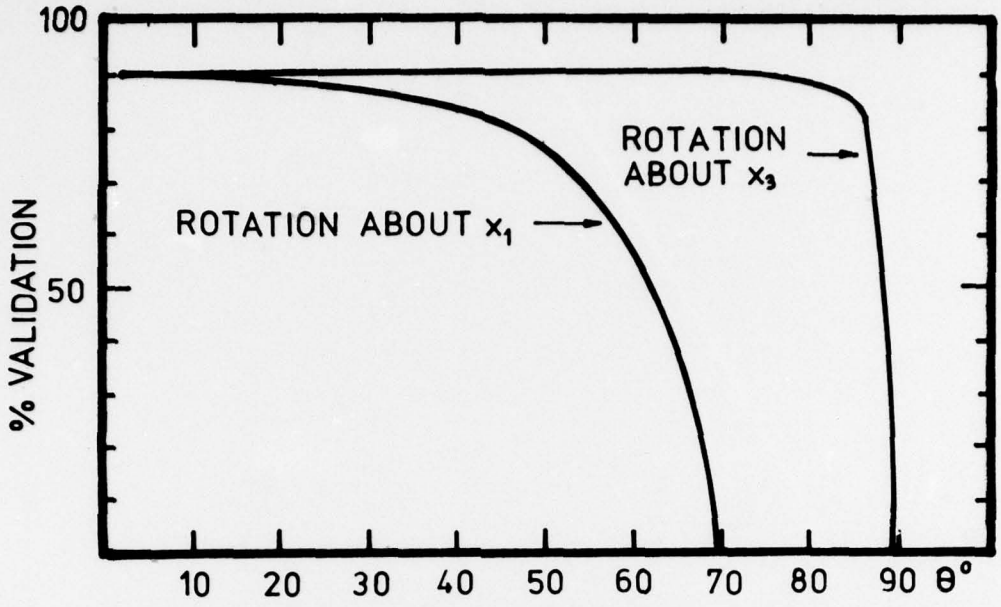


FIG. D.5 % VALIDATION AS A FUNCTION OF PROBE VOLUME ORIENTATION WITH RESPECT TO THE FLOW DIRECTION.

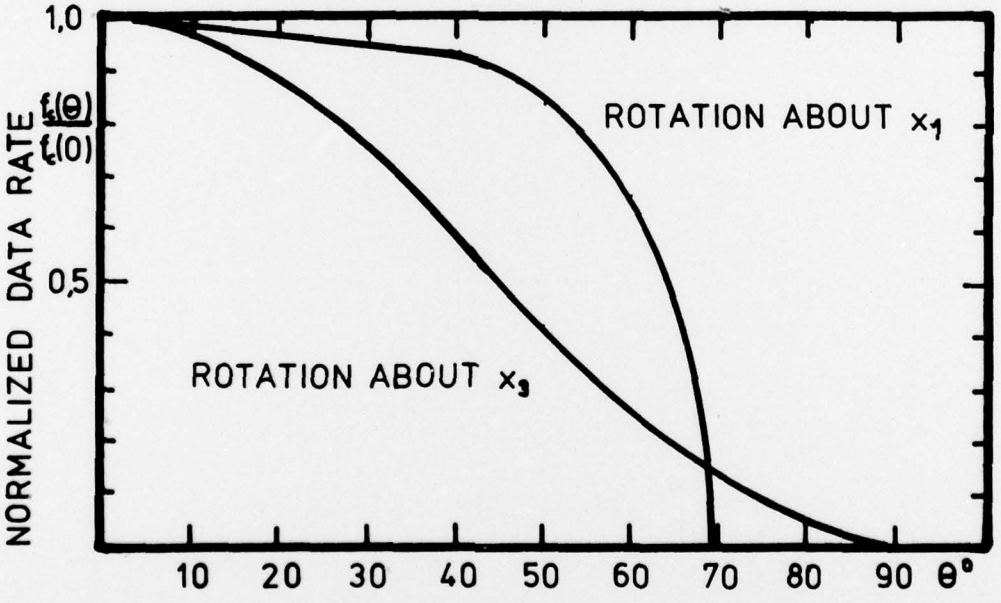


FIG. D.6 DATA RATE AS A FUNCTION OF PROBE ORIENTATION WITH RESPECT TO THE FLOW DIRECTION.

APPENDIX E

ESTIMATE OF THE POWER SPECTRAL DENSITY OF THE LDV OUTPUT

The laser Doppler velocimeter generates a sequence of output voltages $v(T_n)$ proportional to the speed of a particle in the probe volume at time $T_n - \delta$, δ is the computation time required by the processor (Fig. E1). The last realization of $v(T_n)$ is stored in the output memory of the processor until a new measurement has been performed. The time interval between successive measurements $v(T_{n+1})$ and $v(T_n)$ is ΔT_n, and the output waveform of the LDV has the form

$$\hat{v}(t) = \sum_{n=-N}^{N} v(T_n)[H(t - T_n) - H(t - T_{n+1})] \tag{E1}$$

The Fourier transform of $v(t)$ is

$$\hat{\mathcal{V}}(\omega) = \frac{1}{2\pi}\int \sum_{n=-N}^{N} v(T_n)[H(t - T_n) - H(t - T_{n+1})]e^{i\omega t}\, dt \tag{E2}$$

$$\hat{\mathcal{V}} = \sum_{n=-N}^{N} \frac{1}{2\pi} v(T_n)e^{i\omega T_n}\, \Delta T_n\, e^{i\omega \frac{\Delta T_n}{2}} \frac{\sin\left(\omega \frac{\Delta T_n}{2}\right)}{\omega \frac{\Delta T_n}{2}} \tag{E3}$$

For the special case of $\Delta T_n = \Delta T$, one may define a sampling frequency or data rate $f_c = \Delta T^{-1}$

$$\hat{\mathcal{V}}(\omega) = \frac{\sin \pi f/f_c}{\pi f/f_c}\, e^{i\pi f/f_c} \sum_{n=-N}^{N} \frac{1}{2\pi} v(n\Delta T)\, e^{i\omega n\Delta T}\, \Delta T \tag{E4}$$

$(\sin \pi f/f_c\, e^{i\pi f/f_c})/\pi f/f_c$ can be interpreted as the transfer function of the particular sampling process. The amplitude transfer function $(\sin \pi f/f_c)/\pi f/f_c$ has zeroes at $f = nf_c$, $n = 1, 2, \ldots$. The frequency window is a good low pass filter for frequencies less than $f = f_c/2$ (Fig. E2). The summation is an estimate of the Fourier transform of $v(t)$:

$$\mathcal{V}(\omega) = \frac{1}{2\pi}\int v(t)\, e^{i\omega t}\, dt \tag{E5}$$

$\hat{\mathcal{V}}(f)$ is a good estimate of $\mathcal{V}(f)$ if $f < f_c/2$ and if $\mathcal{V}(f)$ has little spectral content for frequencies greater than $f_c/2$. If this is not the case, then the estimated spectrum will contain spurious frequency components, called aliases.

As a simple example one may consider the case of oscillatory flow with frequency f_o. The output of the LDV processor will be:

$$\hat{W}(t) = v_o \sum_{n=-N}^{N} \cos\omega_o T_n [H(t - T_n) - H(t - T_{n+1})] \qquad \text{(E6)}$$

$$\hat{W}(f) = v_o \frac{\sin \pi f/f_c}{\pi f/f_c} e^{i\pi f/f_c} \sum_{n=-N}^{N} \frac{1}{2\pi} f_c \cos 2\pi f_o \frac{n}{f_c} e^{2\pi i \frac{nf}{f_c}} \qquad \text{(E7)}$$

$$= v_o \frac{\sin \pi f/f_c}{\pi f/f_c} e^{i\pi f/f_c} \left\{ -\frac{1}{2\pi f_c} + \sum_{n=0}^{N} \frac{1}{2\pi f_c} \cos 2\pi f_o \frac{n}{f_c} \left(e^{2\pi i \frac{nf}{f_c}} + e^{-2\pi i \frac{nf}{f_c}} \right) \right\} \qquad \text{(E8)}$$

The series can be written in the form:

$$\frac{1}{4\pi} \sum_{n=0}^{N} \left(e^{2\pi i \frac{f+f_o}{f_c}} \right)^n + \left(e^{-2\pi i \frac{f+f_o}{f_c}} \right)^n + \left(e^{2\pi i \frac{f-f_o}{f_c}} \right)^n + \left(e^{-2\pi i \frac{f-f_o}{f_c}} \right)^n \qquad \text{(E9)}$$

For $N \to \infty$ the series simplifies to (Gradshteyn and Ryzhik, Ref. 88):

$$\frac{1}{1 - e^{2\pi i \frac{f+f_o}{f_c}}} + \frac{1}{1 - e^{-2\pi i \frac{f+f_o}{f_c}}} + \frac{1}{1 - e^{2\pi i \frac{f-f_o}{f_c}}} + \frac{1}{1 - e^{-2\pi i \frac{f-f_o}{f_c}}} \qquad \text{(E10)}$$

$= 1/2\pi$ unless $f = \pm f_o$ or $f = mf_c \pm f_o$; m an integer.

At these special frequencies the series has an infinite value, and the usual interpretation of a delta function applies. The function W(f) has maxima at $f = \pm f_o$, the frequency of oscillation, and at $f = m f_c \pm f_o$. The latter are the aliases. There are no aliases in the range $0 < f < f_c/2$ for the case of $f_o < f_c/2$.

In order to avoid aliasing errors, the data rate of the LDV must be sufficiently high and satisfy the criteria outlined above. Turbulence spectra of Hot Wire Anemometer signals indicate that f_c should be 20 KHz or greater if aliasing errors are too negligible. Additional filtering of the signal v(t) generally does not reduce errors, as the aliases may be distributed over the entire span $0 < f < f_c$.

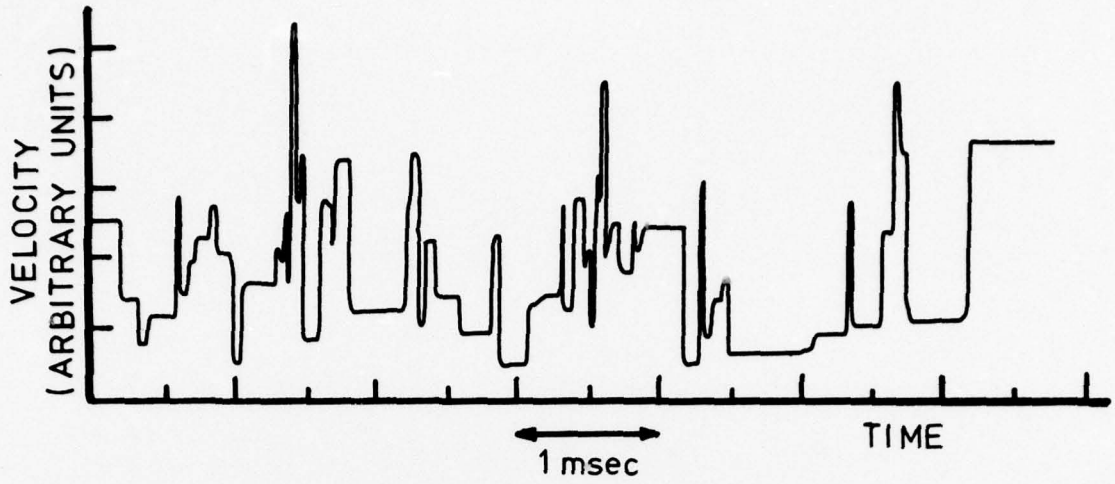


FIG. E.1 TYPICAL OUTPUT OF THE LDV PROCESSOR.

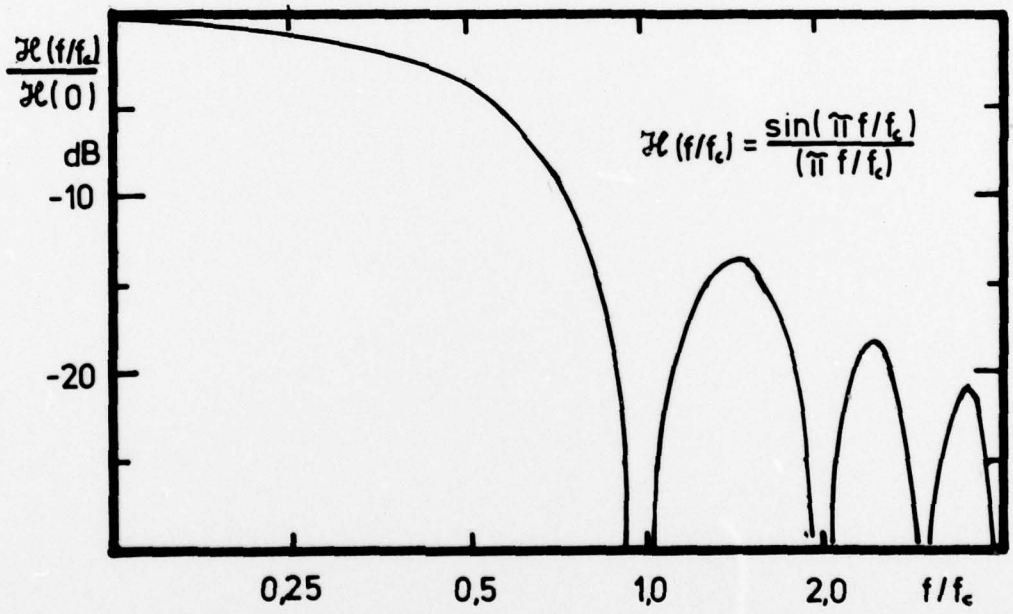


FIG. E.2 SPECTRAL WINDOW IMPOSED ON THE SPECTRUM ESTIMATE OF THE OUTPUT OF THE LDV PROCESSOR, AS A CONSEQUENCE OF THE DATA RATE f_c.

UTIAS REPORT NO. 230

Institute for Aerospace Studies, University of Toronto (UTIAS)
4925 Dufferin Street, Downsview, Ontario, Canada, M3H 5T6

DIRECT CORRELATION OF NOISE AND FLOW OF A JET USING LASER DOPPLER

Richarz, W. G. Approx. 130 pages 65 figures

1. Jet noise 2. Laser Doppler velocimeter 3. Correlations 4. Turbulence 5. Aerodynamic noise

I. Richarz, W. G. II. UTIAS Report No. 230

Lighthill's theory of jet noise, as extended and developed by Ribner (self and shear noise), has successfully described many features of the jet noise outside the 'refraction valley'. However, attempts to measure the self and shear noise source terms directly by means of a cross-correlation technique have been only partially successful. The major difficulty has been suspected as spurious 'probe noise' generated by turbulence - hot wire interaction. Thus, to avoid this problem, the traditional hot wire anemometer has been replaced in the present investigation by a non-intrusive device: a Laser Doppler Velocimeter. Substantial modifications were made to meet the constraints imposed by the correlation experiment; a major feature was provision to measure u_x, the component of turbulent velocity in the observer direction $\underline{x}$. Cross-correlations and cross-spectral densities of the jet noise at 40° to the jet axis and the instantaneous turbulent jet flow u_x ($\partial^2 u_x/\partial t^2$ ~ shear noise source term) or u_x^2 ($\partial^2 u_x^2/\partial t^2$ ~ self noise source term) were measured at various source positions in the jet. Source distributions were inferred therefrom over slices of jet normal to the jet axis. They were found to be strongly pear-shaped, rather than axisymmetric, the small end of the 'pear' pointing toward the observer. (This is not, however, incompatible with the axisymmetry of far field sound intensity.) Self and shear noise spectra have been constructed from the measured cross-spectral densities by a method consistent with the postulated self/shear noise formalism. The two spectra exhibit comparable amplitudes and virtually identical shapes, but are displaced substantially in frequency: all this is predicted by the theory. Self and shear noise spectra extracted from far field jet noise intensities via an algorithm of Nossier and Ribner exhibit the same behaviour. On the whole both sets of spectra, although derived from vastly different experimental procedures, are compatible.

Available copies of this report are limited. Return this card to UTIAS, if you require a copy.

UTIAS REPORT NO. 230

Institute for Aerospace Studies, University of Toronto (UTIAS)
4925 Dufferin Street, Downsview, Ontario, Canada, M3H 5T6

DIRECT CORRELATION OF NOISE AND FLOW OF A JET USING LASER DOPPLER

Richarz, W. G. Approx. 130 pages 65 figures

1. Jet noise 2. Laser Doppler velocimeter 3. Correlations 4. Turbulence 5. Aerodynamic noise

I. Richarz, W. G. II. UTIAS Report No. 230

Lighthill's theory of jet noise, as extended and developed by Ribner (self and shear noise), has successfully described many features of the jet noise outside the 'refraction valley'. However, attempts to measure the self and shear noise source terms directly by means of a cross-correlation technique have been only partially successful. The major difficulty has been suspected as spurious 'probe noise' generated by turbulence - hot wire interaction. Thus, to avoid this problem, the traditional hot wire anemometer has been replaced in the present investigation by a non-intrusive device: a Laser Doppler Velocimeter. Substantial modifications were made to meet the constraints imposed by the correlation experiment; a major feature was provision to measure u_x, the component of turbulent velocity in the observer direction $\underline{x}$. Cross-correlations and cross-spectral densities of the jet noise at 40° to the jet axis and the instantaneous turbulent jet flow u_x ($\partial^2 u_x/\partial t^2$ ~ shear noise source term) or u_x^2 ($\partial^2 u_x^2/\partial t^2$ ~ self noise source term) were measured at various source positions in the jet. Source distributions were inferred therefrom over slices of jet normal to the jet axis. They were found to be strongly pear-shaped, rather than axisymmetric, the small end of the 'pear' pointing toward the observer. (This is not, however, incompatible with the axisymmetry of far field sound intensity.) Self and shear noise spectra have been constructed from the measured cross-spectral densities by a method consistent with the postulated self/shear noise formalism. The two spectra exhibit comparable amplitudes and virtually identical shapes, but are displaced substantially in frequency: all this is predicted by the theory. Self and shear noise spectra extracted from far field jet noise intensities via an algorithm of Nossier and Ribner exhibit the same behaviour. On the whole both sets of spectra, although derived from vastly different experimental procedures, are compatible.

Available copies of this report are limited. Return this card to UTIAS, if you require a copy.

UTIAS REPORT NO. 230

Institute for Aerospace Studies, University of Toronto (UTIAS)
4925 Dufferin Street, Downsview, Ontario, Canada, M3H 5T6

DIRECT CORRELATION OF NOISE AND FLOW OF A JET USING LASER DOPPLER

Richarz, W. G. Approx. 130 pages 65 figures

1. Jet noise 2. Laser Doppler velocimeter 3. Correlations 4. Turbulence 5. Aerodynamic noise

I. Richarz, W. G. II. UTIAS Report No. 230

Lighthill's theory of jet noise, as extended and developed by Ribner (self and shear noise), has successfully described many features of the jet noise outside the 'refraction valley'. However, attempts to measure the self and shear noise source terms directly by means of a cross-correlation technique have been only partially successful. The major difficulty has been suspected as spurious 'probe noise' generated by turbulence - hot wire interaction. Thus, to avoid this problem, the traditional hot wire anemometer has been replaced in the present investigation by a non-intrusive device: a Laser Doppler Velocimeter. Substantial modifications were made to meet the constraints imposed by the correlation experiment; a major feature was provision to measure u_x, the component of turbulent velocity in the observer direction $\underline{x}$. Cross-correlations and cross-spectral densities of the jet noise at 40° to the jet axis and the instantaneous turbulent jet flow u_x ($\partial^2 u_x/\partial t^2$ ~ shear noise source term) or u_x^2 ($\partial^2 u_x^2/\partial t^2$ ~ self noise source term) were measured at various source positions in the jet. Source distributions were inferred therefrom over slices of jet normal to the jet axis. They were found to be strongly pear-shaped, rather than axisymmetric, the small end of the 'pear' pointing toward the observer. (This is not, however, incompatible with the axisymmetry of far field sound intensity.) Self and shear noise spectra have been constructed from the measured cross-spectral densities by a method consistent with the postulated self/shear noise formalism. The two spectra exhibit comparable amplitudes and virtually identical shapes, but are displaced substantially in frequency: all this is predicted by the theory. Self and shear noise spectra extracted from far field jet noise intensities via an algorithm of Nossier and Ribner exhibit the same behaviour. On the whole both sets of spectra, although derived from vastly different experimental procedures, are compatible.

Available copies of this report are limited. Return this card to UTIAS, if you require a copy.

UTIAS REPORT NO. 230

Institute for Aerospace Studies, University of Toronto (UTIAS)
4925 Dufferin Street, Downsview, Ontario, Canada, M3H 5T6

DIRECT CORRELATION OF NOISE AND FLOW OF A JET USING LASER DOPPLER

Richarz, W. G. Approx. 130 pages 65 figures

1. Jet noise 2. Laser Doppler velocimeter 3. Correlations 4. Turbulence 5. Aerodynamic noise

I. Richarz, W. G. II. UTIAS Report No. 230

Lighthill's theory of jet noise, as extended and developed by Ribner (self and shear noise), has successfully described many features of the jet noise outside the 'refraction valley'. However, attempts to measure the self and shear noise source terms directly by means of a cross-correlation technique have been only partially successful. The major difficulty has been suspected as spurious 'probe noise' generated by turbulence - hot wire interaction. Thus, to avoid this problem, the traditional hot wire anemometer has been replaced in the present investigation by a non-intrusive device: a Laser Doppler Velocimeter. Substantial modifications were made to meet the constraints imposed by the correlation experiment; a major feature was provision to measure u_x, the component of turbulent velocity in the observer direction $\underline{x}$. Cross-correlations and cross-spectral densities of the jet noise at 40° to the jet axis and the instantaneous turbulent jet flow u_x ($\partial^2 u_x/\partial t^2$ ~ shear noise source term) or u_x^2 ($\partial^2 u_x^2/\partial t^2$ ~ self noise source term) were measured at various source positions in the jet. Source distributions were inferred therefrom over slices of jet normal to the jet axis. They were found to be strongly pear-shaped, rather than axisymmetric, the small end of the 'pear' pointing toward the observer. (This is not, however, incompatible with the axisymmetry of far field sound intensity.) Self and shear noise spectra have been constructed from the measured cross-spectral densities by a method consistent with the postulated self/shear noise formalism. The two spectra exhibit comparable amplitudes and virtually identical shapes, but are displaced substantially in frequency: all this is predicted by the theory. Self and shear noise spectra extracted from far field jet noise intensities via an algorithm of Nossier and Ribner exhibit the same behaviour. On the whole both sets of spectra, although derived from vastly different experimental procedures, are compatible.

Available copies of this report are limited. Return this card to UTIAS, if you require a copy.

UNCLASSIFIED
SECURITY CLASSIFICATION OF THIS PAGE (When Data Entered)

REPORT DOCUMENTATION PAGE	READ INSTRUCTIONS BEFORE COMPLETING FORM
1. REPORT NUMBER: AFOSR-TR- 78-1641	2. GOVT ACCESSION NO. / 3. RECIPIENT'S CATALOG NUMBER
4. TITLE (and Subtitle): DIRECT CORRELATION OF NOISE AND FLOW OF A JET USING LASER DOPPLER	5. TYPE OF REPORT & PERIOD COVERED: INTERIM, 1 Jan 78 - 31 Dec 78
	6. PERFORMING ORG. REPORT NUMBER: UTIAS Report No 230
7. AUTHOR(s): W G RICHARZ	8. CONTRACT OR GRANT NUMBER(s): AFOSR 75-2808
9. PERFORMING ORGANIZATION NAME AND ADDRESS: UNIVERSITY OF TORONTO, INSTITUTE FOR AEROSPACE STUDIES, 4925 DUFFERIN ST, DOWNSVIEW, ONTARIO , CANADA, M3H 5T6	10. PROGRAM ELEMENT, PROJECT, TASK AREA & WORK UNIT NUMBERS: 2307A2, 61102F
11. CONTROLLING OFFICE NAME AND ADDRESS: AIR FORCE OFFICE SICNETIFIC RESEARCH/NA, BLDG 410, BOLLING AIR FORCE BASE, D C 20332	12. REPORT DATE: June 1978
	13. NUMBER OF PAGES: 112
14. MONITORING AGENCY NAME & ADDRESS(if different from Controlling Office)	15. SECURITY CLASS. (of this report): UNCLASSIFIED
	15a. DECLASSIFICATION/DOWNGRADING SCHEDULE

16. DISTRIBUTION STATEMENT (of this Report)

Approved for public release; distribution unlimited.

17. DISTRIBUTION STATEMENT (of the abstract entered in Block 20, if different from Report)

18. SUPPLEMENTARY NOTES

19. KEY WORDS (Continue on reverse side if necessary and identify by block number)

JET NOISE
LASER DOPPLER VELOCIMETER
CORRELATIONS
TURBULENCE
AERODYNAMIC NOISE

20. ABSTRACT (Continue on reverse side if necessary and identify by block number)

Lighthill's theory of jet noise, as extended and developed by Ribner (self and shear noise), has successfully described for features of the jet noise outside the 'refraction valley'. However, attempts to measure the self and shear noise source terms directly by means of a cross-correlation technique have been only partially successful. The major difficulty has been suspected as spurious 'probe noise' generated by turbulence - hot wire interaction. Thus, to avoid this problem, the traditional hot wire anemometer has been replaced in the present investigation by a non-intrusive device: a Laser Doppler Velocimeter. Substantial

DD FORM 1 JAN 73 1473

UNCLASSIFIED
SECURITY CLASSIFICATION OF THIS PAGE (When Data Entered)

modifications were made to meet the constraints imposed by the correlation experiment; a major feature was provision to measure u_x, the component of turbulent velocity in the observer direction x. Cross-correlations and cross-spectral densities of the jet noise at 40° to the jet axis and the instantaneous turbulent jet flow u_x ($\partial^2 u_x/\partial t^2 \sim$ shear noise source term) or u_x^2 ($\partial^2 u_x^2/\partial t^2 \sim$ self noise source term) were measured at various source positions in the jet. Source distributions were inferred therefrom over slices of jet normal to the jet axis. They were found to be strongly pear-shaped, rather than axisymmetric, the small end of the 'pear' pointing toward the observer. (This is not, however incompatible with the axisymmetry of far field sound intensity.) Self and shear noise spectra have been constructed from the measured cross-spectral densities by a method consistent with the postulated self/shear noise formalism. The two spectra exhibit comparable amplitudes and virtually identical shapes, but are displaced substantially in frequency: all this is predicted by the theory. Self and shear noise spectra extracted from far field jet noise intensities via an algorithm of Nossier and Ribner exhibit the same behavior. On the whole both sets of spectra, although derived from vastly different experimental procedures, are compatible.